Lappeenranta
University of Technology

Paula Immonen

ENERGY EFFICIENCY OF A DIESEL-ELECTRIC MOBILE WORKING MACHINE

Thesis for the degree of Doctor of Science (Technology) to be presented with due permission for public examination and criticism in the Auditorium 1382 at Lappeenranta University of Technology, Lappeenranta, Finland, on the 6th of June, 2013, at noon.

Acta Universitatis
Lappeenrantaensis 518

Supervisor

Professor Juha Pyrhönen
Department of Electrical Engineering
LUT Institute of Energy Technology (LUT Energy)
LUT School of Technology
Lappeenranta University of Technology
Finland

Reviewers and opponents

Professor Kalevi Huhtala
Intelligent Hydraulics and Automation
Tampere University of Technology
Finland

Assistant Professor Marko Hinkkanen
Department of Electrical Engineering
Aalto University
Finland

ISBN 978-952-265-414-4
ISBN 978-952-265-415-1 (PDF)
ISSN-L 1456-4491
ISSN 1456-4491

Lappeenrannan teknillinen yliopisto
Yliopistopaino 2013

Abstract

Lappeenranta University of Technology
Acta Universitatis Lappeenrantaensis 518

Paula Immonen

Energy Efficiency of a Diesel-Electric Mobile Working Machine

Lappeenranta 2013
133 p.

ISBN 978-952-265-414-4
ISBN 978-952-265-415-1 (PDF)
ISSN-L 1456-4491, ISSN 1456-4491

The power demand of many mobile working machines such as mine loaders, straddle carriers and harvesters varies significantly during operation, and typically, the average power demand of a working machine is considerably lower than the demand for maximum power. Consequently, for most of the time, the diesel engine of a working machine operates at a poor efficiency far from its optimum efficiency range. However, the energy efficiency of diesel-driven working machines can be improved by electric hybridization. This way, the diesel engine can be dimensioned to operate within its optimum efficiency range, and the electric drive with its energy storages responds to changes in machine loading. A hybrid working machine can be implemented in many ways either as a parallel hybrid, a series hybrid or a combination of these two. The energy efficiency of hybrid working machines can be further enhanced by energy recovery and reuse.

This doctoral thesis introduces the component models required in the simulation model of a working machine. Component efficiency maps are applied to the modelling; the efficiency maps for electrical machines are determined analytically in the whole torque–rotational speed plane based on the electrical machine parameters. Furthermore, the thesis provides simulation models for parallel, series and parallel-series hybrid working machines. With these simulation models, the energy consumption of the working machine can be analysed. In addition, the hybridization process is introduced and described.

The thesis provides a case example of the hybridization and dimensioning process of a working machine, starting from the work cycle of the machine. The selection and dimensioning of

the hybrid system have a significant impact on the energy consumption of a hybrid working machine. The thesis compares the energy consumption of a working machine implemented by three different hybrid systems (parallel, series and parallel-series) and with different component dimensions. The payback time of a hybrid working machine and the energy storage lifetime are also estimated in the study.

Keywords: diesel-electric hybridization, energy efficiency, mobile working machine
UDC 621.313:621.3.017:621.436:620.97:629

Acknowledgements

The research documented in this doctoral thesis was carried out at the Institute of Energy Technology (LUT Energy) at Lappeenranta University of Technology (LUT) during the years 2009–2012. The research was funded by the Graduate School of Electrical Energy Engineering (GSEEE) and the Finnish Funding Agency for Technology and Innovation (Tekes).

I express my gratitude to Professor Juha Pyrhönen, the supervisor of this thesis and Professor Pertti Silventoinen for their comments and corrections to the work, and Dr. Lasse Laurila for the collaboration and encouragement over the years.

The comments by the preliminary examiners, Professor Kalevi Huhtala and Assistant Professor Marko Hinkkanen, are highly appreciated.

Dr. Hanna Niemelä deserves my special thanks for her work to edit the language of this work.

I express my thanks to all project members who have contributed to this work; Ville Ahola, M.Sc. and Janne Uusi-Heikkilä, M.Sc. from the Department of Intelligent Hydraulics and Automation at Tampere University of Technology (TUT IHA) for their collaboration on the research of hydraulic systems and for providing the power curves of the working hydraulics. I also express my thanks to my colleagues. Especially, Dr. Vesa Ruuskanen for the collaboration on developing the algorithms to calculate the efficiency maps of the electric machines and Dr. Lassi Aarniovuori, for providing the measurement results to verify the method to calculate the efficiency map of the induction machine.

Financial support by Walter Ahlström Foundation, The Finnish Foundation for Technology Promotion, The Finnish Cultural Foundation, The South Karelia Regional Fund, Ulla Tuominen Foundation and Emil Aaltonen Foundation is highly appreciated.

Finally, I express my gratitude to my family for their the support and understanding during the years.

Lappeenranta, May 7th, 2013

Paula Immonen

Contents

List of Symbols and Abbreviations

Roman letters

A	surface $\left[\mathrm{m}^2\right]$
A_f	front cross-sectional area $\left[\mathrm{m}^2\right]$
a	acceleration $\left[\mathrm{m/s}^2\right]$
B	friction coefficient of rotation $[\mathrm{Js}]$, magnetic flux density $\left[\mathrm{Vs/m}^2\right]$
C	capacitance $[\mathrm{As/V}]$, specific heat capacity $[\mathrm{J/kgK}]$
C_d	air drag coefficient [-]
C_sc	capacitance of the supercapacitor $[\mathrm{As/V}]$
D	diameter $[\mathrm{m}]$
DOD	depth of discharge [%]
D_s	stator inner diameter $[\mathrm{m}]$
D_se	stator outer diameter $[\mathrm{m}]$
$\vec{e}_\mathrm{m}, e_\mathrm{m}$	magnetizing electromotive force (vector, absolute value) $[\mathrm{V}]$
$\vec{e}_\mathrm{PM}, e_\mathrm{PM}$	no-load voltage (vector, absolute value) $[\mathrm{V}]$
$\vec{e}_\mathrm{s}, e_\mathrm{s}$	stator electromotive force (vector, absolute value) $[\mathrm{V}]$
E	energy $[\mathrm{J}]$
E_es	energy storage capacity [kWh]
E_off	IGBT turn-off energy $[\mathrm{J}]$
E_on	IGBT turn-on energy $[\mathrm{J}]$
E_rr	diode turn-off energy $[\mathrm{J}]$
E_sc	supercapacitor energy $[\mathrm{J}]$

F_{air}	air drag $[\mathrm{N}]$
F_{brake}	brake force $[\mathrm{N}]$
F_{eq}	equivalent force $[\mathrm{N}]$
F_{res}	friction force $[\mathrm{N}]$
F_{roll}	rolling force $[\mathrm{N}]$
F_{slope}	force caused by the inclination of the road $[\mathrm{N}]$
F_{wheel}	force caused by the wheel moment of inertia $[\mathrm{N}]$
f	frequency $[\mathrm{Hz}]$
f_{n}	nominal frequency $[\mathrm{Hz}]$
f_{sw}	switching frequency $[\mathrm{Hz}]$
G	gear [-]
g	gravitation constant $\left[\mathrm{m/s^2}\right]$
H	magnetic field strength $[\mathrm{A/m}]$, difference in prices [€]
I	current $[\mathrm{A}]$
I_{n}	nominal current $[\mathrm{A}]$
i_{dc}	DC current $[\mathrm{A}]$
i_{em}	electrical machine current $[\mathrm{A}]$
i_{es}	energy storage current $[\mathrm{A}]$
i_{diff}	final drive fixed gear ratio [-]
i_{Fe}	iron loss current $[\mathrm{A}]$
i_{Fed}	direct-axis iron loss current $[\mathrm{A}]$
i_{Feq}	quadrature-axis iron loss current $[\mathrm{A}]$
$\vec{i}_{\mathrm{m}}, i_{\mathrm{m}}$	magnetizing current (vector, absolute value) $[\mathrm{A}]$
$\vec{i}_{\mathrm{md}}, i_{\mathrm{md}}$	direct-axis magnetizing current (vector, absolute value) $[\mathrm{A}]$
$\vec{i}_{\mathrm{mq}}, i_{\mathrm{mq}}$	quadrature-axis magnetizing current (vector, absolute value) $[\mathrm{A}]$
$\vec{i}_{\mathrm{r}}, i_{\mathrm{r}}$	rotor current (vector, absolute value) $[\mathrm{A}]$
i_{rd}	direct-axis rotor current $[\mathrm{A}]$
i_{rq}	quadrature-axis rotor current $[\mathrm{A}]$
$\vec{i}_{\mathrm{s}}, i_{\mathrm{s}}$	stator current (vector, absolute value) $[\mathrm{A}]$
i_{sc}	supercapacitor current $[\mathrm{A}]$
$\vec{i}_{\mathrm{sd}}, i_{\mathrm{sd}}$	direct-axis stator current (vector, absolute value) $[\mathrm{A}]$

$\vec{i}_{\mathrm{sq}}, i_{\mathrm{sq}}$	quadrature-axis stator current (vector, absolute value) $[\mathrm{A}]$
i_{trans}	gear ratio [-]
J	moment of inertia $\left[\mathrm{kgm}^2\right]$
j	imaginary unit
$\vec{\mathrm{j}}$	imaginary unit vector
K	capacity factor $\left[1/\mathrm{s}\sqrt{\mathrm{Nm}}\right]$
k	rolling friction coefficient [-], interest rate [-]
k_{f}	friction loss coefficient $[\mathrm{W}]$
k_{w}	windage loss coefficient $\left[\mathrm{Ws}^2\right]$
L	inductance $[\mathrm{Vs/A}]$
L_{m}	magnetizing inductance $[\mathrm{Vs/A}]$
L_{md}	direct-axis magnetizing inductance $[\mathrm{Vs/A}]$
L_{mq}	quadrature-axis magnetizing inductance $[\mathrm{Vs/A}]$
L_{r}	rotor inductance $[\mathrm{Vs/A}]$
$L_{\mathrm{r}\sigma}$	rotor leakage inductance $[\mathrm{Vs/A}]$
L_{s}	stator inductance $[\mathrm{Vs/A}]$
L_{sc}	series inductance of the supercapacitor $[\mathrm{Vs/A}]$
L_{sd}	stator direct-axis inductance $[\mathrm{Vs/A}]$
L_{sq}	stator quadrature-axis inductance $[\mathrm{Vs/A}]$
$L_{\mathrm{s}\sigma}$	stator leakage inductance $[\mathrm{Vs/A}]$
l	length $[\mathrm{m}]$
l_{c}	core length $[\mathrm{m}]$
M	modulation index [-]
m	mass $[\mathrm{kg}]$
m_{veh}	mass of the vehicle $[\mathrm{kg}]$
m_{wheel}	mass of the wheel $[\mathrm{kg}]$
N	hold time [a]
N_{s}	number of series-connected cells [-]
N_{p}	number of parallel-connected cells [-]
NPV	net present value [€]
n	rotational speed [rpm]

n_{d}	diesel engine rotational speed [rpm]
n_{n}	nominal rotational speed [rpm]
P	power [W]
P_{add}	additional losses [W]
P_{cond}	conduction losses [W]
$P_{\mathrm{cond,D}}$	diode conduction losses [W]
$P_{\mathrm{cond,IGBT}}$	IGBT conduction losses [W]
$P_{\mathrm{Cu,r}}$	rotor copper losses [W]
$P_{\mathrm{Cu,s}}$	stator copper losses [W]
P_{d}	power of the diesel engine [W]
P_{es}	power capacity of the energy storage [W]
P_{Fe}	iron losses [W]
$P_{\mathrm{inv,loss}}$	inverter losses [W]
P_{load}	load power [W]
P_{mec}	mechanical losses [W]
P_{n}	nominal power [W]
P_{SOC}	SoC-dependent power reference [W]
P_{sw}	switching losses [W]
$P_{\mathrm{sw,D}}$	diode switching losses [W]
$P_{\mathrm{sw,IGBT}}$	IGBT switching losses [W]
p	number of pole pairs [-]
PB	payback time [a]
Q	charge [As]
R	resistance [V/A]
R_{charge}	battery resistance [V/A]
R_{CE}	on-state resistance of the IGBT [V/A]
R_{D}	on-state resistance of the diode [V/A]
$R_{\mathrm{discharge}}$	battery resistance [V/A]
$R_{\mathrm{ESR,sc}}$	equivalent series resistor of the supercapacitor [V/A]
R_{Fe}	iron loss resistance [V/A]
R_{p}	parallel resistor of the supercapacitor [V/A]

R_r	rotor resistance $[\mathrm{V/A}]$
R_s	stator resistance $[\mathrm{V/A}]$
R_T	torque ratio [-]
r_wheel	radius of the tyre $[\mathrm{m}]$
$r_\mathrm{wheel,eff}$	effective radius of the tyre $[\mathrm{m}]$
SA	annual saving [€]
SOC	state of charge [-]
s	slip [-], distance $[\mathrm{m}]$
T_amb	ambient temperature $[^\circ\mathrm{C}]$
T_core	temperature of the battery surface $[^\circ\mathrm{C}]$
T_d	torque of the diesel engine $[\mathrm{Nm}]$
T_diff	output torque of the final drive $[\mathrm{Nm}]$
T_em	electric torque $[\mathrm{Nm}]$
T_load	load torque $[\mathrm{Nm}]$
T_n	nominal torque $[\mathrm{Nm}]$
T_SOC	SoC-dependent torque reference $[\mathrm{Nm}]$
T_tc	torque of the torque converter $[\mathrm{Nm}]$
T_trans	output torque of the gearbox $[\mathrm{Nm}]$
t	time $[\mathrm{s}]$
U_CE0	threshold voltage of the IGBT $[\mathrm{V}]$
U_D	threshold voltage of the diode $[\mathrm{V}]$
U_n	nominal voltage $[\mathrm{V}]$
u_dc	DC voltage $[\mathrm{V}]$
u_es	energy storage voltage $[\mathrm{V}]$
u_inv	inverter voltage $[\mathrm{V}]$
u_md	direct-axis magnetizing voltage $[\mathrm{V}]$
u_mq	quadrature-axis magnetizing voltage $[\mathrm{V}]$
u_OC	open-circuit voltage $[\mathrm{V}]$
$\vec{u}_\mathrm{r}, u_\mathrm{r}$	rotor voltage (vector, absolute value) $[\mathrm{V}]$
u_rd	direct-axis rotor voltage $[\mathrm{V}]$
u_rq	quadrature-axis rotor voltage $[\mathrm{V}]$

$\vec{u}_\mathrm{s}, u_\mathrm{s}$	stator voltage (vector, absolute value) $[\mathrm{V}]$
u_sc	terminal voltage of the supercapacitor $[\mathrm{V}]$
u_sd	direct-axis stator voltage $[\mathrm{V}]$
u_sq	quadrature-axis stator voltage $[\mathrm{V}]$
v_veh	vehicle speed $[\mathrm{m/s}]$

Greek Letters

α	angular acceleration $\left[\mathrm{rad/s^2}\right]$, convection coefficient $\left[\mathrm{W/Km^2}\right]$
β	surface inclination angle [rad]
γ	angle of the magnetizing current $[\mathrm{rad}]$
δ	load angle $[\mathrm{rad}]$
η_ed	electric drive efficiency [-]
η_em	electrical machine efficiency [-]
η_d	diesel engine efficiency [-]
η_diff	final drive efficiency [-]
η_inv	inverter efficiency [-]
η_tc	torque converter efficiency [-]
η_trans	gearbox efficiency [-]
μ_r	relative permeability [-]
ρ	air density $\left[\mathrm{kg/m^3}\right]$
$\vec{\psi}_\mathrm{m}, \psi_\mathrm{m}$	magnetizing flux linkage, air-gap flux linkage, (vector, absolute value), $[\mathrm{Vs}]$
ψ_md	direct-axis magnetizing flux linkage $[\mathrm{Vs}]$
ψ_mq	quadrature-axis magnetizing flux linkage $[\mathrm{Vs}]$
$\vec{\psi}_\mathrm{PM}, \psi_\mathrm{PM}$	permanent magnet flux linkage (vector, absolute value) $[\mathrm{Vs}]$
$\vec{\psi}_\mathrm{r}, \psi_\mathrm{r}$	rotor flux linkage, (vector, absolute value) $[\mathrm{Vs}]$
ψ_rd	direct-axis rotor flux linkage $[\mathrm{Vs}]$
ψ_rq	quadrature-axis rotor flux linkage $[\mathrm{Vs}]$
$\vec{\psi}_\mathrm{s}, \psi_\mathrm{s}$	stator flux linkage, (vector, absolute value) $[\mathrm{Vs}]$
ψ_sd	direct-axis stator flux linkage $[\mathrm{Vs}]$

ψ_{sq}	quadrature-axis stator flux linkage $[\mathrm{Vs}]$
$\vec{\psi}_{\delta}, \psi_{\delta}$	air-gap flux linkage, (vector, absolute value) $[\mathrm{Vs}]$
τ_{em}	electrical machine time constant $[\mathrm{s}]$
τ_{d}	diesel engine time constant $[\mathrm{s}]$
ϕ	phase angle $[\mathrm{rad}]$
Ω	mechanical angular velocity $[\mathrm{rad/s}]$
Ω_{d}	mechanical angular velocity of the diesel engine $[\mathrm{rad/s}]$
Ω_{diff}	mechanical angular velocity of the final drive $[\mathrm{rad/s}]$
Ω_{em}	mechanical angular velocity of the electrical machine $[\mathrm{rad/s}]$
Ω_{rel}	relative angular velocity $[\mathrm{rad/s}]$
Ω_{tc}	mechanical angular velocity of the torque converter $[\mathrm{rad/s}]$
Ω_{trans}	mechanical angular velocity of the transmission $[\mathrm{rad/s}]$
ω	angular frequency $[\mathrm{rad/s}]$
ω_{s}	stator angular frequency $[\mathrm{rad/s}]$
ω_{r}	rotor angular frequency $[\mathrm{rad/s}]$

Acronyms

CO	carbon monoxide
CO_2	carbon dioxide
DC	direct current
DoD	depth of discharge
DPF	diesel particulate filter
EGR	exhaust gas recirculation
EMR	energetic macroscopic representation
EPA	Environment Protection Agency
EU	European Union
HC	hydrocarbon
IGBT	insulated gate bipolar transistor
IM	induction machine

LiTi	lithium titanate
LPF	low-pass filter
LS	load sensing
NEDC	New European Driving Cycle
NiMH	nickel-metal hydride
NO_x	nitrogen oxide
NPV	net present value
PM	particulate matter
PMSM	permanent magnet synchronous machine
RMS	root mean square
RTG	rubber-tyred gantry
SCR	selective catalytic reduction
SoC	state of charge

Chapter 1

Introduction

Mobile working machines such as mine loaders, straddle carriers, load tractors, cranes, harvesters and log or container staggers are widely used all around the world. Consequently, the energy consumed and emissions caused by mobile working machines are significant. For these reasons, tightening emissions regulations and standards, increasing oil prices and thereby increasing variable costs have aroused increasing interest in electric hybridization of mobile working machines. The target of hybridization by applying electrical engineering solutions in mobile machines is to achieve a significant, at least 20% and, in some cases, even up to 50% reduction in the energy consumption and emissions. In the context of mobile applications, several terms are used to refer to mobile working machines, such as off-road machines, non-road machines or off-road machinery. In this work, however, the term 'mobile working machine' will be mainly used.

1.1 Motivation of hybridization

There are two main motivations to hybridize a mobile working machine. The first one is the need to decrease the fuel consumption, while the second one arises from the tightening emissions regulations and standards that demand improvements in the machines in order to reduce the environmental stress. To this end, the load cycles (work cycles) of a mobile working machine are often such that hybridization provides significant fuel consumption savings. In the optimal hybrid machine case, with energy recovery, a significantly smaller diesel engine can be selected, and therefore, the engine can operate in its best efficiency range.

However, the emissions regulations sometimes lead to an engine design that provides a reduced energy efficiency and dynamic performance of an engine. Nevertheless, with a hybrid system, it is possible to reduce the energy consumption even though the diesel performance is degraded.

1.2 Emissions regulations

The increasing concern about the adverse effects resulting from the use of fossil fuels and the possible climate warming have resulted in more stringent emissions regulations and standards for diesel engines. The regulations concerning working machine diesels are tightened up after the redefinition of the standards for the car engine emissions. Consequently, the new regulations have an impact on most of the working machines because they are normally diesel powered.

The US Environmental Protection Agency (EPA) and the European Union (EU) have emission standards of their own with similar regulations but different effective dates. Thus far, the emissions of carbon dioxide (CO_2) are not regulated, but the norms concern the emissions of carbon monoxide (CO), particles (PM), nitrogen oxides (NO_x) and hydrocarbons (HC). Table 1.1 describes the EPA Tier 4 Interim and Tier 4 Final emission levels and effective dates, while Table 1.2 gives the corresponding values for the EU Stage IIIB and Stage IV for diesels of different sizes [1].

Table 1.1: EPA non-road diesel engine emission standard; CO / PM / (NO_x + HC) or CO / PM / NO_x / HC [g/kWh] [1].

Engine Power [kW]	2008	2009	2010	2011	2012	2013	2014	2015	2016
$8 \leq P_d < 19$	6.6/0.4/7.5								
$19 \leq P_d < 37$	5.5/0.3/7.5					5.5/0.03/4.7			
$37 \leq P_d < 56$	5.0/0.3/4.7					5.0/0.03/4.7			
$56 \leq P_d < 130$					5.0/0.02/0.19/3.4			5.0/0.02/0.19/0.40	
$130 \leq P_d < 560$				3.5/0.02/0.19/2			3.5/0.02/0.19/0.40		

EPA Tier 4 Interim and EPA Tier 4 Final

Table 1.2: EU non-road diesel engine emission standard; CO / PM / (NO_x + HC) or CO / PM / NO_x / HC [g/kWh] [1].

Engine Power [kW]	2008	2009	2010	2011	2012	2013	2014	2015	2016
$19 \leq P_d < 37$	5.5/0.6/7.5								
$37 \leq P_d < 56$						5.0/0.025/4.7			
$56 \leq P_d < 130$					5.0/0.025/0.19/3.3		5.0/0.025/0.19/0.4		
$130 \leq P_d < 560$				3.5/0.025/0.19/2.0			3.5/0.025/0.19/0.4		

EU Stage IIIA, EU Stage IIIB and EU Stage IV

Because of the new emissions regulations and standards, the PM, NO_x and HC emissions must be significantly reduced from the present level. Figure 1.1 presents the combined NO_x and HC emissions in grams per kWh according to different Tier classification levels. The combined NO_x and HC emissions have to be decreased in diesel engines having power more than 225 kW, while the emission standards are tightened by more than 90% from the Tier 2 level. CO emissions, however, will not change essentially compared with the present values. In present-day mobile machines, engines with more than 130 kW power are normally used. The new emission standards (EPA Tier 4 Final and EU Stage IV) for them will become effective at the beginning of 2014.

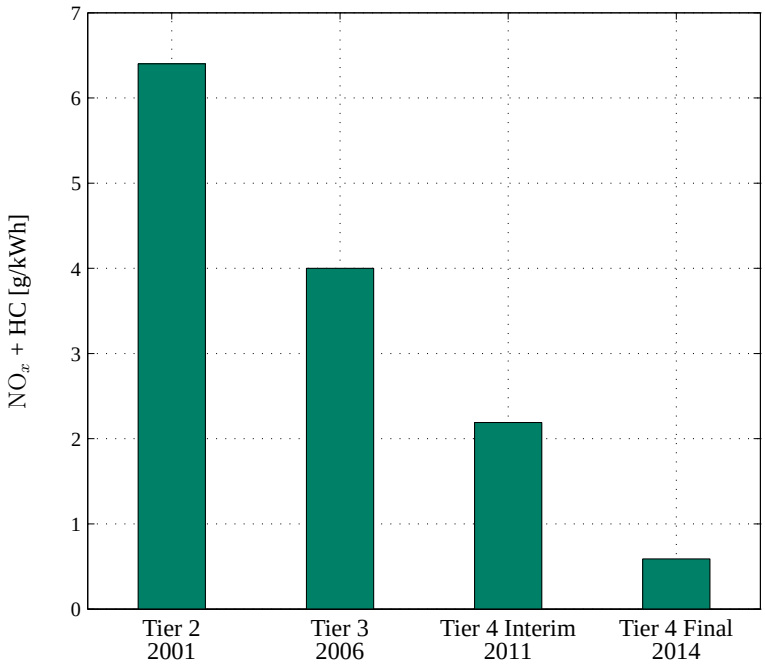

Fig. 1.1: Combined maximum allowable emission levels for 225 kW diesel engines according to different Tier levels [1].

The tightening regulations on CO, HC, NO_x and particle emissions of diesel engines in working machines have brought new challenges for the engine manufacturers. One of the major challenges in developing the engines further is to simultaneously limit both the NO_x and PM emissions still keeping the fuel consumption as low as possible [2].

The control of a diesel engine significantly affects the emissions and the fuel consumption. The timing of the fuel injection has a significant impact on the diesel emissions and efficiency. Early injection increases the combustion temperature, which reduces the fuel consumption and PM emissions but increases the generation of NO_x emissions. Considering the NO_x emissions, it is preferable to inject the fuel later, but then, the efficiency of the engine will suffer [3]. The dependency of NO_x and PM emissions can be reduced only by post-processing of the exhaust fumes.

Working machine engine manufacturers have developed post-processing systems for exhaust fumes. For instance, Exhaust Gas Recirculation (EGR), Diesel Particulate Filter (DPF) and Selective Catalytic Reduction (SCR) are used [4].

The EGR and SCR systems reduce diesel NO_x emissions [5]. In the EGR system, part of the exhaust fumes are recirculated through an EGR valve to an EGR cooler, from which the fumes are mixed to the inlet air. The cool intake air mixed with the exhaust fumes reduces the oxygen content of the intake air, which decreases the combustion temperature and results in a lower NO_x level. However, application of the EGR system increases fuel consumption, as the lower oxygen content in the combustion chamber degrades the efficiency [6], [7].

With the SCR system, the NO_x emissions are cut down by using a reduction substance. In the system, urea is used as the substance that is sprayed into the exhaust fumes. After spraying, the fumes travel to an SCR catalyzer, and the harmful nitrogen oxides are converted into nitrogen and water [8]. In the SCR system, NO_x emissions are reduced outside the engine combustion process, and thus, the combustion process and the fuel injection can be optimized, which again cuts down fuel consumption [9].

The function of the DPF is to collect particles and burn them in a high temperature to ashes. After the catalyzer, the soot particles travel to the DPF filter and are collected on its walls. When enough particles have been collected, the particles will be burnt [10]. The PM emissions can also be reduced by using different biofuels [11].

Unfortunately, reducing the amount of emissions by post-processing systems may increase the fuel consumption and limits the opportunities to improve the energy efficiency of diesel drives [7]. The emissions control system may also reduce the response of a diesel engine [12]. The manufacturers aim at achieving the emission standard levels; however, it is impossible to remove all emissions, and therefore, it is important to analyse the whole system powered by the diesel. The power chain of a working machine has to be studied as an entity.

By improving the energy efficiencies of individual components, it is possible to reduce the power loss of a working machine and to save fuel. At the same time, pollution is reduced when a certain task needs less fuel. Completely new system options must also be considered, especially, if the working machine cycle provides opportunities for recovering potential energy for further use. Mobile machine manufacturers are becoming increasingly interested in hybridization of their machines. Hybridization can result in reduced emissions because it is possible to run a diesel engine in its optimum range while the fuel consumption and emissions are reduced and the post-processing of exhaust fumes is easier.

Despite hybridization and significantly reduced fuel consumption, the diesel engine still has to meet the emission standards. Thanks to hybridization, a lower-power diesel engine can be used, and furthermore, the emissions regulations are not as strict with small engines as they are with higher-power diesels. That is why hybridization makes it easier to meet the emission standards.

1.3 Improving the energy efficiency of a mobile working machine

In mobile machines, work actions that require high forces, and in some cases, also the traction are implemented by hydraulics. Because of a high power density, the use of hydraulics is a key factor in mobile working machines [13]. Both the component and system designs affect the efficiency of a hydraulic system. The efficiencies of hydraulic components such as pumps, motors, hoses and valves have an impact on the efficiency of the hydraulic systems, but it is also important to consider how these components are combined to meet the load demands. Thus, the hydraulic circuit design is a very important element in mobile machine efficiency considerations [14].

In mobile machines, the hydraulics control is normally implemented by a load sensing (LS) system. A load sensing system is based on controlling a actuator by load-sensing hydraulic directional valves. The highest load sets the demand for the pump flow control [15]. The pump pressure is also determined by the highest pressure needed, and the volume flow is determined by the combined flow of the actuators [16]. If one of the actuators requires a high pressure and a small flow, and the other vice versa, the losses in the system become large. In most present-day machines there is no option for energy recovery because the pumps do not allow working as motors in different rotational directions. Therefore, lowering of the loads is carried out by proportional valves, which convert the system potential energy into heat thereby degrading the system energy efficiency.

When designing an energy efficient working machine, the hydraulic components should be replaced by ones allowing regenerative braking or lowering. The recovered energy must also be converted into useful energy in a suitable storage. In the case of electrical drives, the mechanical energy can be converted into electricity and stored in an electric energy storage. The hydraulic machines must be replaced by types capable of operating in two quadrants. The energy efficiency can be enhanced by improving the hydraulic systems. Pump control is an energy efficient way to control the positions of hydraulic cylinders (Fig. 1.2). The pump control means that the actuator is controlled directly by the flow of the pump without valves [13]. Pump control makes it possible to recover energy from the hoisting actuators. For example, in a wheel loader it is possible to achieve a ten percent improvement by using energy recovery systems [17].

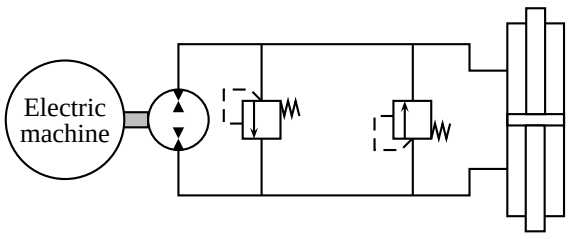

Fig. 1.2: Schematic of a pump-controlled symmetrical cylinder [16]. Asymmetric systems are also an option but need more complicated compensation arrangements.

The energy efficiency of the traction system of a working machine can be improved. In large working machines such as mine loaders and wheel loaders, hydrodynamic power transmission with a torque converter and a gearbox is traditionally employed. Smaller working machines and harvesters with a diesel engine below 100 kW typically apply hydrostatic power transmission with a hydraulic pump, a hydraulic motor and a gearbox instead [18]. Kohmäscher et al. [19] have presented different configurations of working machine traction systems. The efficiencies of different traction systems vary in the range of 60–88% [20]. Energy recovery and reuse are possible also in a mobile machine traction drive. Ancia and Achten [21], [22] have described a hydrostatic traction system based on the use of a hydraulic accumulator, in which braking energy recovery is possible. The University of Karlsruhe has studied hybrid systems by adding a hydraulic accumulator in a traditional hydrostatic transmission. The system has shown a 15% improvement in the fuel consumption [23]. The focus of this doctoral thesis is on large mobile working machines, and thus, the work concentrates on hydrodynamic power transmission.

Figure 1.3 provides a Sankey diagram of the energy flows in a working machine. In a working machine, energy is required for the traction and the working hydraulics. The Sankey diagram is determined for machine loading consisting of repeated work cycles without long idle periods. The proportion of idle running is small; approx. 5%.

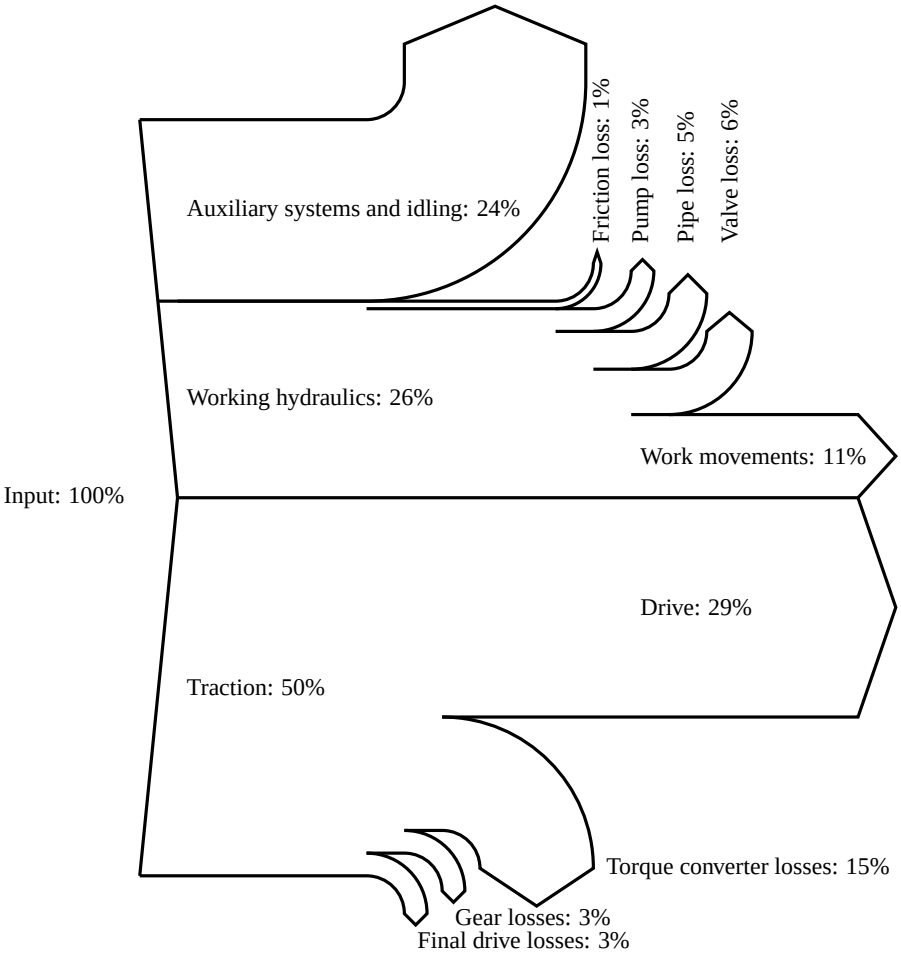

Fig. 1.3: Sankey diagram of a mobile working machine under a duty cycle with 5% idling. The input (100%) refers to the mechanical energy obtained from the diesel engine.

In the case of an example cycle, the input in the diagram refers to the mechanical energy obtained from the diesel engine. The figure shows that 40% of the energy given by the diesel engine is used in effective work, the losses account for 36% of the energy, and finally, idle running and auxiliary devices consume 24% of the energy. In original diesel-operated working machines, the energy wasted in losses is almost equal to the energy used in effective work. As the average energy efficiency of the diesel engine is about 30% in this case, the working efficiency of the machine is slightly higher than 10%. Hence, the energy efficiency of a working machine could be significantly improved.

Energy efficiency can be improved by replacing the components by new more efficient components that enable energy recycling, or by chancing the whole system architecture over to a more energy efficient one and by exploiting the opportunities of modern control systems [24].

In the field of hydraulic construction machinery, there are normally two kinds of hybrid systems: hydraulic hybrid [25] and electric hybrid (Fig.1.4) [26]. The hydraulic energy recovery system can also be implemented by hydraulic accumulator energy recovery systems [25], [27] or electric energy recovery systems [28], [29].

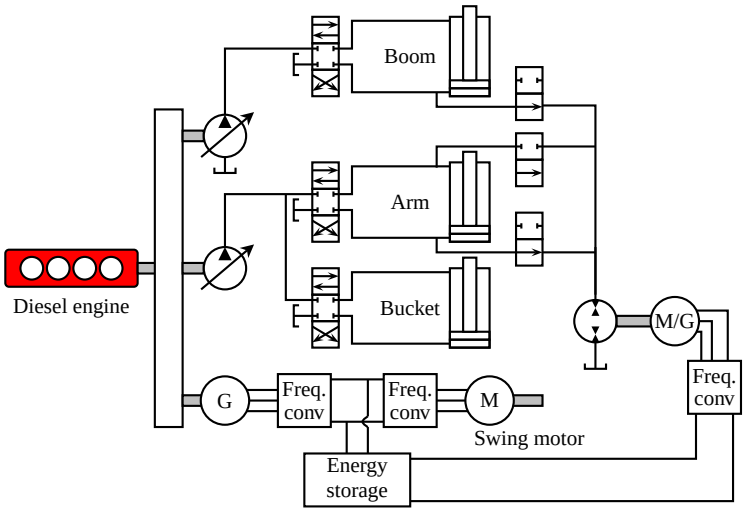

Fig. 1.4: Schematic of a hybrid excavator [26].

Interest in electric hybrid vehicles has arisen already in the 1990s [30], and a lot of research effort has been put into hybrid systems [31], [32]. However, the interest in hybrid working machines has increased significantly only in the late 2000s because of the tightening emissions regulations and rising fuel prices.

Hybrid drive systems for mobile working machines have been studied mainly with respect to cranes and construction machines [26] such as excavators and wheel loaders. Kim and Sul [33] and Mulder [34] have investigated the control and energy management in a series hybrid drive system for a rubber-tyred gantry (RTG) crane, which consists of a diesel generator set and a supercapacitor. Within the studied RTG crane, the fuel consumption was reduced by 35–50%.

In particular, the hybridization of excavators has been studied from the perspective of construction machines. Different electro-hydraulic hybrid structures have been presented and compared in [25], [28] and [29]. Kwon et al. [28] compare parallel, series and compound type hybrid excavators with supercapacitors and propose a power control algorithm of the engine and the supercapacitor. The achieved fuel savings vary from 12% to 55% depending on the hybrid structure. Moreover, the payback times of different hybrid systems are studied. The series hybrid seems to be the most expensive one, and also the payback time is the longest [28]. Xiao et al. [35] have presented an engine double-work-point control strategy in a parallel hybrid system with a supercapacitor. However, the double-work-point control strategy cannot meet the higher requirement for fuel efficiency, and therefore, a multi-work-point control strategy with four work points is presented in [36].

The modelling and energy management of hybrid electric trucks have also been studied. A procedure for the design of a near-optimal power management system for a parallel hybrid electric truck is presented in [37]. Kessels et al. [38] have presented an optimal control strategy that incorporates not only the energy management but also the emissions management in a series hybrid electric truck. Hou et al. [39] have developed a parallel hybrid electric truck simulation model and designed static and dynamic power management optimization algorithms. The power management algorithms are analysed, and with these algorithms, the fuel economy is several tens of percents better than that of a conventional diesel truck. Depending on the capacity of an electric storage in a hybrid drive, a diesel engine can be made run with a good control in its best operating range. In addition, the storage of electric energy is possible.

Commercial hybrid mobile working machines are still quite rare in the market. Hybrid forest machines available are for instance the hybrid harvester 910 EH by Prosilva, which is claimed to provide 40% less energy consumption [40], and the Elforest B12 and F15 series hybrid tractors [41]. There are also earth-moving machines such as the Komatsu HB215LC-1 excavator, in which the swinging motion is provided by an electric drive capable of energy recovery. A supercapacitor is used as an energy storage [42]. Catepillar also produces a hybrid excavator Cat 336EH, which is stated to be 25–33% more energy efficient than the previous models and provide a one-year payback period [44]. Straddle carriers are also available as hybrids; for instance, the Kalmar ESC W series straddle carrier can be equipped with a hybrid module, which offers 25–30% fuel savings compared with traditional models [43].

Improving the energy efficiency of mobile working machines is not a straightforward problem but depends on several factors. Obviously, a manufacturer cannot develop solutions that are not affordable to their customers. The payback period must, in practice, be less than three years in all cases. A mobile machine is used normally for 800–4000 hours a year. Beck et al. have compared the fuel consumptions and annual working hours of different applications in [44]. For example a harvester operates between 2000–3000 hours a year depending on the working principle, that is, whether the machine is used in one or two shifts a day. The lifetime of the main components is calculated to be about 10 years [13].

1.4 Load cycle of a mobile working machine

Some vehicle applications have standardized cycles, on which for example the marketing information is based and the vehicles can be operated. Mobile working machines do not have a common general standard work cycle. It may be difficult to define such a cycle as the working environments and load cycles vary significantly between machines. Mobile working machines can be divided for instance into forest, mine, farming, building and terminal machines. However, when designing an energy-efficient hybrid mobile machine, it is not possible to define the most suitable hybridization system based on the application field alone. From the perspective of energy efficiency, the load cycle is much more important than the application field.

Mobile machine cycles can be divided for instance into

- high constant loads
- manipulation loads
- transport loads

High constant loads can be observed for example for tractors and bulldozers, which either pull or push heavy loads. Manipulation cycles can be found in machines with several actuators, such as in harvesters. In manipulation systems, high load variations are typical. In several manipulating machines also transportation cycles are present.

A load cycle can comprise no-load, acceleration, constant speed, braking, lifting and lowering cycles. Rotational movements are also possible for instance in excavators. Further, loads can be divided into repeatable cycles.

Figure 1.5 illustrates two totally different manipulation load cycles. In Fig. 1.5a, the cycle contains periods where energy can be recovered and the power variations are slight. In Fig. 1.5b, the cycle does not contain periods during which it could be possible to recover energy, and hence, the load varies much more than in Fig. 1.5a.

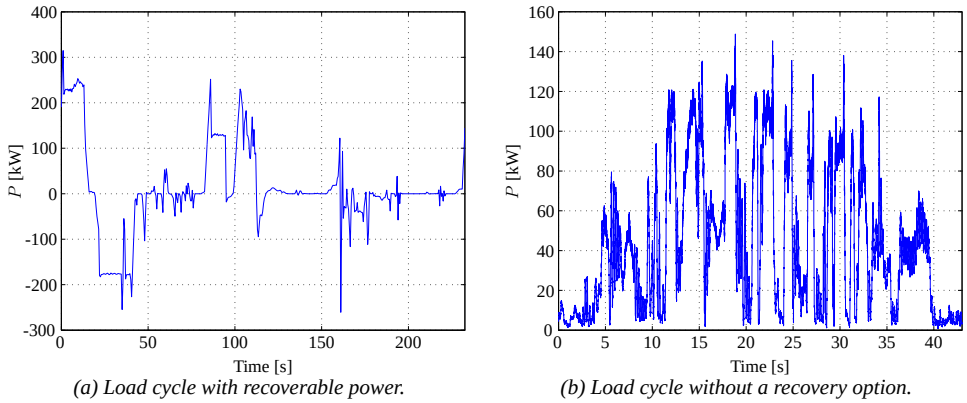

(a) Load cycle with recoverable power. *(b) Load cycle without a recovery option.*

Fig. 1.5: Example load cycles of goods manipulating machines during one repeatable cycle.

In cars and buses, the internal combustion engine is mainly needed to move the vehicle and auxiliary systems. In mobile working machines instead there are, in addition to traction, work movements that are delivered by several actuators. Figure 1.6a shows the power needed in a car as a function of time in NEDC (New European Driving Cycle) and the distribution of power during loading. Figure 1.6b shows the load demand of a mobile machine as a function of time and the power demand during the loading of the machine.

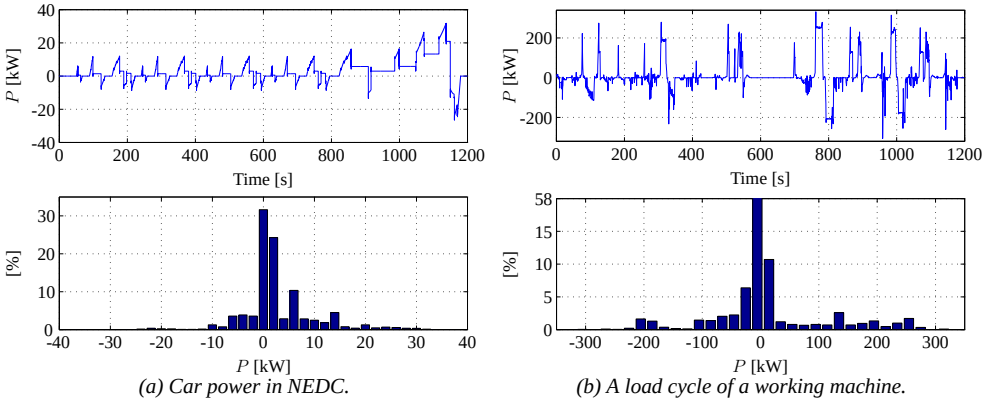

(a) Car power in NEDC. *(b) A load cycle of a working machine.*

Fig. 1.6: Car and working machine power as a function of time and the power distribution.

In construction machinery, the load change rate and amplitude are much larger compared with cars [45], [46]. In cars the braking energy is the highest recoverable energy whereas in working machines the largest proportion of recoverable energy is generated by actuators. The amount of regenerated energy is often significant and varies rapidly [47]. The example machine shows, however, that despite the high power peaks a working machine can operate at no load more than half of the running time. The average power is, therefore, low compared with the peak power.

1.5 Outline of the thesis

The objective of the work is to describe the hybridization process of a working machine starting from the selection of the type of the hybrid system. The main target in hybridization is to efficiently reduce the fuel consumption of the working machine. However, different hybridization arrangements result in different prices for hybridization and thereby also in different savings. In this work, the hybridization alternatives have been limited to three main principles:

1. Pure parallel hybrid system where both the traction and hydraulic drives are implemented by using a parallel hybrid system. This is the simplest one resulting in minor changes in a present-day working machine and is therefore favoured by the machine manufacturers.
2. Parallel-series hybrid system in which the working machine hydraulics is implemented by the parallel hybrid principle and the traction by the series hybrid principle.
3. Pure series hybrid system in which all the functions of the machine are implemented by the series hybrid principle. In this case, the working machine must be redesigned as all the functions are delivered by electric drives.

General guidelines for hybridization are given. The effects of the hybridization principle in the fuel consumption are studied in detail by using different components in the preliminary designs of a hybrid machine. In the case of the series hybrid system, the effect of the energy storage capacity is studied in detail by altering the power capability and the capacity of the storage in the designs.

The work comprises five chapters. The introduction gives an overview of the motivation of hybridization and the objectives to improve the energy efficiency and working cycles of the machines.

Chapter 2 introduces the components of a simulation model for a mobile working machine and algorithms to estimate the efficiencies of electrical machines. The algorithms have been developed in co-operation with Dr. Vesa Ruuskanen. Some measurements verifying an induction machine performance in a traction drive are also made. The efficiency measurements for the induction machine have been made by Dr. Lassi Aarniovuori. The hydraulics of the working machine is not modelled in detail, but the power needed by the hydraulic drives has been modelled separately at the Department of Intelligent Hydraulics and Automation at Tampere University of Technology (TUT IHA). The power curves for the working hydraulics have been determined by Ville Ahola, M.Sc. and Janne Uusi-Heikkilä, M.Sc.

Chapter 3 describes how the components introduced in Chapter 2 are used to construct a working machine simulation model for parallel, parallel-series and series hybrid drives. The most important control principles of the system are also introduced and discussed.

Chapter 4 demonstrates an actual working machine as an example of hybridization. The dimensioning of the components and several simulation results are given to show the effects of different components on the performance and energy efficiency of the system. The system's return on investment is also evaluated.

Chapter 5 concludes the work and suggests topics for further study.

1.6 Scientific contributions

1. Development of a comprehensive model of a working machine energy flow in different hybridization alternatives.
2. Analysis on the effects of the diesel and energy storage dimensions on the fuel consumption in different hybridization alternatives.
3. Construction of a method to determine the optimum dimensioning of the energy storage in a series hybrid system.
4. Analytical algorithm to evaluate a permanent magnet synchronous machine or induction machine efficiency starting from the equivalent circuit parameters and obtaining the results in a torque–speed co-ordinate system applying different control principles.

1.7 Most relevant scientific publications related to the doctoral thesis

V. Ruuskanen, P. Immonen, J. Nerg and J. Pyrhönen, "Determining Electrical Efficiency of Permanent Magnet Synchronous Machines with Different Control Methods," *Electrical Engineering (Archiv für Elektrotechnik)*, vol. 94 no. 2 pp. 97–106, Jun. 2012.

P. Immonen, L. Laurila and J. Pyrhönen, "Modelling of a diesel-electric parallel hybrid drive system in Matlab Simulink," *International Review of Modelling and Simulations (IREMOS)*, vol. 2. no. 5, pp. 565–572, Oct. 2009.

P. Immonen, L. Laurila, M. Rilla and J. Pyrhönen, "Modelling and simulation of a parallel hybrid drive system for mobile work machines," in *Proc. IEEE Eurocon*, May 2009, St. Petersburg, Russia.

Chapter 2

Subsystem components of hybrid work machine simulation model

A hybrid working machine model is prepared by combining all the component models together. This way, a modular model is obtained, and it will be easy to modify the model by changing just one component inside the entire model based on the needs of different machines and different hybridization principles. The partial models needed depend on the working machine type and its hybridization.

In a traction drive, the important model components to be listed are: the torque converter model, the gearbox model, the transmission parts model and the model of the dynamics of the machine. In addition to the traction drive, a working machine has hydraulic actuators. These actuators are not modelled in this work, but the model requires the power curves of the actuators. The power demand is also determined for the working hydraulics used in the hybrid systems; the hydraulics is implemented by pump-motor units that enable energy recovery and reuse. The electric parts of the model comprise for instance the electric drives consisting of motors and power electronic converters and an energy storage. The storage can be either a battery or a supercapacitor, or both. In this doctoral thesis, the term 'battery' refers to a rechargeable (secondary) battery (aka accumulator) used as a source of energy. The focus of this thesis is on the case where the energy storage is connected directly without a DC-DC converter to the DC link. The advantage of this approach is that there will be no DC-DC-converter losses either. A drawback, again, is that the voltage of the energy storage must be suitable for direct DC link connection. The mechanical power source in a mobile machine is a diesel engine.

The modelling is based on energetic macroscopic representation (EMR), which is an energy-flow-based graphical modelling tool to illustrate the energy flow in a complex electromechanical system. The EMR is based on an action-reaction principle to organize the interconnections of subsystems according to the physical causality (system modelled by an integral equation) [48], [49]. The subsystem components and the hybrid systems are illustrated

graphically by using the EMR presentation. The EMR presentation is suitable for describing complex electromechanical systems [49]. The basic elements of the EMR are shown in Fig. 2.1. This chapter presents the component modelling and verification of some the component models.

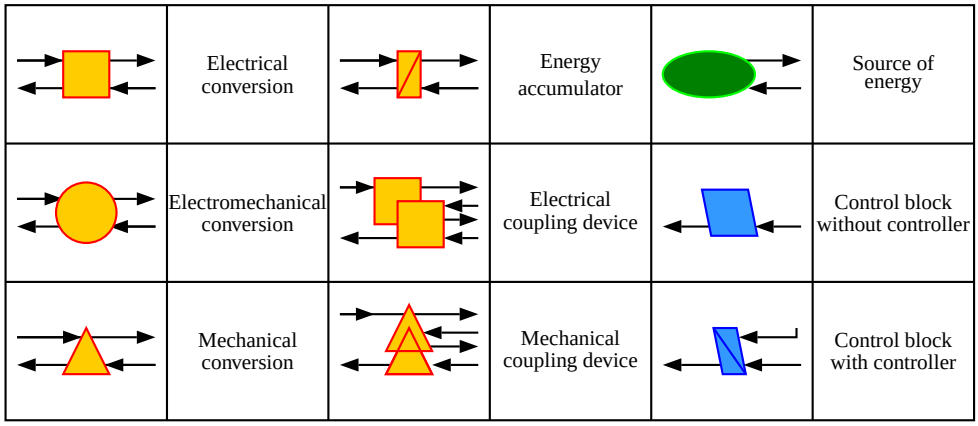

Fig. 2.1: Basic elements of the EMR [50].

2.1 Electric drive

When modelling an electric drive, either a dynamic or quasi-static model can be used. With dynamic modelling, also the converter model has to be included. The benefit of the dynamic modelling is that the control of the machine can be designed and tested by applying the model. The electrical machine behaviour can be analysed both in transient and steady states. The difficulties of the dynamic modelling are its complexity and the long calculation time needed to analyse a larger machine system. Figure 2.2 provides the EMR model of the electric drive.

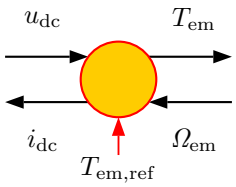

Fig. 2.2: Energetic macroscopic representation (EMR) of an electric drive model. T_{em} is the torque and Ω_{em} is the angular velocity of the electrical machine, u_{dc} is the DC voltage, i_{dc} the DC current and $T_{\mathrm{em,ref}}$ the reference value of the electrical machine torque.

In the quasi-static model, the electric motor is modelled in a straightforward manner by only using a first- or second-order time constant model. The torque of the electrical machine is assumed to follow the torque reference limited by the maximum torque curve and delayed by a first-order time constant filter. The DC current needed by the electric drive

$$i_{\mathrm{dc}} = \frac{T_{\mathrm{em}}\,\Omega_{\mathrm{em}}}{\eta_{\mathrm{ed}}^{c}\left(\Omega_{\mathrm{em}}, T_{\mathrm{em}}\right) u_{\mathrm{dc}}}, \tag{2.1}$$

is calculated by using the efficiency of the electric drive η_{ed}. The efficiency of the electric drive consists of the efficiencies of the converter and the motor. The power multipler c depends on the power flow direction, if the power is transmitted from the energy storage to the electric motor, $c = 1$, and if the power tries to flow in the opposite direction, $c = -1$. The converter and motor efficiencies are determined in advance for different speeds and torque levels. With the quasi-static model it is possible to study the energy flows in an electric drive both in the steady states and transients. The accuracy of the quasi-static model depends on the accuracy of the efficiency map and the correctness of the electric motor time constant. The accuracy of the efficiency map is very much dependent on the number of the operating points calculated when preparing the map. The more points are included, the better the map will be. The benefit of the quasi-static model is that it yields a significantly shorter calculation time compared with the dynamic model. However, it is emphasized that calculation of the efficiency maps takes time. Despite the relatively simple electrical machine modelling, the quasi-static models can be used without significant errors if the efficiency map is accurate enough [51], [52]. Efficiency maps have been used for instance in [53] and [54] to evaluate and optimize the energy consumption in a mobile drive. Figure 2.3 describes the construction of a quasi-static model.

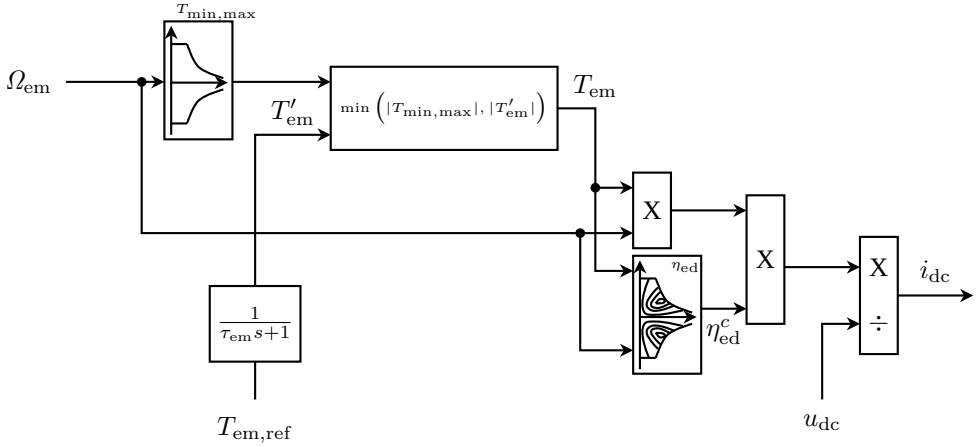

Fig. 2.3: Quasi-static model of an electric drive. The $T_{\mathrm{min,max}}$ block contains information of the minimum and maximum torque curves of the electric machine, and τ_{em} is the electromechanical conversion time constant of the electric machine.

In this doctoral thesis, a quasi-static model of an electrical machine is used in the simulations. In the electrical machine models, constant parameters are used, taking into account only the saturation behaviour of the magnetizing inductance of the induction machine and the dependency of the iron loss resistance on frequency. In reality, the inductances of the electrical

machine saturate and cross-saturate, and consequently, the saturation behaviour has an effect on the machine efficiency [55]. Further, the rotor resistance of the induction machine varies as a function of slip frequency, which again has an impact on losses [56]. Hence, because of the use of constant parameters in the machine model, the actual losses and efficiency of an electrical machine may deviate somewhat from the model. However, the quasi-static model of an electrical machine is commonly used in the modelling and analysis of electro-hybrid vehicles at a system level [52], [57]. A quasi-static constant parameter model can be applied to analyse hybrid options at a system level; however, if the behaviour of an electrical machine in a hybrid system has to be studied in more detail, a dynamic model has to be used taking parameter variation into account.

2.1.1 Permanent magnet synchronous machines

Dynamic model

The permanent magnet synchronous machine (PMSM) is modelled by applying the space vector theory, which enables modelling and simulating of the transient states of the machine. Such an approach is not acceptable in the RMS phasor presentation of AC machines. Traditionally, the iron losses are neglected in the space vector theory to simplify the presentation. In this case, the iron losses are modelled as the energy efficiency studies make it necessary to observe these losses. The PMSM is modelled in the rotor co-ordinate system. Figure 2.4 depicts the direct- and quadrature-axis vector equivalent circuits of the PMSM without damper windings but equipped with iron loss resistances [58].

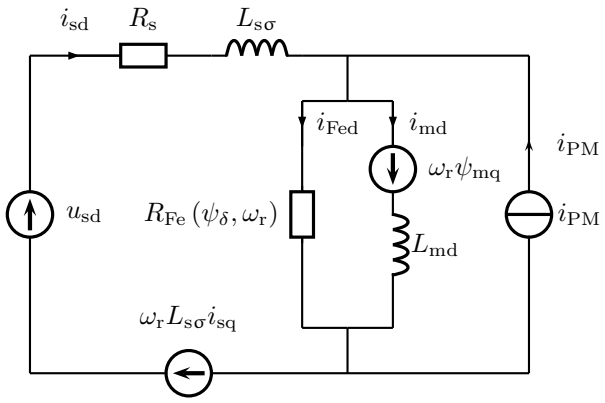

(a) Direct axis

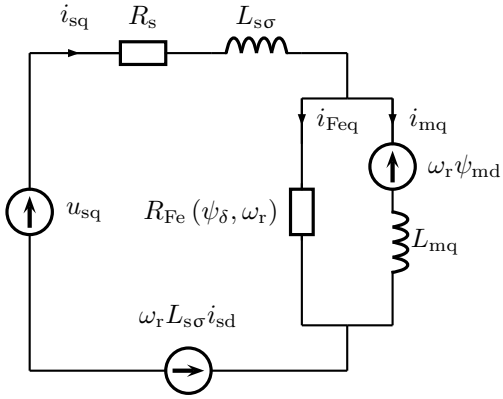

(b) Quadrature axis

Fig. 2.4: Direct- and quadrature-axis equivalent circuits of the PMSM. u_{sd} and u_{sq} are the stator direct- and quadrature-axis voltages, i_{sd} and i_{sq} the direct- and quadrature-axis currents, i_{Fed} and i_{Feq} the direct- and quadrature-axis iron loss currents, i_{md} and i_{mq} the direct- and quadrature-axis magnetizing currents, R_{s} the stator resistance, $L_{\mathrm{s}\sigma}$ the stator leakage inductance, R_{Fe} the iron loss resistance, L_{md} and L_{mq} the direct- and quadrature-axis magnetizing inductances, ψ_{md} and ψ_{mq} the direct- and quadrature-axis magnetizing flux linkages, ω_{r} the rotor angular frequency and i_{PM} the virtual permanent magnet current source producing the permanent magnet flux linkage in the magnetizing inductance.

When the iron losses are modelled with a resistor parallel to the magnetizing inductance in the space vector equivalent circuit, the iron loss current has to be separated from the current that passes through the magnetizing inductance and produces the air gap flux linkage that is capable of producing torque. Figure 2.5 depicts the vector diagram of a salient pole PMSM.

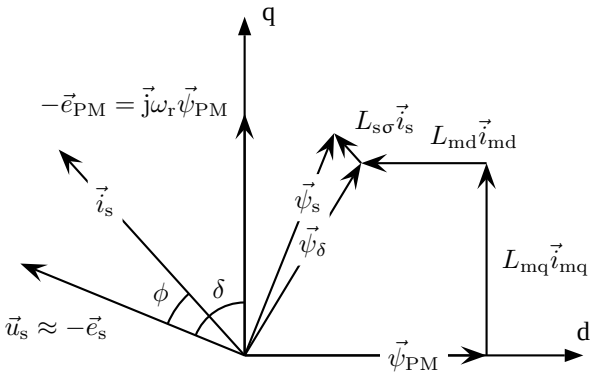

Fig. 2.5: Salient pole PMSM phasor diagram at nominal speed and torque.

In the vector diagram, the presence of iron losses can be observed from the fact that the air gap flux linkage space vector $\vec{\psi}_{\delta}$ is generated by the flux linkage $\vec{\psi}_{\mathrm{PM}}$ produced by the permanent magnet, the magnetizing inductances (L_{md} and L_{md}) and the magnetizing current components ($\vec{i}_{\mathrm{md}}$ and $\vec{i}_{\mathrm{mq}}$). The steady-state stator current does not completely travel through the magnetizing inductance as in the iron lossless case producing flux linkage, but a part of it travels through the iron loss resistance.

For control purposes instead, the proportion of iron losses is negligible. Figure 2.6 illustrates the PMSM dynamic model according to the EMR presentation.

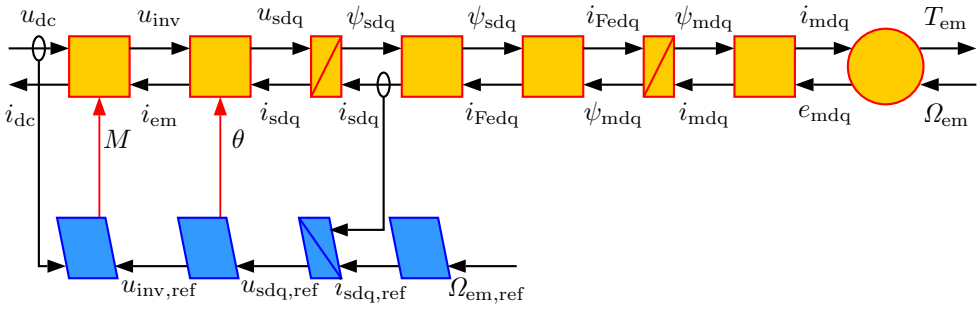

Fig. 2.6: Model of a PMSM according to the EMR. u_{inv} is the inverter voltage, i_{em} the electric machine current, u_{sdq} the stator voltage, i_{sdq} the stator current, ψ_{sdq} the stator flux , i_{Fedq} the iron loss current, ψ_{mdq} the magnetizing flux linkage, i_{mdq} the magnetizing current, e_{mdq} the stator electromotive force, M the modulation index and θ the rotor angle.

The voltage equations of the PMSM in the rotor co-ordinate system are

$$u_{\mathrm{sd}} = R_{\mathrm{s}} i_{\mathrm{sd}} + \frac{\mathrm{d}\psi_{\mathrm{sd}}}{\mathrm{d}t} - \omega_{\mathrm{r}}\psi_{\mathrm{sq}}, \tag{2.2}$$

$$u_{\mathrm{sq}} = R_{\mathrm{s}} i_{\mathrm{sq}} + \frac{\mathrm{d}\psi_{\mathrm{sq}}}{\mathrm{d}t} + \omega_{\mathrm{r}}\psi_{\mathrm{sd}}. \tag{2.3}$$

The stator and magnetizing flux linkages are

$$\psi_{\mathrm{sd}} = L_{\mathrm{sd}} i_{\mathrm{sd}} - L_{\mathrm{md}} i_{\mathrm{Fed}} + \psi_{\mathrm{PM}}, \tag{2.4}$$
$$\psi_{\mathrm{sq}} = L_{\mathrm{sq}} i_{\mathrm{sq}} - L_{\mathrm{mq}} i_{\mathrm{Feq}} \tag{2.5}$$

$$\psi_{\mathrm{md}} = L_{\mathrm{md}} \left(i_{\mathrm{sd}} - i_{\mathrm{Fed}} \right) + \psi_{\mathrm{PM}}, \tag{2.6}$$
$$\psi_{\mathrm{mq}} = L_{\mathrm{mq}} \left(i_{\mathrm{sq}} - i_{\mathrm{Feq}} \right) \tag{2.7}$$

where the d-axis inductance $L_{\mathrm{sd}} = L_{\mathrm{s}\sigma} + L_{\mathrm{md}}$ and the quadrature axis inductance $L_{\mathrm{sq}} = L_{\mathrm{s}\sigma} + L_{\mathrm{mq}}$.

The stator and iron loss currents can be solved based on the flux linkage equations

$$i_{\mathrm{sd}} = \frac{\psi_{\mathrm{sd}} - \psi_{\mathrm{PM}} + L_{\mathrm{md}} i_{\mathrm{Fed}}}{L_{\mathrm{sd}}} \tag{2.8}$$
$$i_{\mathrm{sq}} = \frac{\psi_{\mathrm{sq}} + L_{\mathrm{mq}} i_{\mathrm{Feq}}}{L_{\mathrm{sq}}} \tag{2.9}$$

$$i_{\mathrm{Fed}} = \frac{\psi_{\mathrm{md}} - \frac{L_{\mathrm{md}}}{L_{\mathrm{sd}}} \psi_{\mathrm{sd}} + \left(\frac{L_{\mathrm{md}}}{L_{\mathrm{sd}}} - 1 \right) \psi_{\mathrm{PM}}}{\frac{L_{\mathrm{md}}^2}{L_{\mathrm{sd}}} - L_{\mathrm{md}}} \tag{2.10}$$
$$i_{\mathrm{Feq}} = \frac{\psi_{\mathrm{mq}} - \frac{L_{\mathrm{mq}}}{L_{\mathrm{sq}}} \psi_{\mathrm{sq}}}{\frac{L_{\mathrm{mq}}^2}{L_{\mathrm{sq}}} - L_{\mathrm{mq}}} \tag{2.11}$$

The air gap flux linkage is solved with the iron loss current from the air gap voltage equation as

$$u_{\mathrm{md}} = \frac{\mathrm{d}\psi_{\mathrm{md}}}{\mathrm{d}t} = R_{\mathrm{Fe}} i_{\mathrm{Fed}} + \omega_{\mathrm{r}} \psi_{\mathrm{mq}} \tag{2.12}$$
$$u_{\mathrm{mq}} = \frac{\mathrm{d}\psi_{\mathrm{mq}}}{\mathrm{d}t} = R_{\mathrm{Fe}} i_{\mathrm{Feq}} - \omega_{\mathrm{r}} \psi_{\mathrm{md}}. \tag{2.13}$$

The electromagnetic torque according to the Lorentz force is calculated by the flux linkage and stator current cross product as

$$T_{\mathrm{em}} = \frac{3p}{2}|\vec{\psi}_{\mathrm{s}} \times \vec{i}_{\mathrm{m}}| = \frac{3p}{2}(\psi_{\mathrm{sd}} i_{\mathrm{mq}} - \psi_{\mathrm{sq}} i_{\mathrm{md}}). \tag{2.14}$$

By writing the flux linkage components ψ_{sd} and ψ_{sq} by currents and inductances, it is possible to write Eq. (2.14) into the form

$$T_{\mathrm{em}} = \frac{3p}{2}\left[(L_{\mathrm{sd}} - L_{\mathrm{sq}})\, i_{\mathrm{md}} i_{\mathrm{mq}} + \psi_{\mathrm{PM}} i_{\mathrm{mq}}\right]. \tag{2.15}$$

The rotating movement differential equation can be used to solve the speed of a motor

$$T_{\mathrm{em}} = T_{\mathrm{load}} + J\frac{\mathrm{d}\Omega_{\mathrm{em}}}{\mathrm{d}t} + B\Omega_{\mathrm{em}} \tag{2.16}$$

T_{load} is the load torque, J the moment of inertia, Ω_{em} the mechanical angular velocity and B the friction coefficient of the rotating movement. The mechanical angular velocity Ω_{em} and the rotor electrical angular frequency ω_{r} are linked by

$$\omega_{\mathrm{r}} = p\Omega_{\mathrm{em}}, \tag{2.17}$$

where p is the number of pole pairs.

Quasi-static model

The quasi-static model needs the efficiency map and maximum torque curve of the PMSM as inputs. The efficiency map can be supplied by the motor manufacturer or it must be defined during the design phase by the designer of the working machine based on the electrical machine parameters [59]. The efficiency map of a PMSM is defined here by using the above-mentioned vector equivalent circuit to which the effect of iron losses has been added. The voltage equations (2.2) and (2.3) in the rotor co-ordinate system in the steady state are

$$u_{\mathrm{sd}} = R_{\mathrm{s}} i_{\mathrm{sd}} - \omega_{\mathrm{r}} \psi_{\mathrm{sq}} \tag{2.18}$$

$$u_{\mathrm{sq}} = R_{\mathrm{s}} i_{\mathrm{sq}} + \omega_{\mathrm{r}} \psi_{\mathrm{sd}}, \tag{2.19}$$

where the flux linkages ψ_{sd} and ψ_{sq} have been defined by Eqs. (2.4) and (2.5). The PMSM torque, voltages, currents and losses have been calculated at different angular frequencies ω_{r} and with different magnetizing current combinations (i_{md}, i_{mq}). It is pointed here that constant inductance values will result in erroneous torque values at high torques. It is, naturally, possible to take the saturation and cross-saturation phenomena into account if the inductances have been defined accordingly, as for instance in [55]. Figure 2.7 provides the flow chart of the calculation of the PMSM efficiency.

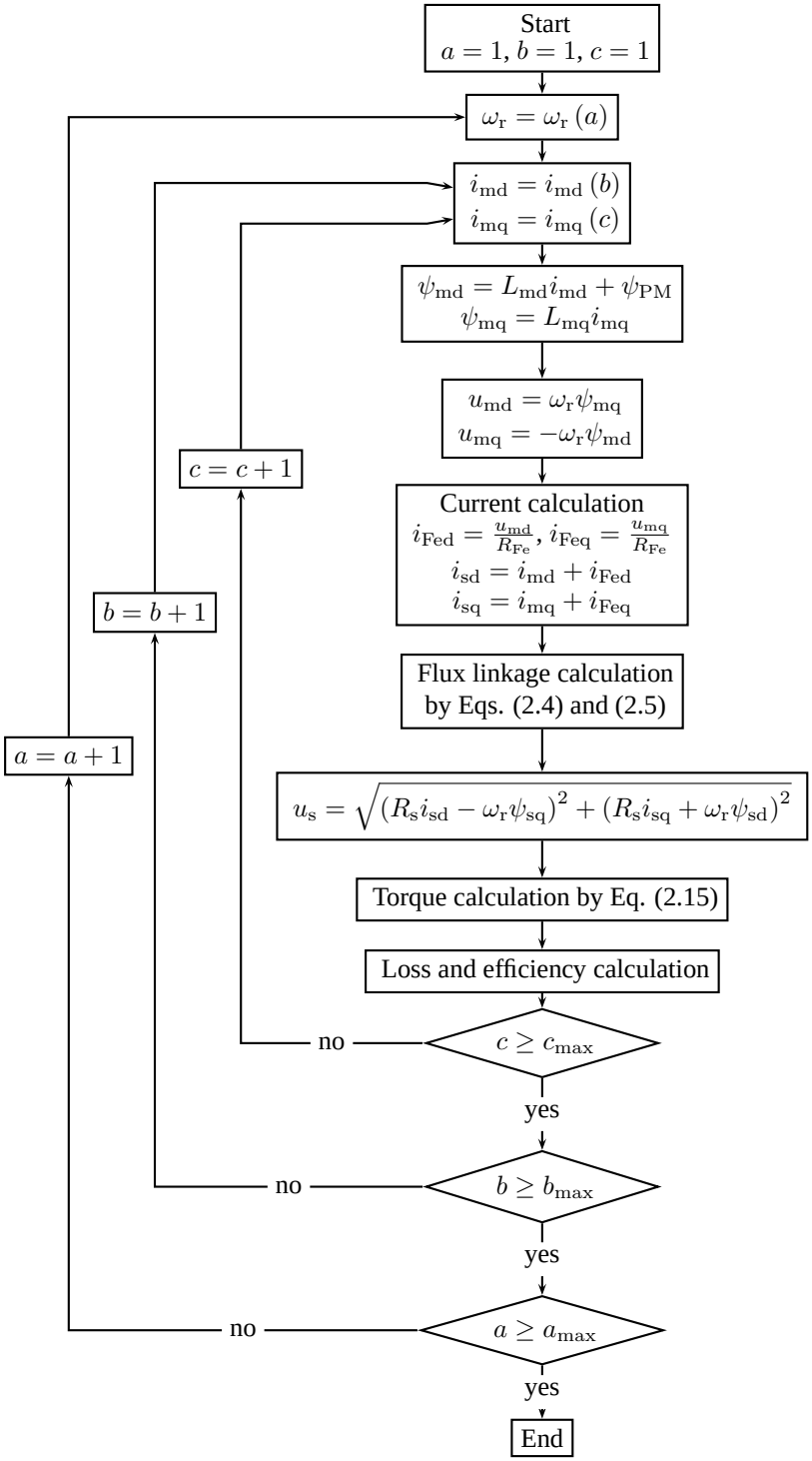

Fig. 2.7: Flow chart for determining the efficiency chart of a PMSM.

In the loss calculation, the copper, iron and mechanical losses are taken into account. The iron losses can be calculated by using either the iron loss resistance R_{Fe} or by the Bertotti equation [60], if the iron loss resistance is not known but the machine magnetic circuit parameters are known. When the rated point iron loss resistance is known, the rated point iron losses can be calculated by $P_{\mathrm{Fe}} = \frac{3}{2} R_{\mathrm{Fe}} i_{\mathrm{Fe}}^2$, when the iron loss current i_{Fe} has been defined. In such a case, the iron loss current is automatically included in the stator current. The iron losses are frequency and air-gap flux dependent [61], and therefore, also the iron loss resistance is frequency dependent. The frequency dependent iron loss resistance is identified using the experimental procedure described in [62]. The mechanical losses comprise windage and friction losses [63]

$$P_{\mathrm{mec}} = k_{\mathrm{f}} \frac{\Omega_{\mathrm{em}}}{\Omega_{\mathrm{em,n}}} + k_{\mathrm{w}} \left(\frac{\Omega_{\mathrm{em}}}{\Omega_{\mathrm{em,n}}} \right)^3 , \tag{2.20}$$

where k_{f} is the friction coefficient, k_{w} the windage loss coefficient and Ω_{em} the mechanical angular velocity and $\Omega_{\mathrm{em,n}}$ the nominal mechanical angular velocity.

The calculation produces three-dimensional tables for the torque T_{em}, the voltage u_{s}, the current i_{s} and the efficiency η_{em} (Fig. 2.8), by which it is possible to determine the maximum torque curve of the PMSM and plot the efficiency map by picking up the efficiency values that meet the desired boundary conditions. The maximum torque curve and the efficiency map can be generated for instance by using a voltage u_{s} that equals the optimum or by using a constant flux linkage under the constraints of the maximum current or voltage levels available.

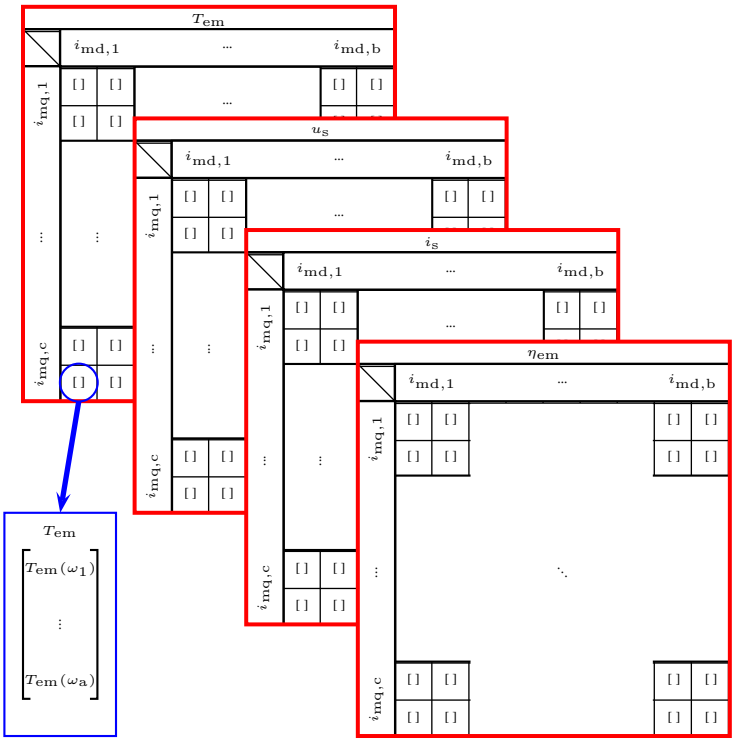

Fig. 2.8: Example of maps produced by the efficiency map calculation.

With the method introduced above, the efficiency of a case machine, the non-salient eight-pole 200 kW PMSM, is defined. The parameters of a case PMSM are presented in Table 2.1.

Table 2.1: 200 kW PMSM parameters for the efficiency calculation.

Nominal power	P_n	200 kW
Nominal voltage	U_n	400 V
Nominal current	I_n	330 A
Nominal frequency	f_n	100 Hz
Number of pole pairs	p	4
Nominal speed	n_n	1500 rpm
Permanent magnet flux linkage	ψ_PM	0.33 Vs
Stator resistance	R_s	3.72 mΩ
Stator leakage inductance	$L_\mathrm{s\sigma}$	0.10 mH
Stator direct-axis inductance	L_sd	0.258 mH
Stator quadrature-axis inductance	L_sq	0.258 mH
Friction loss coefficient	k_f	560 W
Windage loss coefficient	k_w	594 W

The iron loss resistance used to evaluate the efficiency map is a function of angular velocity as Fig. 2.9 illustrates for the constant stator flux level.

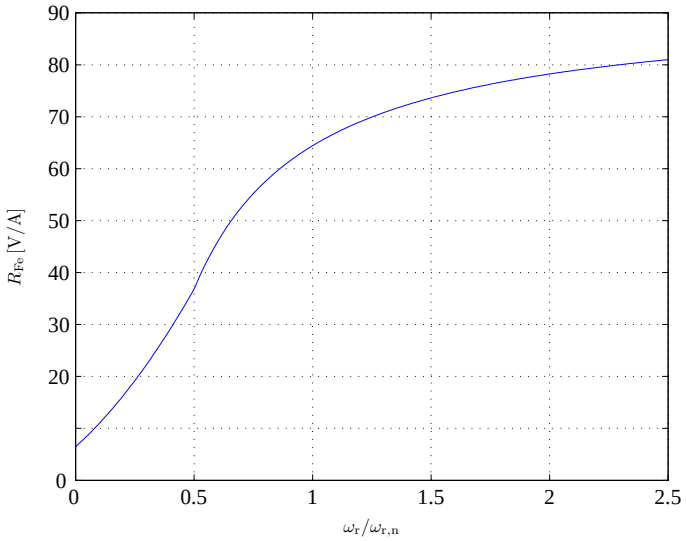

Fig. 2.9: Iron loss behaviour used in the efficiency map calculation with a constant stator flux level.

The efficiency map of the PMSM has been calculated by applying the optimum voltage principle. The maximum voltage has been 400 V and the maximum current 990 A. In the optimum voltage principle, the voltage producing the highest efficiency in each operating point is selected to minimize the losses. Figure 2.10 presents the efficiency map calculated by the above-mentioned principle.

The map is given for speeds ranging from zero to 2.5 times the rated speed and for torque levels between $-3T_\mathrm{n}$ and $+3T_\mathrm{n}$. The maximum efficiency of this machine is 0.98, and it is reached at the rated speed and at a torque slightly higher than the rated one.

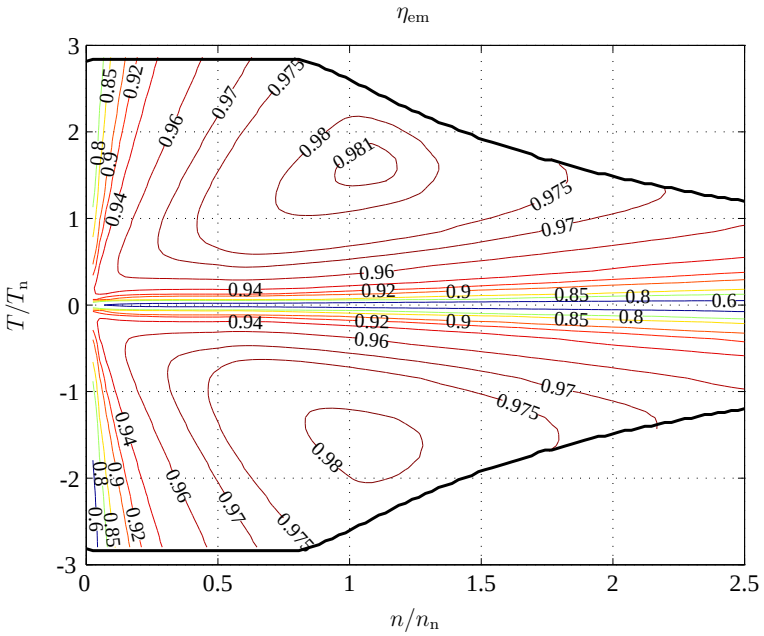

Fig. 2.10: Efficiency map of the PMSM with optimum voltage.

Figure 2.11 shows the optimum voltage, the corresponding current and the power factor.

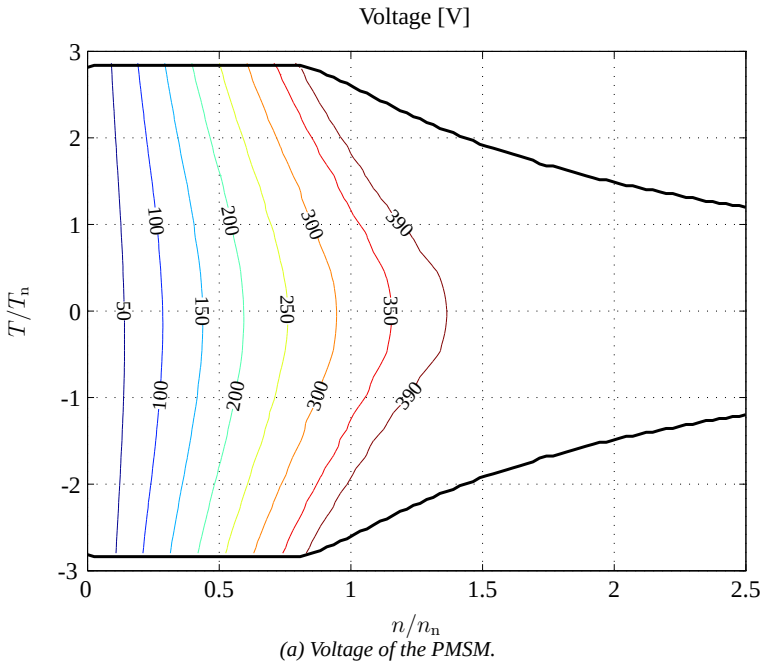

(a) Voltage of the PMSM.

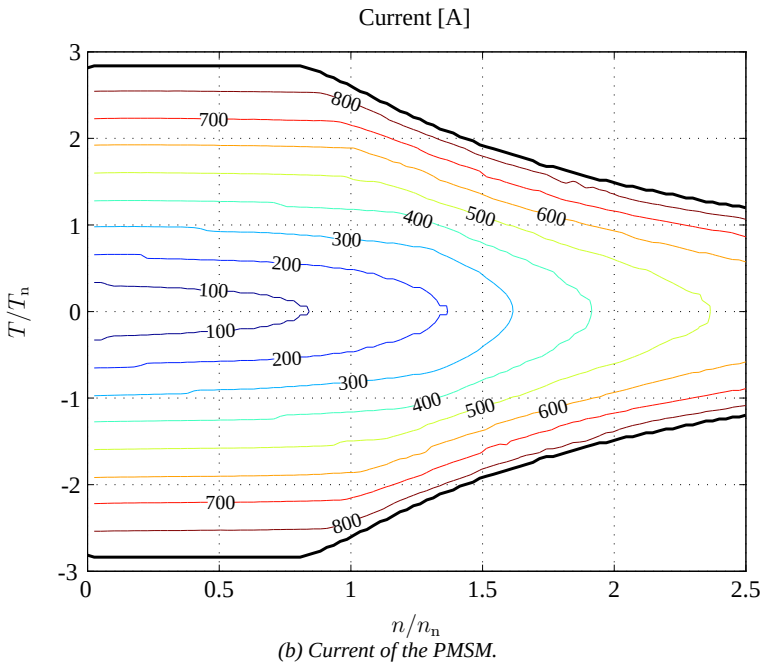

(b) Current of the PMSM.

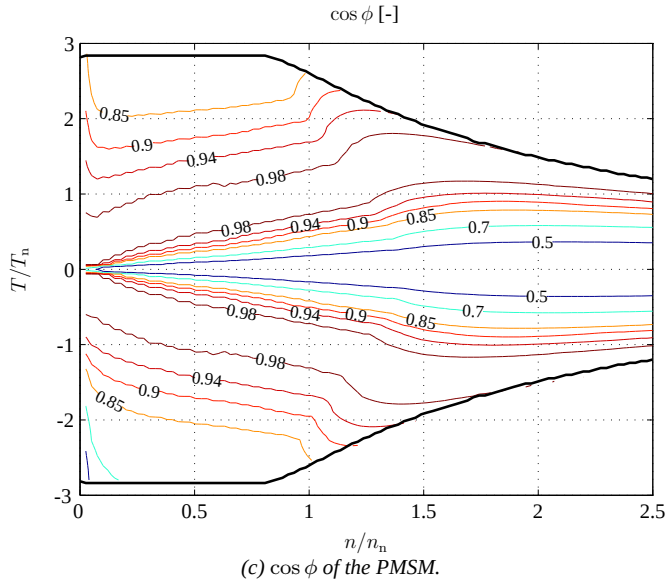

(c) $\cos\phi$ *of the PMSM.*

Fig. 2.11: Voltage, current and $\cos\phi$ *of the PMSM with the optimum voltage.*

The optimum voltage resulting in the maximum efficiency increases as a function of speed and torque. In the rated point, the voltage is about 350 V, which is 0.87 times the rated voltage. The current behaviour shows increasing values as the speed increases, as there is a need for the demagnetizing d-axis current. The voltage available naturally affects the maximum value of torque. Figure 2.12 shows the torque of the PMSM normalized to 1 at different speeds with different voltages (the rated torque is normalized to 1, even though the per unit torque of a machine with $\psi_\mathrm{s} = 1$ and $i_\mathrm{s} = 1$ is normally less than 1).

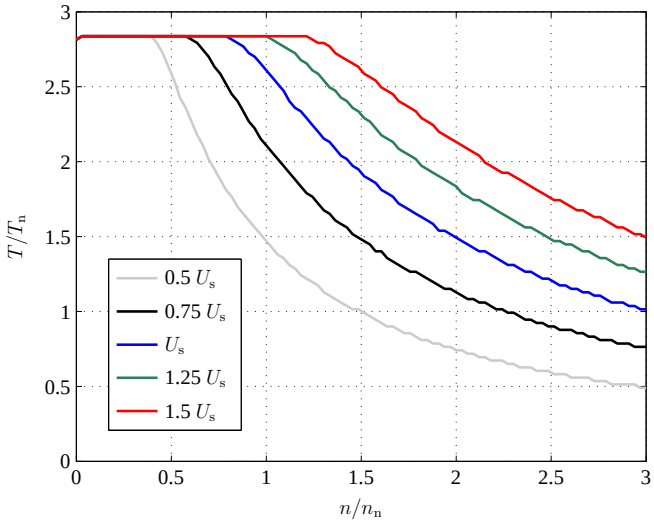

Fig. 2.12: Maximum torque of the PMSM with different stator voltages.

Figure 2.13 demonstrates how the maximum torque is limited by the converter maximum current $i_{\mathrm{inv,max}}$, the voltage of the energy storage u_{dc} and the magnetic circuit saturation.

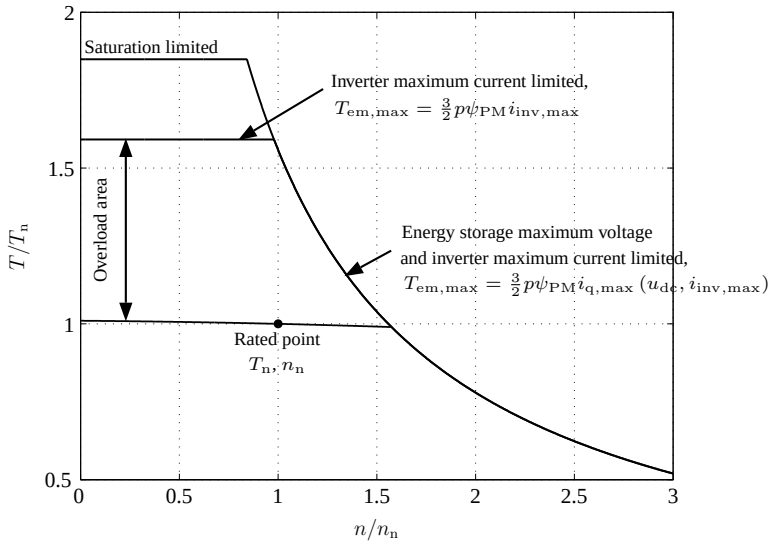

Fig. 2.13: Maximum torque of the non-salient pole PMSM.

At low speeds, the PMSM maximum torque is limited by the maximum converter current and the magnetic circuit saturation. If infinite current were available, a maximum torque level should be found anyway because of the magnetic circuit saturation. The voltage of the energy storage limits the torque at higher speeds. The voltage available also affects the electrical machine efficiency. At higher speeds in particular, a high voltage results in a higher efficiency than a low voltage, because with a high voltage the need for demagnetizing is smaller. Hence, it is important to observe how the voltage affects the machine performance. It must be remembered that it is not possible to give the maximum torque curve for the electrical machine alone, but the maximum torque of a drive also depends on the converter current capability and the voltage of the energy storage.

Dynamic vs. quasi-static model

Dynamic- and quasi-static-model-based energy efficiency calculations for a PMSM have been compared in a system illustrated in Fig. 2.14. Table 2.2 lists the efficiencies obtained by the dynamic and quasi-static models. In the quasi-static case, efficiency maps with different resolutions have been used.

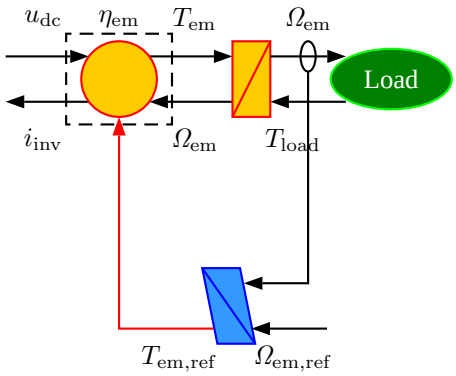

Fig. 2.14: Modelling of the electrical machine efficiency.

Figure 2.15 illustrates the reference value for $\Omega_{\mathrm{em,ref}}$ normalized to the rated speed and the torque of the load T_{load} normalized to the rated torque of the electrical machine. The efficiency analysis is carried out applying these values.

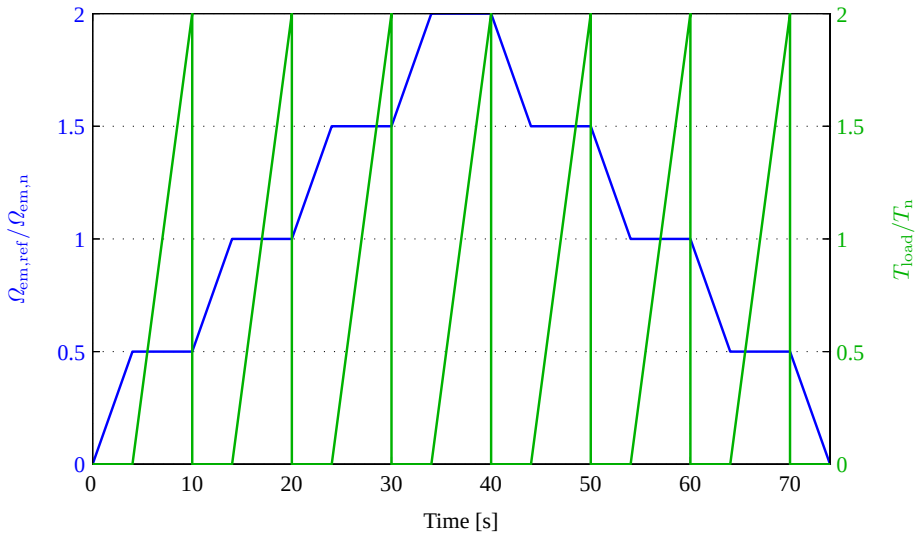

Fig. 2.15: Reference value for $\Omega_{\mathrm{em,ref}}$ normalized by the rated angular velocity of the motor and the torque T_{load} normalized by the rated torque of the electrical machine.

Table 2.2: Efficiencies given by the dynamic and quasi-static models.

	Size	η_{em}
Quasi-static	15 x 15	0.976
Quasi-static	25 x 25	0.976
Quasi-static	50 x 50	0.974
Quasi-static	75 x 75	0.973
Quasi-static	100 x 100	0.970
Quasi-static	150 x 150	0.970
Dynamic	-	0.962

The dynamic model gives 0.962 for the energy efficiency of the machine while the quasi-static model gives varying outputs between 0.970 and 0.976 depending on the accuracy of the efficiency map. Figure 2.16 describes the efficiency differences in the speed and torque ranges of 0–1 and the points in which the efficiency has been calculated. It can be seen that a small number of calculation points exaggerates the efficiency.

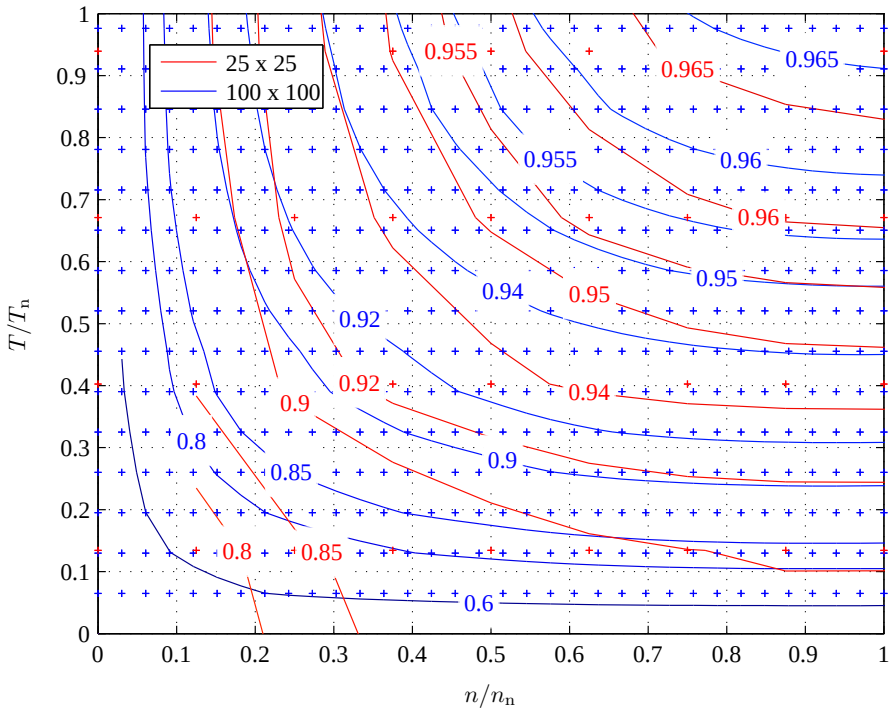

Fig. 2.16: Efficiency differences when the number of static model calculation points is 25 x 25 or 100 x 100.

When the number of calculation points is 100 x 100 or more, the difference between these approaches is 0.8 per cent units. This difference is due, for instance, to the fact that neither the flux linkage nor current can be changed abruptly in the dynamic model $\left(\psi_\mathrm{s} = \int u_\mathrm{s} \mathrm{d}t\right)$. In the quasi-static model instead, there are no such limitations. The accuracy of the quasi-static model is obviously accurate enough for modelling of a hybrid system.

2.1.2 Induction machine

Dynamic model

Similarly as the PMSM, an induction machine has been modelled applying the dynamic space vector theory in a rotor-flux-oriented d-q coordinate system complemented by the iron loss model. Figure 2.17 illustrates the d-q equivalent circuits with iron loss resistances [64].

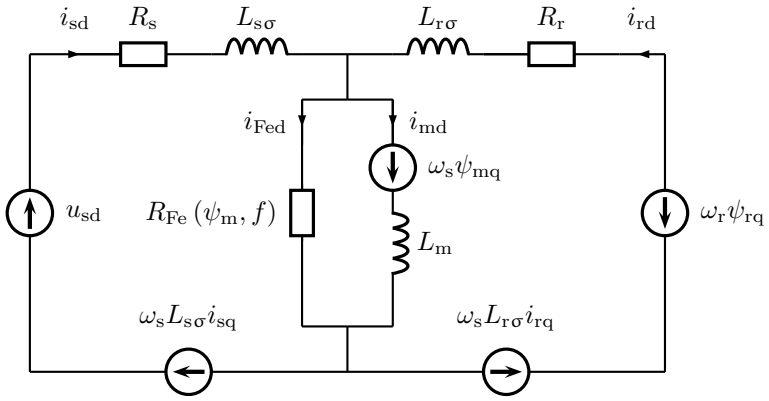

(a) Direct-axis model

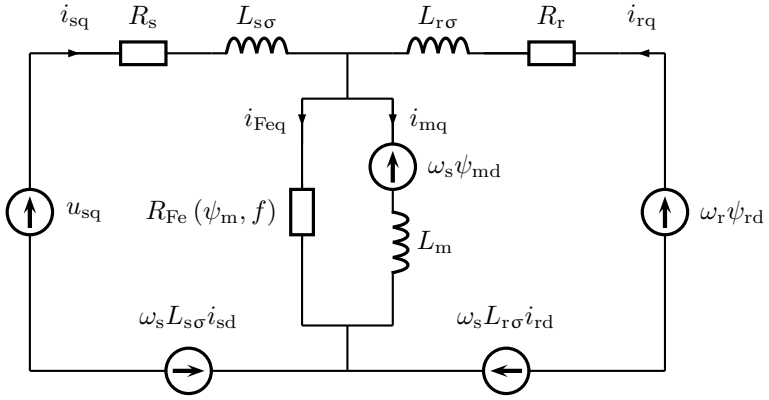

(b) Quadrature-axis model

Fig. 2.17: D-and q-axis models of the IM [65].

In the rotor co-ordinate system the IM voltages can be described by the following equations

$$u_{\mathrm{sd}} = R_{\mathrm{s}} i_{\mathrm{sd}} + \frac{\mathrm{d}\psi_{\mathrm{sd}}}{\mathrm{d}t} - \omega_{\mathrm{s}} \psi_{\mathrm{sq}} \tag{2.21}$$

$$u_{\mathrm{sq}} = R_{\mathrm{s}} i_{\mathrm{sq}} + \frac{\mathrm{d}\psi_{\mathrm{sq}}}{\mathrm{d}t} + \omega_{\mathrm{s}} \psi_{\mathrm{sd}} \tag{2.22}$$

$$u_{\mathrm{rd}} = R_{\mathrm{r}} i_{\mathrm{rd}} + \frac{\mathrm{d}\psi_{\mathrm{rd}}}{\mathrm{d}t} - (\omega_{\mathrm{s}} - \omega_{\mathrm{r}}) \psi_{\mathrm{rq}} = 0 \tag{2.23}$$

$$u_{\mathrm{rq}} = R_{\mathrm{r}} i_{\mathrm{rq}} + \frac{\mathrm{d}\psi_{\mathrm{rq}}}{\mathrm{d}t} + (\omega_{\mathrm{s}} - \omega_{\mathrm{r}}) \psi_{\mathrm{rd}} = 0 \tag{2.24}$$

The stator, rotor and air gap flux linkages are

$$\psi_{\mathrm{sd}} = L_{\mathrm{s}} i_{\mathrm{sd}} + L_{\mathrm{m}} i_{\mathrm{rd}} - L_{\mathrm{m}} i_{\mathrm{Fed}} \tag{2.25}$$

$$\psi_{\mathrm{sq}} = L_{\mathrm{s}} i_{\mathrm{sq}} + L_{\mathrm{m}} i_{\mathrm{rq}} - L_{\mathrm{m}} i_{\mathrm{Feq}} \tag{2.26}$$

$$\psi_{\mathrm{rd}} = L_{\mathrm{r}} i_{\mathrm{rd}} + L_{\mathrm{m}} i_{\mathrm{sd}} - L_{\mathrm{m}} i_{\mathrm{Fed}} \tag{2.27}$$

$$\psi_{\mathrm{rq}} = L_{\mathrm{r}} i_{\mathrm{rq}} + L_{\mathrm{m}} i_{\mathrm{sq}} - L_{\mathrm{m}} i_{\mathrm{Feq}} \tag{2.28}$$

$$\psi_{\mathrm{md}} = L_{\mathrm{m}} \left(i_{\mathrm{sd}} + i_{\mathrm{rd}} - i_{\mathrm{Fed}} \right) \tag{2.29}$$

$$\psi_{\mathrm{mq}} = L_{\mathrm{m}} \left(i_{\mathrm{sq}} + i_{\mathrm{rq}} - i_{\mathrm{Feq}} \right), \tag{2.30}$$

where $L_{\mathrm{s}} = L_{\mathrm{s}\sigma} + L_{\mathrm{m}}$ and $L_{\mathrm{r}} = L_{\mathrm{r}\sigma} + L_{\mathrm{m}}$.

With the flux linkage equations it is possible to solve for the stator, rotor and iron loss currents

$$i_{\mathrm{sd}} = \frac{\psi_{\mathrm{sd}} - \frac{L_{\mathrm{m}}}{L_{\mathrm{r}}} \psi_{\mathrm{rd}} - \left(\frac{L_{\mathrm{m}}^2}{L_{\mathrm{r}}} - L_{\mathrm{m}} \right) i_{\mathrm{Fed}}}{L_{\mathrm{s}} - \frac{L_{\mathrm{m}}^2}{L_{\mathrm{r}}}} \tag{2.31}$$

$$i_{\mathrm{sq}} = \frac{\psi_{\mathrm{sq}} - \frac{L_{\mathrm{m}}}{L_{\mathrm{r}}} \psi_{\mathrm{rq}} - \left(\frac{L_{\mathrm{m}}^2}{L_{\mathrm{r}}} - L_{\mathrm{m}} \right) i_{\mathrm{Feq}}}{L_{\mathrm{s}} - \frac{L_{\mathrm{m}}^2}{L_{\mathrm{r}}}} \tag{2.32}$$

$$i_{\mathrm{rd}} = \frac{\psi_{\mathrm{rd}} - \frac{L_{\mathrm{m}}}{L_{\mathrm{s}}}\psi_{\mathrm{sd}} - \left(\frac{L_{\mathrm{m}}^2}{L_{\mathrm{s}}} - L_{\mathrm{m}}\right) i_{\mathrm{Fed}}}{L_{\mathrm{r}} - \frac{L_{\mathrm{m}}^2}{L_{\mathrm{s}}}} \tag{2.33}$$

$$i_{\mathrm{rq}} = \frac{\psi_{\mathrm{rq}} - \frac{L_{\mathrm{m}}}{L_{\mathrm{s}}}\psi_{\mathrm{sq}} - \left(\frac{L_{\mathrm{m}}^2}{L_{\mathrm{s}}} - L_{\mathrm{m}}\right) i_{\mathrm{Feq}}}{L_{\mathrm{r}} - \frac{L_{\mathrm{m}}^2}{L_{\mathrm{s}}}} \tag{2.34}$$

$$i_{\mathrm{Fed}} = \frac{\frac{\psi_{\mathrm{md}}}{L_{\mathrm{m}}} - \frac{\psi_{\mathrm{sd}} - \frac{L_{\mathrm{m}}}{L_{\mathrm{s}}}\psi_{\mathrm{rd}}}{L_{\mathrm{s}} - \frac{L_{\mathrm{m}}^2}{L_{\mathrm{r}}}} - \frac{\psi_{\mathrm{rd}} - \frac{L_{\mathrm{m}}}{L_{\mathrm{r}}}\psi_{\mathrm{sd}}}{L_{\mathrm{r}} - \frac{L_{\mathrm{m}}^2}{L_{\mathrm{s}}}}}{2L_{\mathrm{m}} - L_{\mathrm{m}}^2\left(\frac{1}{L_{\mathrm{r}}} + \frac{1}{L_{\mathrm{s}}}\right) - 1} \tag{2.35}$$

$$i_{\mathrm{Feq}} = \frac{\frac{\psi_{\mathrm{mq}}}{L_{\mathrm{m}}} - \frac{\psi_{\mathrm{sq}} - \frac{L_{\mathrm{m}}}{L_{\mathrm{s}}}\psi_{\mathrm{rq}}}{L_{\mathrm{s}} - \frac{L_{\mathrm{m}}^2}{L_{\mathrm{r}}}} - \frac{\psi_{\mathrm{rq}} - \frac{L_{\mathrm{m}}}{L_{\mathrm{r}}}\psi_{\mathrm{sq}}}{L_{\mathrm{r}} - \frac{L_{\mathrm{m}}^2}{L_{\mathrm{s}}}}}{2L_{\mathrm{m}} - L_{\mathrm{m}}^2\left(\frac{1}{L_{\mathrm{r}}} + \frac{1}{L_{\mathrm{s}}}\right) - 1}. \tag{2.36}$$

$$\tag{2.37}$$

The IM torque is expressed as [64]

$$T_{\mathrm{e}} = -\frac{3}{2}p|\vec{\psi_{\mathrm{r}}} \times \vec{i_{\mathrm{r}}}| = \frac{3}{2}p\left(\psi_{\mathrm{rq}}i_{\mathrm{rd}} - \psi_{\mathrm{rd}}i_{\mathrm{rq}}\right) \tag{2.38}$$

and the rotational speed can be solved by using Eq. (2.16).

Quasi-static model

In the quasi-static model, we need a priori knowledge of the efficiency map and the maximum torque curve. Similarly as in the case of the PMSM, the efficiency map and the maximum torque curve can be given by the manufacturer, or they can be calculated based on machine parameters. In this case, the efficiency map and the maximum torque curve are calculated by using the machine parameters. Figure 2.18 depicts the vector diagram of an IM. The efficiency map and the maximum torque are calculated applying equations that are derived based on the vector diagram.

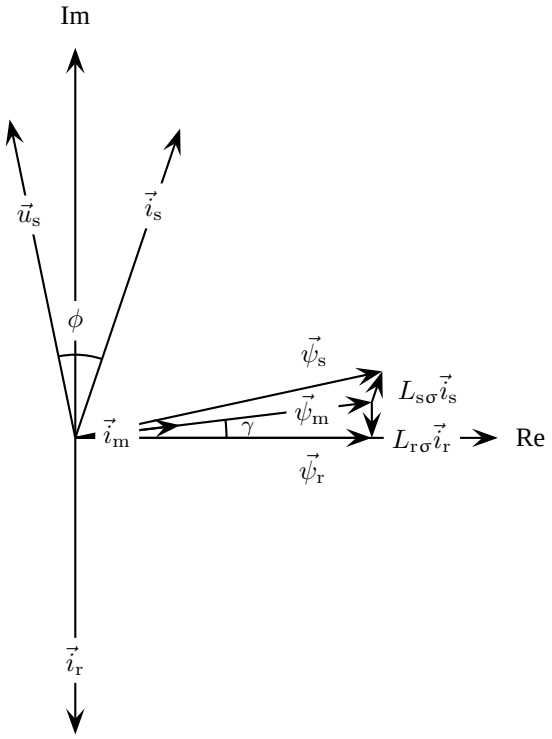

Fig. 2.18: Vector diagram of the IM in the rotor flux linkage co-ordinate system. The flux linkage vectors $\vec{\psi}_\mathrm{m}$, $\vec{\psi}_\mathrm{s}$ and $\vec{\psi}_\mathrm{r}$ are the magnetizing, stator and rotor flux linkage vectors, $\vec{i}_\mathrm{m}$, $\vec{i}_\mathrm{s}$ and $\vec{i}_\mathrm{r}$ the magnetizing, stator and rotor current vectors, respectively, $\vec{u}_\mathrm{s}$ is the stator voltage vector, ϕ is the phase angle and γ the magnetizing current angle.

In the steady state, the stator $\vec{u}_\mathrm{s}$ and rotor voltage vectors $\vec{u}_\mathrm{r}$ are [66]

$$\vec{u}_\mathrm{s} = R_\mathrm{s}\vec{i}_\mathrm{s} + \mathrm{j}\omega_\mathrm{s}\vec{\psi}_\mathrm{s} \tag{2.39}$$

$$\vec{u}_\mathrm{r} = R_\mathrm{r}\vec{i}_\mathrm{r} + \mathrm{j}\left(\omega_\mathrm{s} - \omega_\mathrm{r}\right)\vec{\psi}_\mathrm{r}, \tag{2.40}$$

where the stator $\vec{\psi}_\mathrm{s}$ and rotor flux linkage vectors $\vec{\psi}_\mathrm{r}$are

$$\vec{\psi}_\mathrm{s} = \vec{\psi}_\mathrm{m} + L_{\mathrm{s}\sigma} i_\mathrm{s} \tag{2.41}$$

$$\vec{\psi}_\mathrm{r} = \mathrm{Re}\left\{\vec{\psi}_\mathrm{m}\right\} \tag{2.42}$$

and the air gap flux linkage $\vec{\psi}_\mathrm{m} = L_\mathrm{m}\vec{i}_\mathrm{m} = L_\mathrm{m} i_\mathrm{m} \mathrm{e}^{\gamma \mathrm{j}}$.

The torque, voltages, currents and losses of the IM are calculated at different stator angular frequency ω_{s} and with different magnetizing current vectors $\vec{i}_{\mathrm{m}}$, by changing the absolute value of i_{m} and the angle γ, after which the maximum torque curve is determined and the efficiency maps calculated with the desired voltage. The saturation of L_{m} can be taken into account if L_{m} is defined as a function of magnetizing current for instance in the way suggested in [67]. However, it must be remembered that L_{m} also depends on the machine torque [68], [69]. This phenomenon and possible saturation of the leakage inductances are neglected in this case [70]. Figure 2.19 describes the flow chart of the calculation process.

Similarly as above with the PMSM, three-dimensional tables are built, by which it is possible to determine the maximum torque curve and plot the efficiency map with the desired boundary conditions.

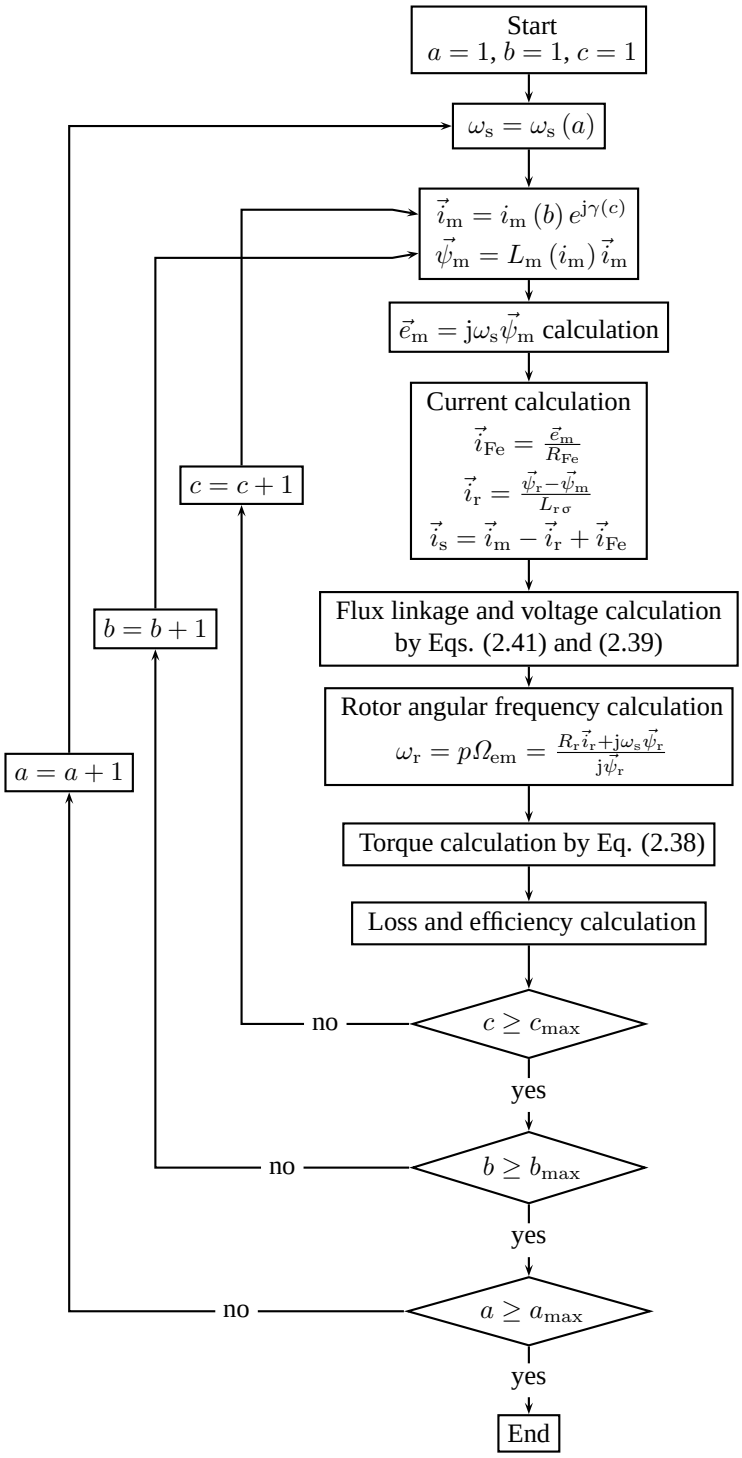

Fig. 2.19: Flow chart of the calculation process to define the induction machine efficiency.

Verification of the IM machine efficiency

With the method introduced above, the efficiency of the four-pole 37 kW IM is defined and the results are verified in the laboratory. The parameters of the IM are presented in Table 2.3.

Table 2.3: 37 kW induction motor parameters needed for the efficiency calculation [71].

Nominal power	P_{n}	37 kW
Nominal voltage	U_{n}	400 V
Nominal current	I_{n}	69 A
Nominal frequency	f_{n}	50 Hz
Number of pole pairs	p	2
Nominal speed	n_{n}	1480 rpm
Stator resistance	R_{s}	0.0629 Ω
Rotor resistance	R_{r}	0.0439 Ω
Stator leakage inductance	$L_{\mathrm{s}\sigma}$	0.483 mH
Rotor leakage inductance	$L_{\mathrm{r}\sigma}$	1.003 mH
Friction loss coefficient	k_{f}	149 W
Windage loss coefficient	k_{w}	189 W

The saturation of the magnetizing inductance is taken into account by measuring the magnetizing inductance as a function of magnetizing current. The magnetizing inductance is measured by the method presented in [67]. Figure 2.20 shows the measured magnetizing inductance values as a function of peak magnetizing current.

The measured magnetizing inductance decreases when the magnetizing current is smaller than 21 A. At low currents the measured magnetizing inductance values are smaller because of the form of the virgin BH curve and the hysteresis of the magnetic circuit material. The BH curve of the lamination material is not linear at low values of the magnetic field strength (Fig. 2.21), and the inductance is directly proportional to the permeability. The same behaviour of L_{m} was reported also in [67], [69], [72] and [73]. This decrease in L_{m} can cause demagnetization of the ferromagnetic core [73].

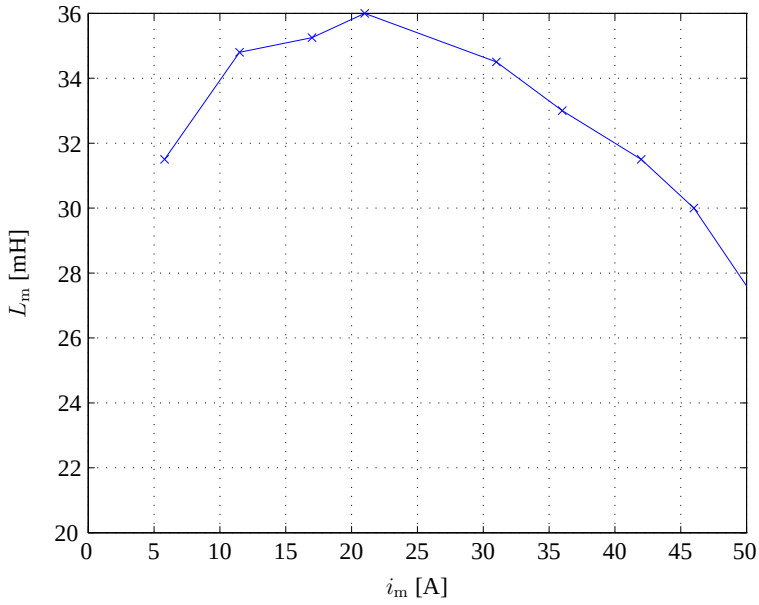

Fig. 2.20: Saturation of the magnetization inductance of an induction machine as a function of peak magnetizing current.

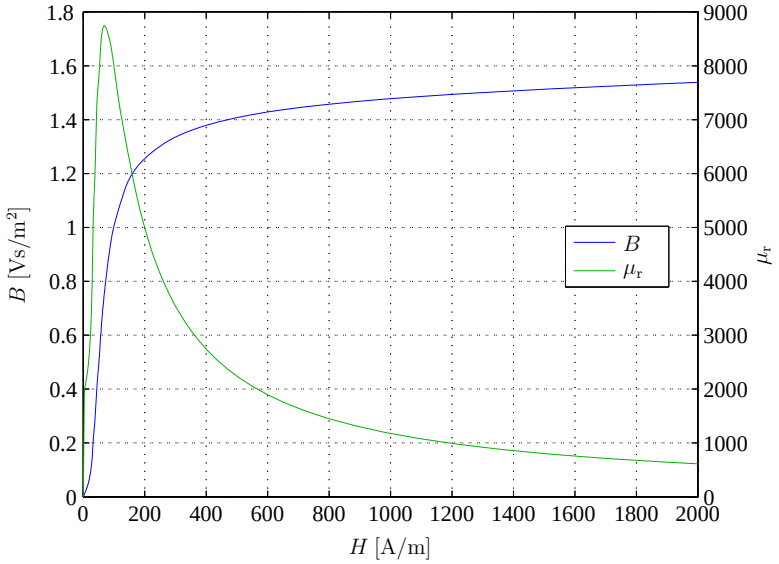

Fig. 2.21: Example of the BH curve and the relative permeability.

The calculated and measured efficiencies of the 37 kW induction machine with a constant flux

reference are compared. In the efficiency calculation, copper, iron, mechanical and additional losses are taken into account.

The iron loss resistance is estimated based on FEM simulations and measurements on the induction machine [71]. Figure 2.22 illustrates the estimated iron loss resistance as a function of frequency and air gap flux linkage.

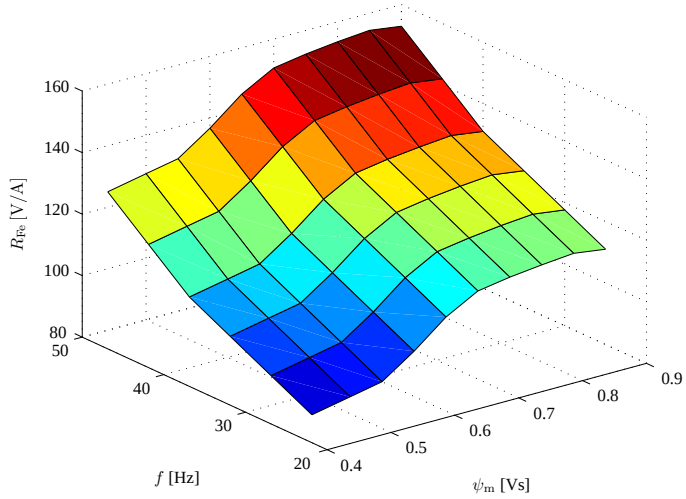

Fig. 2.22: Iron loss resistance used in the analysis of the induction machine. The resistance is a function of frequency and air gap flux linkage.

Additional losses P_{add} are proportional to the square of the RMS stator current I and to the power of $3/2$ of the frequency [74]. The additional losses are calculated by

$$P_{\mathrm{add}} = P_{\mathrm{add,n}} \left(\frac{I}{I_{\mathrm{n}}} \right)^2 \left(\frac{f}{f_{\mathrm{n}}} \right)^{\frac{3}{2}}, \tag{2.43}$$

where $P_{\mathrm{add,n}}$ are the measured additional losses in the nominal point, I_{n} is the stator RMS current in the nominal point and f_{n} is the nominal frequency.

Table 2.4 presents the measured and calculated efficiencies at different torques and rotational speeds. There are slight differences between the measured and calculated efficiency values.

Table 2.4: Calculated and measured efficiencies at different torques and rotational speeds with a constant flux reference. The measured efficiency values are given in parentheses.

$\frac{T}{T_\mathrm{n}} / \frac{n}{n_\mathrm{n}}$	0.25	0.5	0.75	1	1.5	2
1.5	-	88 (87)	91 (91)	-	-	-
1	85 (84)	90 (90)	92 (92)	93 (93)	-	-
0.75	86 (86)	90 (90)	92 (92)	93 (93)	92 (89)	-
0.5	87 (86)	90 (90)	91 (92)	92 (93)	92 (91)	-
0.25	85 (84)	87 (87)	87 (88)	88 (90)	89 (90)	87 (87)

The calculated efficiencies are equal to or higher than the measured efficiencies in almost all measured operating points except for three points at low torques. The differences between the calculated and measured efficiencies are due to the inaccuracy of the saturation and iron loss model. The saturation of the magnetizing inductance is also taken into account in a simple way. The magnetizing inductance also varies as a function of load [68]. The temperature effects of the resistance also have an impact on the efficiency, which, however, is not taken into account. Figure 2.23 presents the efficiency map of the IM with a constat flux reference without any *IR* compensation.

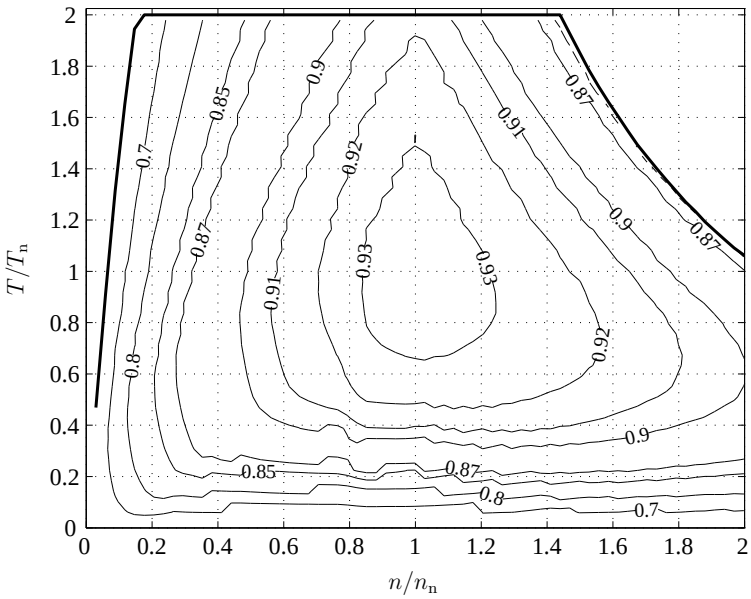

Fig. 2.23: Efficiency map of the IM with a constant flux reference without any IR *compensation.*

2.1.3 Frequency converter

In hybrid mobile machines, an electric machine is always controlled by a frequency converter, and the efficiency of the electric drive depends both on the efficiency of the motor and the converter and their interactions. This section studies the principles of converter efficiency calculation.

The simple two-level frequency converter comprises six IGBTs (insulated-gate bipolar transistors) and free-wheeling diodes connected anti-parallel to them.

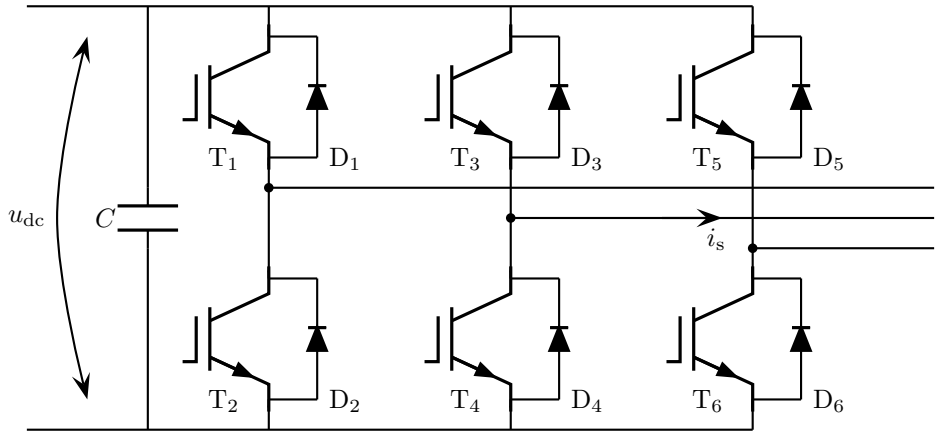

Fig. 2.24: Main circuit of the two-level three-phase frequency converter.

The inverter IGBT module losses are produced by the switching P_{sw} and conduction losses P_{cond} of the IGBTs and the diodes. These can be calculated based on the module parameters. The average conduction losses of a diode are [75]

$$P_{\mathrm{cond,D}} = \frac{1}{2} i_{\mathrm{s}} U_{\mathrm{D}} \left(\frac{1}{\pi} + \frac{M}{4} \cos\phi \right) + i_{\mathrm{s}}^2 R_{\mathrm{D}} \left(\frac{1}{8} + \frac{M}{3\pi} \cos\phi \right) \tag{2.44}$$

and the IGBT conduction losses [75]

$$P_{\mathrm{cond,IGBT}} = \frac{1}{2} i_{\mathrm{s}} U_{\mathrm{CE0}} \left(\frac{1}{\pi} - \frac{M}{4} \cos\phi \right) + i_{\mathrm{s}}^2 R_{\mathrm{CE}} \left(\frac{1}{8} - \frac{M}{3\pi} \cos\phi \right), \tag{2.45}$$

where i_{s} is the peak value of the phase current, U_{D} the threshold voltage of the diode, R_{D} the on-state resistance of the diode, U_{CE0} the threshold voltage of the IGBT, R_{CE} the on-state resistance of the IGBT, M the modulation index and $\cos\phi$ the power factor. The equations show that the losses depend on the current, and through the modulation index $M = \frac{u_{\mathrm{s}}}{2u_{\mathrm{dc}}}$, on the motor voltage. u_{dc} is the DC link voltage. These equations ignore the effect of the third

harmonic injection. The effect of this is, however, so small that the accuracy of the equations suffices for the purpose [75]. Both in the diodes and the transistors there are also switching losses. The switching losses of a diode are

$$P_{\mathrm{sw,D}} = \frac{1}{\pi} f_{\mathrm{sw}} E_{\mathrm{rr}} \left(i_{\mathrm{s}} \right) \tag{2.46}$$

and the IGBT switching losses

$$P_{\mathrm{sw,IGBT}} = \frac{1}{\pi} f_{\mathrm{sw}} \left(E_{\mathrm{on}} \left(i_{\mathrm{s}} \right) + E_{\mathrm{off}} \left(i_{\mathrm{s}} \right) \right), \tag{2.47}$$

where f_{sw} is the switching frequency, E_{on} is the turn-on energy depending on the current and E_{off} is the turn-off energy again depending on the current [76]. The switching losses are directly proportional to the switching frequency. The current also affects the switching losses as the turn-on and -off energies depend on that. In a three-phase converter there are six transistors and six diodes, and therefore, the total switching losses are found by multiplying by six. In addition to the IGBT module losses there are no-load losses covering for instance the converter stand-by losses $P_{\mathrm{inv},0}$

$$P_{\mathrm{inv,loss}} = 6 \left(P_{\mathrm{cond,D}} + P_{\mathrm{cond,IGBT}} + P_{\mathrm{sw,D}} + P_{\mathrm{sw,IGBT}} \right) + P_{\mathrm{inv},0}. \tag{2.48}$$

The converter efficiency can be defined when the input power P_{em} of the motor is known. During motoring the converter efficiency is

$$\eta_{\mathrm{inv}} = \frac{P_{\mathrm{em}}}{P_{\mathrm{em}} + P_{\mathrm{inv,loss}}} = \frac{\frac{3}{2} u_{\mathrm{s}} i_{\mathrm{s}} \cos\phi}{\frac{3}{2} u_{\mathrm{s}} i_{\mathrm{s}} \cos\phi + P_{\mathrm{inv,loss}}}. \tag{2.49}$$

In generating mode, the power supplied by the motor to the converter is known, and the efficiency is correspondingly

$$\eta_{\mathrm{inv}} = \frac{P_{\mathrm{em}} - P_{\mathrm{inv,loss}}}{P_{\mathrm{em}}} = \frac{\frac{3}{2} u_{\mathrm{s}} i_{\mathrm{s}} \cos\phi - P_{\mathrm{inv,loss}}}{\frac{3}{2} u_{\mathrm{s}} i_{\mathrm{s}} \cos\phi}. \tag{2.50}$$

The converter efficiency can be defined when the stator voltage, current and power factor are known in different operating points of the torque–speed plane. Hence, the converter efficiency map is dependent on the electric machine driven, and determined by applying the knowledge related to the machine efficiency map. The efficiency map given here is calculated for the drive using the PMSM studied above in Section 2.1.1. The voltage, current and power factor values used in the calculation are given in Fig. 2.11. The converter IGBT module parameters are given in Table 2.5.

Table 2.5: SKM600GA12E4 IGBT module parameters [77].

Nominal voltage	U_n	1200 V
Nominal RMS current	I_n	600 A
Switching frequency	f_sw	4 kHz
Threshold voltage of the diode	U_D	2.07 V
On-state resistance of the diode	R_D	1.9 mΩ
Threshold voltage of the IGBT	U_CE0	0.7 V
On-state resistance of diode of the IGBT	R_CE	2.5 mΩ
Diode turn-off energy	$E_\mathrm{rr}\,(I_\mathrm{rated})$	38 mJ
IGBT turn-on energy	$E_\mathrm{on}\,(I_\mathrm{rated})$	74 mJ
IGBT turn-off energy	$E_\mathrm{off}\,(I_\mathrm{rated})$	84 mJ

Figure 2.25 presents the inverter efficiency in the torque–rotational speed plane.

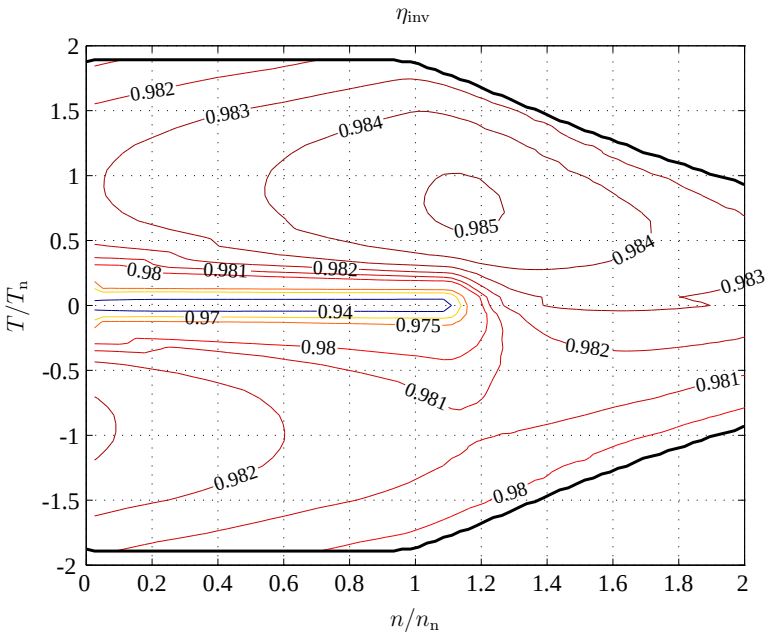

Fig. 2.25: Efficiency map of the inverter supplying the PMSM with optimum voltage.

For the converter in question, the current capability of the IGBT module limits the drive torque to $2T_\mathrm{n}$. The converter efficiency varies in the range of 0.94–0.985 depending on the operating point.

2.2 Energy storage

Supercapacitors, batteries or combinations of these can be used as the electric energy storage in hybrid drives. The specifications for the energy storage, such as capacity, charging and discharging power, efficiency, energy or power density and volume, lifetime and price, depend on the application [78]. The capacity of the storage is defined based either on the energy or power needed in the application [79]. In mobile machines it is common that high instantaneous power levels are needed. When a battery is used, it often has to be dimensioned based on the allowable instantaneous power level. In such a case, many of the present-day battery types must be usually largely overdimensioned by the energy storage capability. In this study, an energy storage is connected directly to the DC link of the frequency converter. Consequently, the voltage of the energy storage has to be such that the direct connection to the DC link is possible. By connecting the energy storage directly to the DC link, the losses of the DC-DC converter can be avoided.

Table 2.6 lists different electric energy storage cell types and their prices. The values given in the table are for a single battery cell. When cells are assembled into modules, the charge and discharge currents are lower.

Table 2.6: Characteristics of battery cell technologies [80]–[85].

	NiMH	Lithium-ion (Saft)	Lithium-iron phosphate	Lithium-polymer	Lithium-titanate	Supercapacitor
Nominal voltage $[\mathrm{V}]$	1.2	3.6	3.3	3.7	2.3	2.5–2.7
Specific power $[\mathrm{kW/kg}]$ cont. (max)	0.2–1.2	0.2–16 (2–30)	0.2–5 (2–7)	0.1–3	0.76–0.9	4–10
Specific energy $[\mathrm{Wh/kg}]$	55–80	58–190	66–160	110–180	52–75	5–10
Cycle life	>1000	>5000	>1000	>800	>10 000	$>10^6$
Max. discharge rate, cont. (pulse)	5C	4–120C (7–270C) 2 s	0.9–175C (2.3–260C) 2 s	1–5C (2–20C) 10 s	6C (10C) 10 s	-
Max. charge rate	1C	C/7–C	C/7	1–3C	6–11C	-
Temperature $[^\circ\mathrm{C}]$	–10–65	–60–60	–30–55	–20–60	–40–55	–40–65
Price $[€/\mathrm{kWh}]$	900–1000	800–1200	1000–1500	1000–1500	1500–2000	40 000

Figure 2.26 illustrates different 700 V energy storage properties; maximum power ($P_{\mathrm{es,max}}$) and energy capacity (E_{es}), when different techniques have been used in the assembly of the storage. The energy storages illustrated in Fig. 2.26 have been built by connecting commercial battery (Kokam, Saft, Altairnano) or supercapacitor (Maxwell, Nesscap) modules in series so that the rated voltage of the storage can reach 700 V. The maximum charging or discharging current of the resulting battery unit is assumed as high as the maximum current of the building block module.

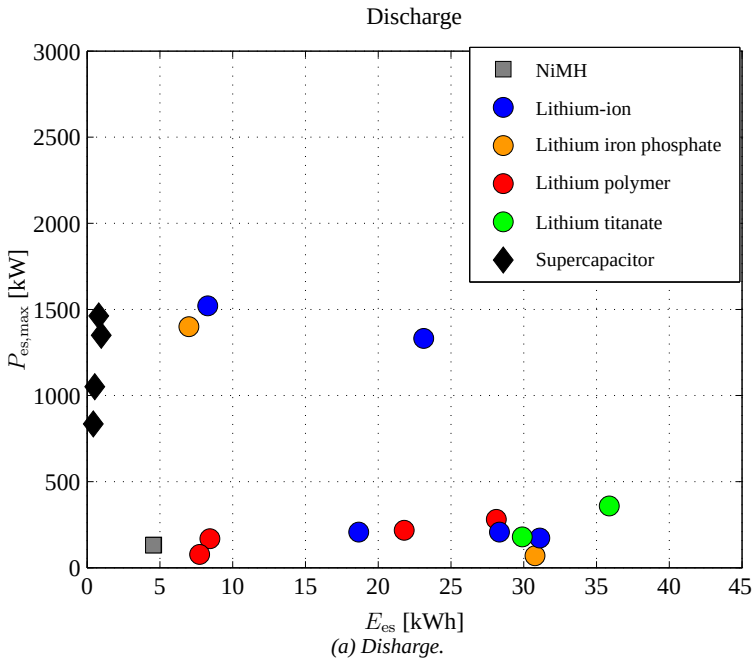

(a) Disharge.

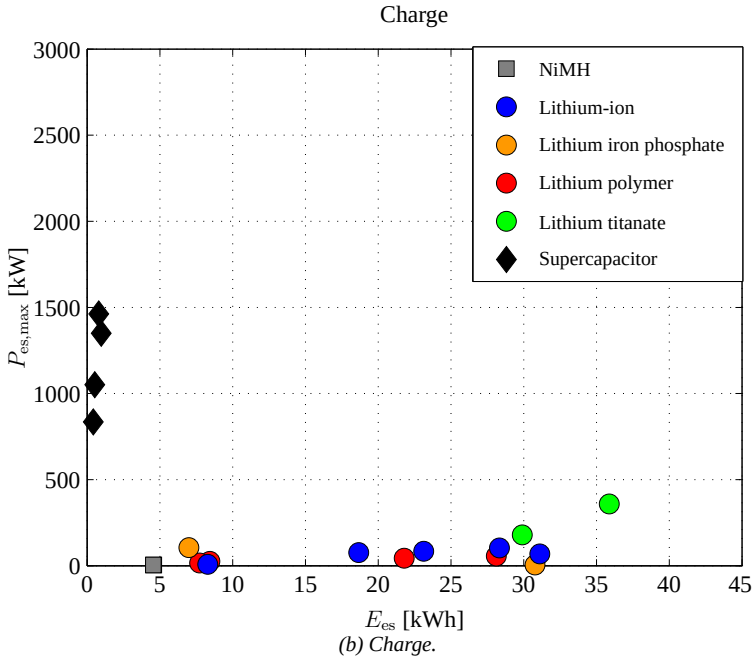

(b) Charge.

Fig. 2.26: $P_{\mathrm{es,max}}$ and E_{es} properties of 700 V energy storages based on different technologies.

Based on the information found in Table 2.6 and Fig. 2.26, it is obvious that it is difficult to

use other than lithium titanate (LiTi) batteries or supercapacitors in mobile working machines where the energy recovery peaks are often high. Therefore, also the charging power of the energy storage must be high enough.

Further, a high cycle life of a practical energy storage is important. This feature again suggests using LiTi batteries or supercapacitors. The cycle life of batteries is typically lower than the cycle life of supercapacitors, but when the depth of discharge (DoD) in LiTi batteries is low enough, the cycle life is increased by several decades from the value given by Table 2.6. Further, the efficiencies of LiTi batteries and supercapacitors are high; the efficiency of the LiTi battery is 95–97% and the efficiency of the supercapacitor is claimed to be 95–98% [86], [87].

Figure 2.27 shows the cycle life of a LiTi battery as a function of DoD for two temperatures.

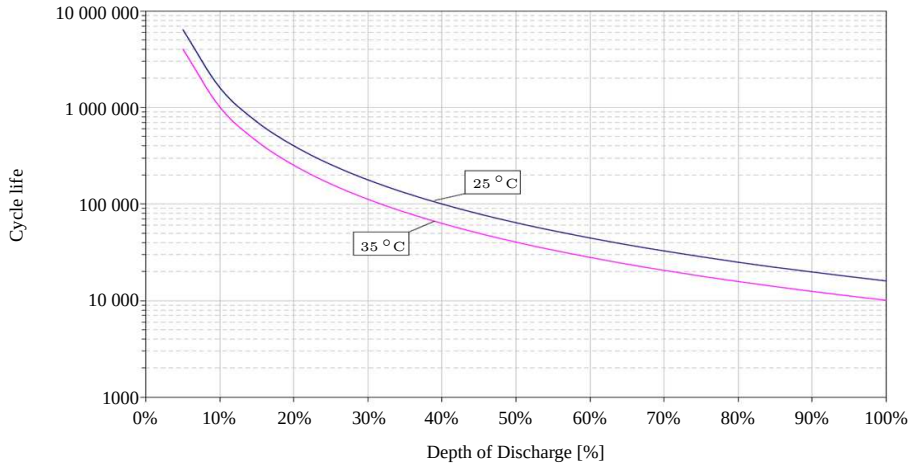

Fig. 2.27: Cycle life of a lithium titanate battery with different depths of discharge [88].

Figure 2.27 shows that the DoD has a significant influence on the cycle life of a battery. If a LiTi battery is operated at a DoD of less than 10% in the temperature of $35\,^{\circ}\mathrm{C}$, the battery will last about a million cycles. With the 30% depth of discharge, the cycle life decreases to one-tenth of the lifetime provided by the 10% value. Therefore, the effect of the DoD on the cycle life of a battery has to be taken into consideration when dimensioning an energy storage.

Irrespective of the type of the storage (battery or supercapacitor) it can be represented by the symbol illustrated in Fig. 2.28. Current is the input variable while voltage is the output of the storage.

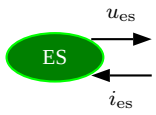

Fig. 2.28: EMR presentation of an energy storage.

2.2.1 Battery

A battery can be modelled either statically or dynamically. A static model is formed by using manufacturer-given charging and discharging curves and some battery parameters [89]. A simple dynamic model can be based on an equivalent circuit having different resistors and capacitors and that can be determined based on measurements and the manufacturer-given curves [90].

Below, a static model of a battery is studied, as the designer does not necessarily have an option of measuring the battery properties during the design phase. The static model studied here includes the following manufacturer-given parameters, $R_{\mathrm{charge}}\left(SOC\right)$, $R_{\mathrm{discharge}}\left(SOC\right)$ and $u_{\mathrm{OC,cell}}\left(SOC\right)$. Figure 2.29 depicts an equivalent circuit of a single battery cell.

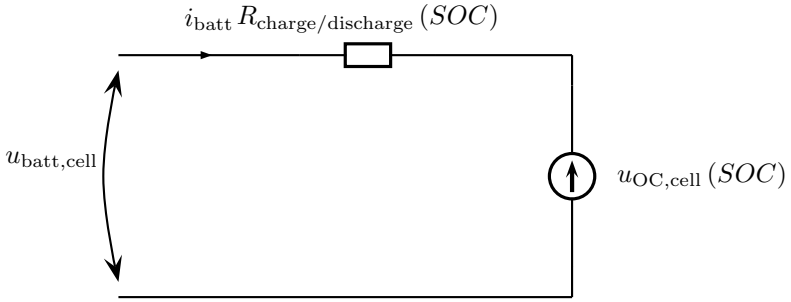

Fig. 2.29: Equivalent circuit of a battery cell.

The state of charge (SoC) as a function of time is

$$SOC\left(t\right) = \frac{\int i_{\mathrm{batt}} \mathrm{d}t}{Q_{\mathrm{max}}} + SOC_{\mathrm{init}}, \tag{2.51}$$

where i_{batt} is the current, Q_{max} the maximum value of charge and SOC_{init} the initial value of the SoC. The open-circuit voltage of the battery $u_{\mathrm{OC,sys}}$ is dependent on the SoC

$$u_{\mathrm{OC,sys}}\left(SOC\right) = N_{\mathrm{s}} u_{\mathrm{OC,cell}}\left(SOC\right), \tag{2.52}$$

where $u_{\mathrm{OC,cell}}\left(SOC\right)$ is the SoC-dependent open-circuit voltage and N_{s} the number of series-connected cells. The terminal voltage of the battery $u_{\mathrm{batt,sys}}$ depends both on the SoC and current i_{batt}

$$u_{\mathrm{batt,sys}}\left(SOC, i_{\mathrm{batt}}\right) = N_{\mathrm{s}} u_{\mathrm{OC,cell}}\left(SOC\right) + \frac{N_{\mathrm{s}}}{N_{\mathrm{p}}} R_{\mathrm{charge/discharge}}\left(SOC\right) i_{\mathrm{batt}}, \quad (2.53)$$

where N_{p} is the number of parallel cells and $R_{\mathrm{charge/discharge}}\left(SOC\right)$ is the resistance depending on the SoC and the direction of the current. The losses of the battery $P_{\mathrm{batt,loss}}$ are

$$P_{\mathrm{batt,loss}} = R_{\mathrm{charge/discharge}}\left(SOC\right) i_{\mathrm{batt}}^2 \quad (2.54)$$

and the instantaneous efficiency

$$\eta_{\mathrm{batt}} = \begin{cases} \frac{u_{\mathrm{OC,sys}}(SOC) i_{\mathrm{batt}}}{\left(u_{\mathrm{OC,sys}}(SOC) + \frac{N_{\mathrm{s}}}{N_{\mathrm{p}}} R_{\mathrm{charge}}(SOC) i_{\mathrm{batt}}\right) i_{\mathrm{batt}}} & \text{if } i_{\mathrm{batt}} > 0 \\ \frac{\left(u_{\mathrm{OC,sys}}(SOC) - \frac{N_{\mathrm{s}}}{N_{\mathrm{p}}} R_{\mathrm{discharge}}(SOC) i_{\mathrm{batt}}\right) i_{\mathrm{batt}}}{u_{\mathrm{OC,sys}}(SOC) i_{\mathrm{batt}}} & \text{if } i_{\mathrm{batt}} \leq 0 \end{cases}$$

Normally, the energy efficiency of a battery when operated in a certain cycle is of more interest.

The battery surface temperature

$$T_{\mathrm{core}} = T_{\mathrm{core,init}} + \int \frac{P_{\mathrm{batt,loss}} - \alpha A \left(T_{\mathrm{core}} - T_{\mathrm{amb}}\right)}{mC} \mathrm{d}t, \quad (2.55)$$

where T_{core} is the surface initial temperature, α the convection coefficience, A the total heat flow surface of the battery, m the mass, C the specific heat capacity and T_{amb} the ambient temperature.

2.2.2 Supercapacitor

A supercapacitor can be modelled by using a classical first-order model, a ladder model [91], a three-branch model [92] (Fig. 2.30) or a frequency-, voltage- and temperature-dependent model [93]. The first-order model is the simplest equivalent presentation of a supercapacitor, and it uses constant parameters. The first-order model ignores the frequency, current and voltage dependencies of the parameters. The three-branch model allows improving the

dynamic accuracy of the first-order model with frequencies up to 1 Hz. The ladder model, however, is capable of modelling frequencies beyond 1 kHz. The frequency-, voltage- and temperature-dependent model obviously takes these dependencies into account.

The main problems in the ladder model, the three-branch model and the frequency-, voltage- and temperature-dependent model are related to acquiring the correct parameters. A manufacturer usually gives only the equivalent series resistance and capacitance. Therefore, in this case, a simple first-order model is used. Figure 2.30a shows the equivalent circuit of the first-order model. It consists of the capacitance C_{sc}, the series resistance $R_{\mathrm{ESR,sc}}$, the parallel resistance R_{p} and the series inductance L_{sc}. The series inductance L_{sc} is normally very small and the parallel resistance R_{p} very large, and therefore, they can be ignored in the modelling of a supercapacitor.

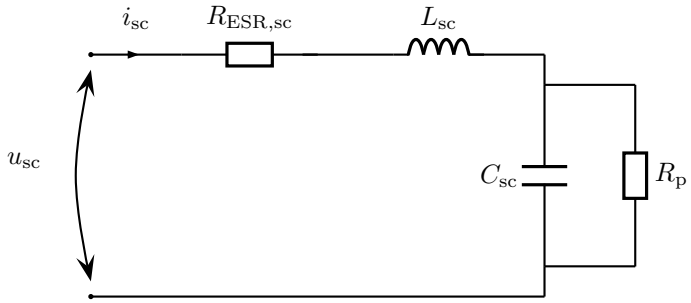

(a) First-order model.

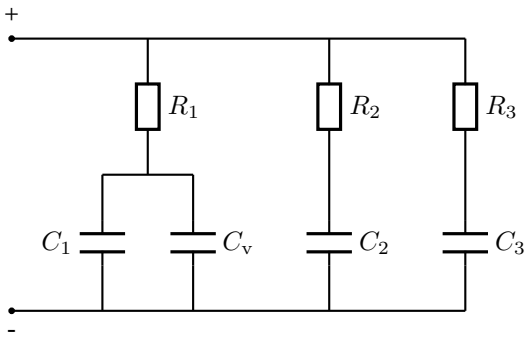

(b) Three branch model.

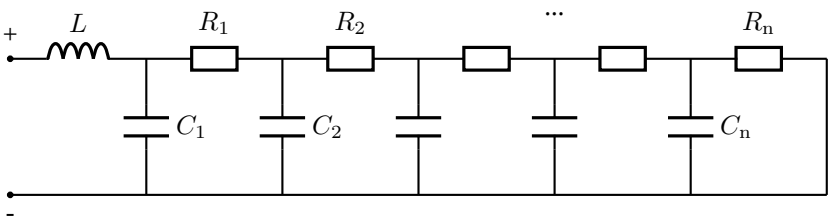

(c) Ladder model.

Fig. 2.30: Equivalent circuit of a supercapacitor [91], [92], [94].

The terminal voltage u_{sc} of a supercapacitor can be calculated by the current of the capacitor i_{sc}, the capacitance C_{sc} and the equivalent series resistance $R_{\mathrm{ESR,sc}}$ as

$$u_{\mathrm{sc}} = \frac{1}{C_{\mathrm{sc}}} \int i_{\mathrm{sc}} \mathrm{d}t - i_{\mathrm{sc}} R_{\mathrm{ESR,sc}}. \tag{2.56}$$

For a supercapacitor, the SoC can be defined either as a ratio of the instantaneous energy and the maximum energy or as a square of the ratio of the instantaneous and maximum voltages

$$SOC = \frac{E_{\mathrm{sc}}}{E_{\mathrm{sc,max}}} = \frac{u_{\mathrm{sc}}^2}{u_{\mathrm{sc,max}}^2}. \tag{2.57}$$

2.3 Diesel engine

In this case, the diesel engine is modelled very simply by a one time constant system and an efficiency map. The torque is limited to the maximum torque curve of the engine $T_{\mathrm{d,max}}$. Figure 2.31 illustrates the block diagram used for a diesel engine in this case. On the diesel engine shaft there are the torque given by the engine T_{d} and the load torque T_{load}, which, depending on the system, consists of the torque of the hydraulic system $T_{\mathrm{hyd,tot}}$, the torque converter T_{tc} and the electric machine torque T_{em} connected to the same shaft.

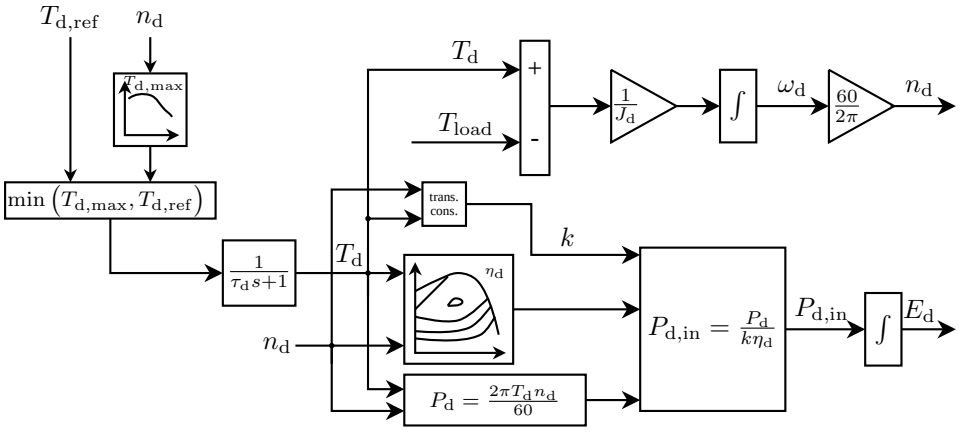

Fig. 2.31: Block diagram of the diesel engine model. τ_{d} is the diesel engine time constant, n_{d} the diesel engine rotational speed, and the factor k takes the transient fuel consumption into account.

The input energy to the diesel engine is calculated by the static efficiency map of the engine. Dynamic states, however, have a significant influence on the engine consumption [95]. In transients, the consumption increases for instance because of the lag in the turbocharger; in

transients, the turbocharger takes time to accelerate to the new operating point speed level and the air-fuel-ratio becomes non-favourable. In addition, the cylinder walls may get moist, which degrades the combustion [96]. During fast transients, the consumption can be even doubled compared with the static consumption [97].

Behaviour of this kind cannot only be modeled by the static efficiency map, and therefore, the method suggested by Lindgren and Hansson [97] is used. During transients, the diesel fuel consumption is calculated by using the static efficiency map and dividing the figure by the transient consumption factor k. Lindgren and Hansson introduced consumption curves that are dependent on changes in speed and torque. Figure 2.32 shows an example of a diesel engine static efficiency map and its maximum torque and power curves.

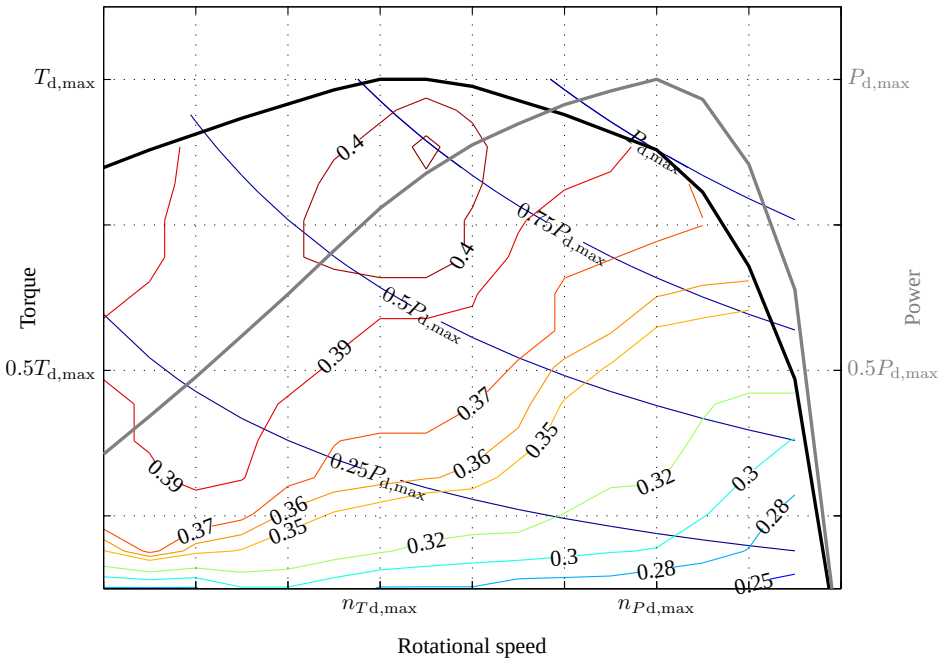

Fig. 2.32: Diesel engine static efficiency map with maximum torque and power curves.

The example map shows that the best efficiency point in static operation is over 0.40, and it is in this case reached at 0.88 $T_{\mathrm{d,max}}$. The power of the diesel engine in this point is about 0.75 $P_{\mathrm{d,max}}$. For example, the best efficiency is, in practice, always found at a speed close to the speed of the maximum torque point. This speed is usually low compared with the maximum speed of the engine. At such a low speed, the relative friction losses and the gas exchange losses remain at lowest.

2.4 Torque converter

A torque converter is needed in some parallel hybrid systems where the diesel motor is used to power all machine actions. Usually, such a machine must have an automatic gearbox with a torque converter. The torque converter makes the modelling of the energy efficiency of a working machine somewhat complicated. The torque converter can also be modelled either statically or dynamically. A dynamic model of a torque converter is given for instance in [98]. Once again, it is very difficult to find all the parameters needed to model a torque converter. The dynamic model describes the fluid flow in the converter, which makes it significantly more realistic compared with the static modelling. Figure 2.33 illustrates the input and output variables of a static model with the EMR presentation.

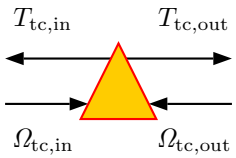

Fig. 2.33: Representation of a static torque converter model using the EMR.

The block diagram of a torque converter is presented in Fig. 2.34. The input torque (from the diesel engine) to the converter $T_{\mathrm{tc,in}}$ and the output $T_{\mathrm{tc,out}}$ (to the gearbox) can be determined when the input $\Omega_{\mathrm{tc,in}}$ and output angular velocities $\Omega_{\mathrm{tc,out}}$ of the converter are known and the torque ratio R_{T} and the capacity factor Kas functions of the relative angular velocity Ω_{rel} are known.

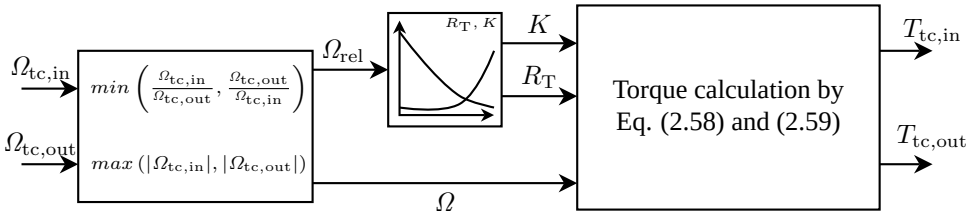

Fig. 2.34: Torque converter block diagram.

Figure 2.35 shows a possible torque ratio and capacity factor of a torque converter as a function of relative speed. The relative angular velocity $\Omega_{\mathrm{rel}} = \min\left(\frac{\Omega_{\mathrm{tc,in}}}{\Omega_{\mathrm{tc,out}}}, \frac{\Omega_{\mathrm{tc,out}}}{\Omega_{\mathrm{tc,in}}}\right)$ and the angular velocity $\Omega = \max\left(|\Omega_{\mathrm{tc,in}}|, |\Omega_{\mathrm{tc,out}}|\right)$ are used in torque calculation. The torque converter input and output torques can be defined as

$$T_{\mathrm{in}} = \begin{cases} \left(\frac{\Omega}{K}\right)^2, & \Omega_{\mathrm{tc,in}} > \Omega_{\mathrm{tc,out}} \\ -R_{\mathrm{T}}\left(\frac{\Omega}{K}\right)^2, & \Omega_{\mathrm{tc,in}} \leq \Omega_{\mathrm{tc,out}} \end{cases} \tag{2.58}$$

$$T_{\mathrm{out}} = \begin{cases} R_{\mathrm{T}}\left(\frac{\Omega}{K}\right)^2, & \Omega_{\mathrm{tc,in}} > \Omega_{\mathrm{tc,out}} \\ -\left(\frac{\Omega}{K}\right)^2, & \Omega_{\mathrm{tc,in}} \leq \Omega_{\mathrm{tc,out}}. \end{cases} \tag{2.59}$$

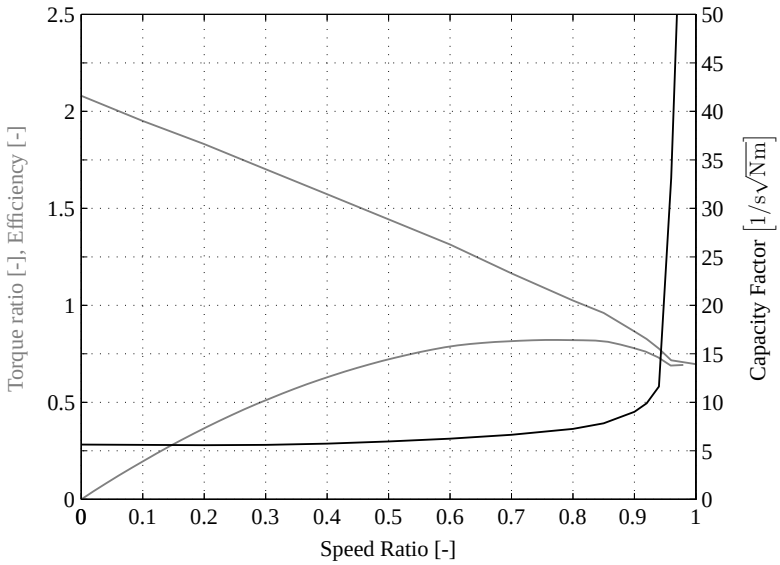

Fig. 2.35: Examples of the torque ratio R_{T}, the efficiency η_{tc} and the capacity factor K as functions of relative angular velocity Ω_{rel} [98], [99].

Figure 2.36 shows the efficiency of the torque converter as functions of $\Omega_{\mathrm{tc,in}}$ and $\Omega_{\mathrm{tc,out}}$ using the parameters of Fig. 2.35.

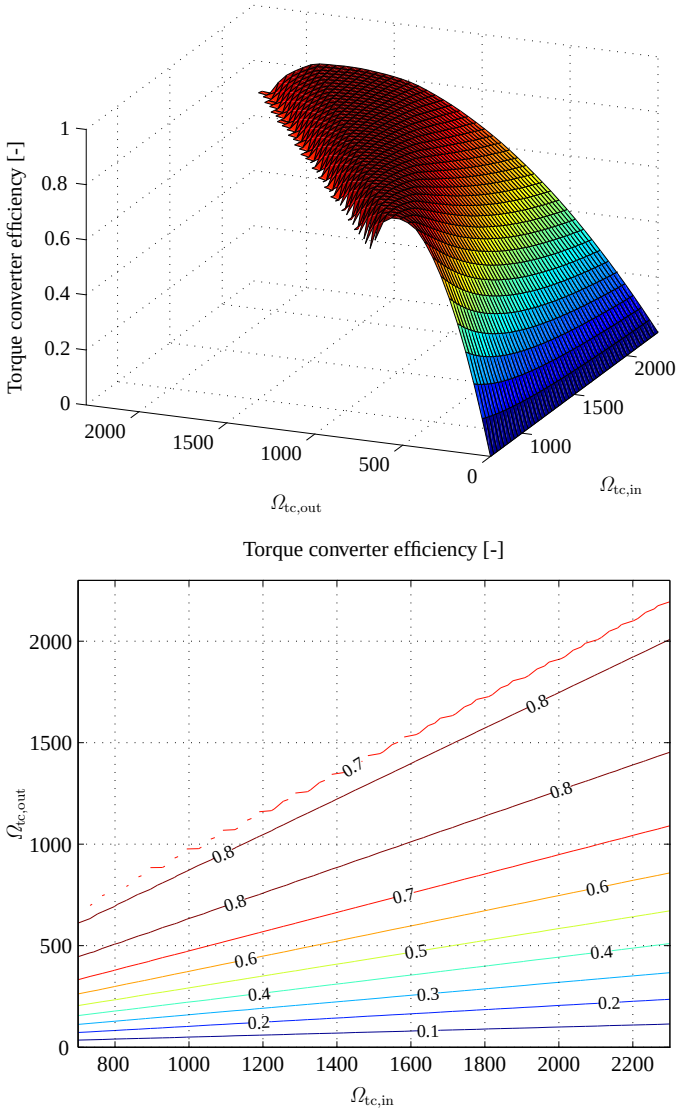

Fig. 2.36: Examples of the efficiency in the $\Omega_{\mathrm{tc,in}}$ $\Omega_{\mathrm{tc,out}}$ plane. Efficiency is determined in an area where $\Omega_{\mathrm{tc,out}} < \Omega_{\mathrm{tc,in}}$.

The efficiency is calculated in an area where $\Omega_{\mathrm{tc,out}} < \Omega_{\mathrm{tc,in}}$. The maximum efficiency of the torque converter 0.82 is reached at a relative angular velocity of about 0.78. The smaller the relative angular velocity Ω_{rel} is, the lower is the efficiency of the torque converters. The losses of the torque converter are emphasized especially at starts, where a high torque is needed at a low speed. The instantaneous losses of a torque converter can exceed 80% of the input power [100]. In our case example, the simulated torque converter losses consume 35% of all input energy to the traction system when using the example load. Beck [101] has measured similar losses in the case of a rubber-tyred loader.

2.5 Gear and transmission

The gearbox and final drive EMR is shown in Fig. 2.37, where T_{d} is the diesel engine torque, T_{trans} the gearbox torque, T_{diff} the final drive torque, Ω_{d} the diesel engine angular velocity, Ω_{trans} the gearbox angular velocity and Ω_{diff} the final drive angular velocity. T_{d} and Ω_{trans} are the inputs and T_{trans} and Ω_{d} are the outputs of the gearbox model. T_{trans} and Ω_{diff} are the inputs and T_{diff} and Ω_{trans} are the outputs of the final drive model.

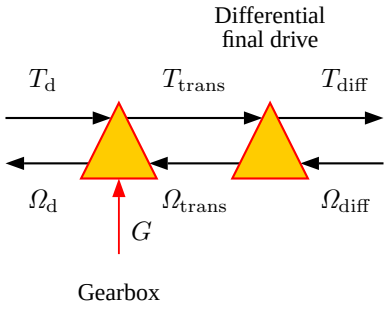

Fig. 2.37: Representation of a gearbox and differential final drive model using the EMR.

The gearbox and the final drive can be modelled by the block diagram of Fig. 2.38, where η_{trans} is the gearbox efficiency, η_{diff} is the final drive efficiency, $i_{\mathrm{trans}}(G)$ the gear ratio depending on the gear G used and i_{diff} is the fixed gear ratio of the final drive. The power c is dependent on the power flow direction, if the power is transmitted from the diesel to the tyres $(P \geq 0)$, $c = 1$, and if the power tries to flow in the opposite direction $(P < 0)$, $c = -1$.

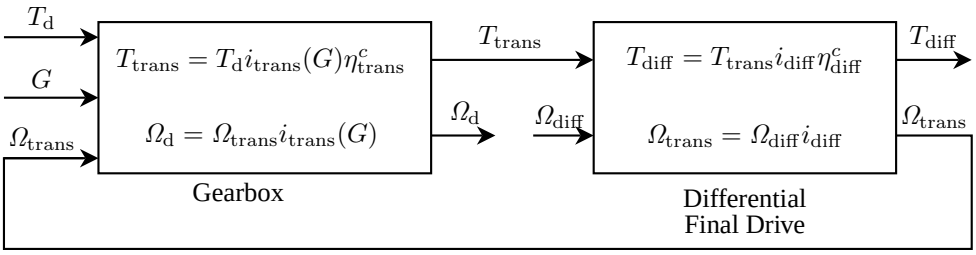

Fig. 2.38: Block diagrams of the gearbox and the final drive.

In the simulations we have used the gearbox efficiency of η_{trans} = 0.92 and the final drive efficiency of η_{diff} = 0.90. In the simulated work cycle, the gearbox losses were about 5% and the final drive losses about 7% of the energy fed into the traction drive. Beck [101] has obtained similar losses for the gearbox in the case of a rubber-tyred loader.

2.6 Friction forces

Figure 2.39 illustrates the tyre and frame model of the machine using the EMR. F_{eq} is the equivalent force of a tyre, F_{brake} is the brake force, F_{tot} the sum of the tyre and brake forces ($F_{\mathrm{tot}} = F_{\mathrm{eq}} + F_{\mathrm{brake}}$), F_{res} the friction forces affecting the machine and v_{veh} is the vehicle speed.

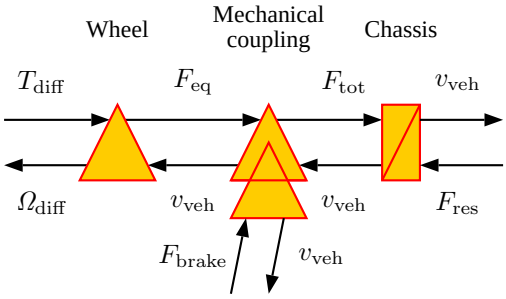

Fig. 2.39: Representation of the friction model using the EMR.

The tyre equivalent output force is $F_{\mathrm{eq}} = \frac{T_{\mathrm{diff}}}{r_{\mathrm{wheel}}}$, where r_{wheel} is the radius of the wheel. The speed of the vehicle v_{veh} can be solved with the forces F_{tot} and F_{res}

$$v_{\mathrm{veh}} = \int \frac{F_{\mathrm{tot}} - F_{\mathrm{res}}}{m_{\mathrm{veh}}} \mathrm{d}t \tag{2.60}$$

and with the speed, also the wheel angular velocity $\Omega_{\mathrm{diff}} = \frac{v_{\mathrm{veh}}}{r_{\mathrm{wheel}}}$ is found.

The friction forces F_{res} are mass and speed dependent. The forces taken into account are [102], [103]:

- air drag $F_{\mathrm{air}} = \frac{1}{2}\rho C_{\mathrm{d}} A_{\mathrm{f}} \left(v_{\mathrm{veh}} + v_{\mathrm{wind}}\right)^2$, where
  - ρ represents the air density,
  - C_{d} is the air drag coefficient,
  - A_{f} is the front cross-sectional area,
  - v_{veh} is the machine speed and
  - v_{wind} is the wind speed

- the inclination of the road causes a force $F_{\mathrm{slope}} = m_{\mathrm{veh}} g \sin\beta$, where
  - m_{veh} is the total mass of the vehicle,
  - g is the gravitational constant and
  - β is the road inclination angle
- rolling friction $F_{\mathrm{roll}} = k m_{\mathrm{veh}} g$, where
  - k is the rolling friction coefficient
- the force caused by the wheel moment of inertia $F_{\mathrm{wheel}} = \frac{\frac{1}{2} m_{\mathrm{wheel}} r_{\mathrm{wheel,eff}}^2 \alpha}{r_{\mathrm{wheel}}}$, where
  - m_{wheel} is the mass of the wheel
  - $r_{\mathrm{wheel,eff}}$ is the effective radius of the tyre and
  - α angular acceleration.

Typical values of the air drag coefficient C_{d} and the rolling friction coefficient k are presented in Table 2.7.

Table 2.7: Typical values of the air drag coefficient C_{d} and the rolling friction coefficient k [104]–[107].

	C_{d} [-]	k [-]
Light-duty vehicles	0.3–0.35	0.008–0.01
Heavy-duty vehicles	0.58–0.78	0.005–0.02

2.7 Working hydraulics

The working hydraulics is not modelled in this work, but the loads caused by a virtual machine are fed directly into the model as time-dependent load curves. At the Department of Intelligent Hydraulics and Automation at Tampere University of Technology, the power demand of the working hydraulics used in the case working machine has been modelled by a combined simulation model based on measurement results. The simulation model is a combination of the Amesim and Simulink simulation software. The power demand has been determined for the present working machine, in which the energy recovery or recycling from one actuator to another is not possible.

The power demand is also determined for the working hydraulics used in the hybrid systems; the hydraulics is implemented by pump-motor unit that enable energy recovery and reuse. In this doctoral thesis, the power curves determined for the hydraulics by the TUT IHA are used in the simulations. The power curves are converted into corresponding torque loads for the system. Figure 2.40 demonstrates the working hydraulics EMR.

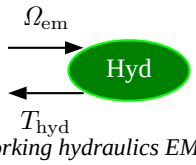

Fig. 2.40: Working hydraulics EMR.

Chapter 3

Simulation model of a hybrid working machine

Hybrid systems are illustrated graphically by using the EMR presentation. This chapter focuses on presenting the interconnections between the subcomponents of the hybrid system model introduced in the previous chapter. The described hybrid systems are the parallel, parallel-series and series hybrid system.

In a pure parallel hybrid system, both the traction and working hydraulics are driven by the parallel hybrid principle using the diesel genset, which is mechanically connected both to the hydraulic pumps and to the torque converter [108]. In a pure series hybrid system, all actions of the working machine are driven by electric motors, and there is no mechanical connection to the diesel, which is only used to rotate a generator to generate electricity for the machine [108]. In a parallel-series hybrid system, the working hydraulics is diesel genset driven and the traction is electric motor driven.

3.1 Parallel hybrid

In the parallel hybrid system, the traction is implemented by using a torque converter with a lock-up, a five-gear gearbox and a fixed final drive. The hydraulic pumps are fixed with the diesel genset on a common shaft. The main lifting movement of the working hydraulics is delivered by a pump-motor unit enabling energy recovery from the lowering. The hydraulics output is controlled by the swash-plate angle control of the pump-motor unit. Negative swash-plate angles provide an opportunity of regenerating while the rotational direction of the whole system remains the same. This is necessary in a parallel hybrid system, where the diesel genset is rotating on a common shaft with the pump. Regenerated power can be recycled to other simultaneous functions needing power or converted back to the energy storage through the electric drive.

In a parallel hybrid drive, the original diesel engine can be replaced by a smaller one when the task of the electric machine is to take care of the positive and negative power peaks in the system. The electric machine is directly attached on the diesel crankshaft to build a genset. Depending on the power flow and control of the system, the electric energy storage selected can be either a battery or a supercapacitor. Figure 3.1 illustrates a parallel hybrid system.

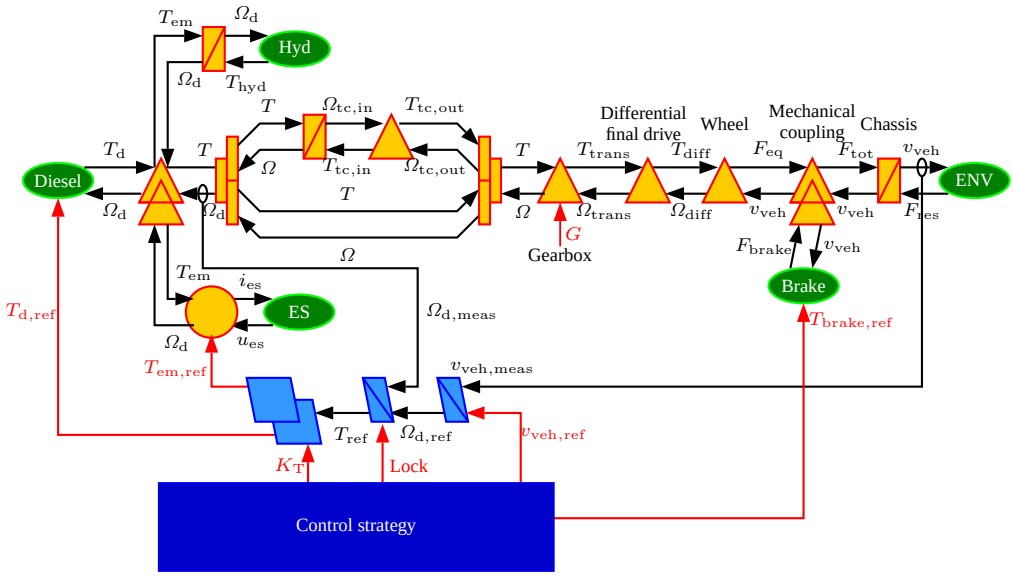

Fig. 3.1: EMR of the parallel hybrid system.

Figure 3.2 shows the control principle of the parallel hybrid system. In a parallel hybrid system, the genset speed is the control object. By the appropriate dimensioning of the genset and the transmission with respect to the load cycle, it is possible to drive the genset at a desired reference speed irrespective of the load of the system. The reference speed of the diesel engine is selected according to the velocity of the mobile machine. Both the diesel engine and the electric machine torque controllers participate in keeping the desired speed. The electric machine can react in milliseconds while the diesel engine reacts in hundreds of milliseconds. A low-pass filter (LPF) affects the transient capability of the diesel engine. The lower is the limiting frequency of the LPF, the less the diesel engine reacts to load changes. The SoC of the storage affects the torque reference of the diesel engine.

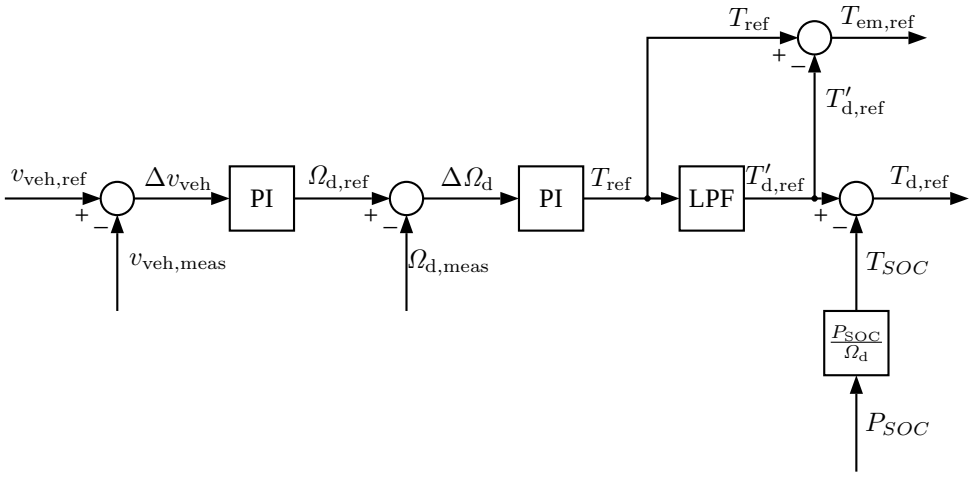

Fig. 3.2: Control principle of the parallel hybrid system.

The SoC-dependent power reference P_{SOC} defining the battery charging power is [109]

$$P_{SOC} = k_{\mathrm{SOC}} \tan\left(\frac{\pi}{2}\frac{SOC_{\mathrm{ref}} - SOC\,(t)}{\Delta SOC}\right), \tag{3.1}$$

where ΔSOC is the maximum allowed SoC deviation.

Figure 3.3 depicts the charging power P_{SOC} of the energy storage. The lower the SoC is, the higher power is needed. If the storage charge tends to reach too high values, the less power from the diesel will be asked for, and correspondingly, the electric machine on the same shaft produces a larger proportion of the mechanical power needed.

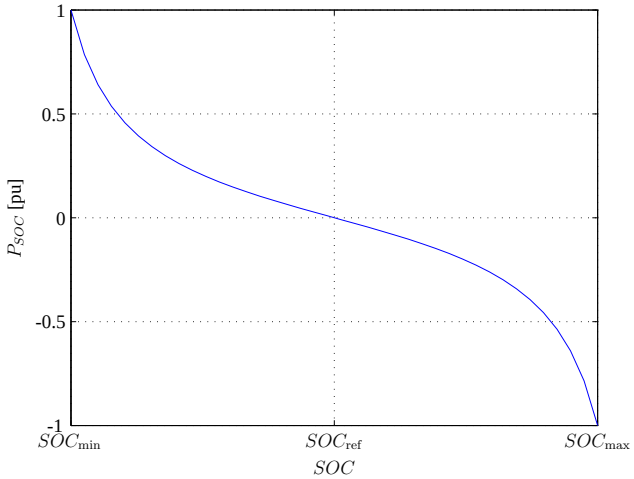

Fig. 3.3: Charging power based on the SoC of the battery or supercapacitor.

Advantages of the parallel hybrid system:

+ often the simplest first step to be taken when a new hybrid machine is built based on a traditional diesel-driven machine,
+ direct pump control of the working hydraulics, which guarantees both minimum losses in the control and provides an option for energy recovery,
+ recycling of the recovered energy between the actuators and
+ only one electric machine drive with only one converter and energy storage needed

and challenges:

– energy recovery from the traction drive is possible only when the torque converter is locked,
– the operating range of the diesel motor cannot be freely selected according to the needs of a certain operation while another, more important, operation dictates the diesel speed and
– optimal control of a parallel hybrid system is complicated.

3.2 Parallel-series hybrid system

Again, the diesel genset provides all the mechanical power needed for the hydraulic system but the traction system is now implemented by an electric drive. Figure 3.4 illustrates the main components of a parallel-series hybrid system. The pumps are on the same shaft with the genset. As the traction drive now has no mechanical connection to the genset, the genset speed can be selected independent of the traction, which helps in controlling the hydraulic systems. As there is no mechanical connection, there is neither need for a torque converter, and an electric traction machine alone can be responsible for the propulsion torque of the working machine. However, there is a need for a gearbox and a final drive gear. If only the final drive were present, the traction motor dimensioning would become very large.

In the parallel-series hybrid system, the original diesel engine can be replaced by a significantly smaller diesel engine. The traction system is converted into a series hybrid system. The electric energy storage can again be implemented either by a battery or a supercapacitor.

In the parallel-series hybrid system, the reference torque of the diesel engine depends on the diesel reference power. The power should be produced with as high efficiency as possible. Therefore, the reference speed of the diesel is selected according to the efficiency map. Both the diesel and electric machine controls affect the speed control. The propulsion motor is speed controlled. Its torque is defined in the speed control chain by the speed controller tuning parameters based on the difference between the actual and reference speeds. Figure 3.5 presents a block diagram of the system.

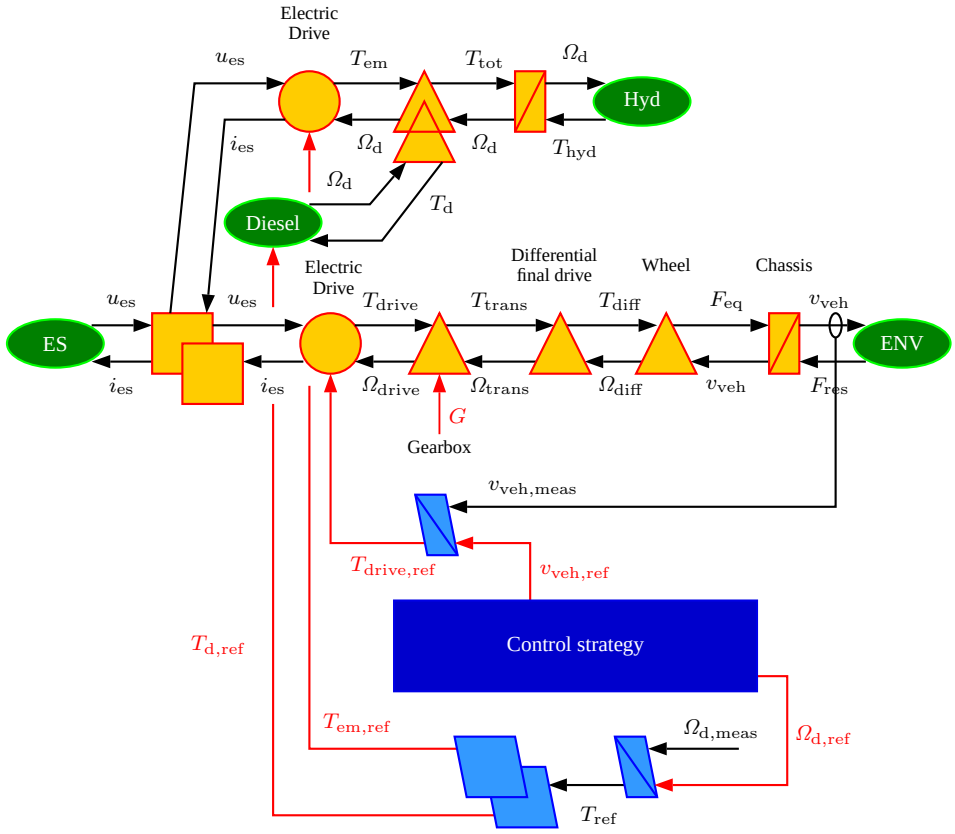

Fig. 3.4: EMR of the parallel-series hybrid system.

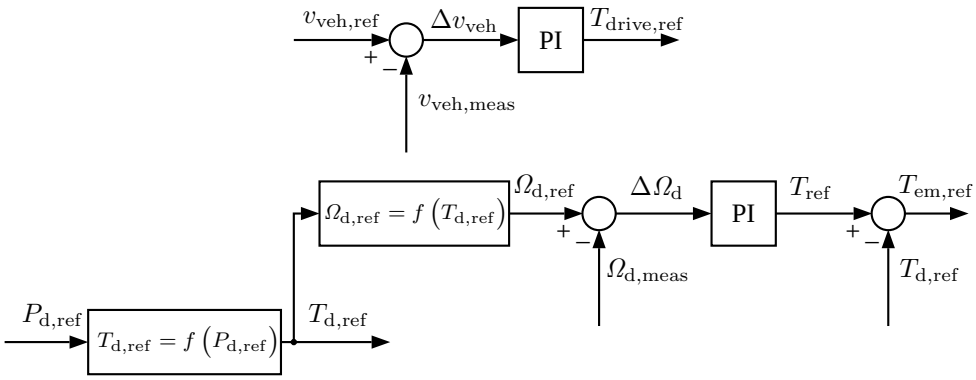

Fig. 3.5: Control principle of the parallel-series hybrid system.

Benefits of the parallel-series hybrid mobile machine:

+ direct pump control of the hydraulic system enabling high efficiency,
+ direct energy recycling between the different loops of the hydraulic system without intermediate conversion into electricity,
+ no highly lossy torque converter; energy recovery from the traction is easy and
+ independent control of the traction motor; no direct effect on the genset speed, and therefore, on the hydraulic pump control

and challenges:

– the diesel speed is still not freely selectable as the hydraulic system needs a certain mechanical speed even though the power of the system should be low, and
– system control is complicated.

3.3 Series hybrid system

In a series hybrid system, the diesel engine is totally disconnected from the mechanics. All the power for all working machine functions is delivered electrically. Both the traction and the hydraulic systems are fully electric drive operated. Despite the mechanical disconnection, the hydraulic pumps are still pump-motor units in this case, even though there might also be an option of driving the hydraulic systems with separate fixed displacement hydraulic machines capable of rotating in both directions and thereby allowing full electric drive control for the position of the hydraulic cylinders. However, pump-motor units provide a simpler configuration as only one electric machine is needed to rotate all the pumps.

The traction is constructed with a traction electric machine, gearbox and a fixed final drive. In a series hybrid system, the traction motor, the hydraulics motor and the diesel motor can all be controlled separately based on the long-term balance of the electric energy storage. Therefore, the diesel engine can really be operated close to its best operating point.

In a series hybrid drive, the original diesel can be replaced by a significantly smaller diesel depending on the power capacity of the electric energy storage. The diesel genset now produces all the electric energy needed in the system to power the hydraulics-driving motor and the traction motor and to keep the SoC in the battery. Depending on the system configuration, the energy storage can be either a battery or a supercapacitor. In the case of a powerful and large enough electric energy storage, the diesel genset can be driven at the average power of the system in a high efficiency point providing the best possible efficiency of the generation. Another option is to drive the genset in the best efficiency point of the diesel and turn the

genset off when the battery is full. Figure 3.6 provides the block diagram of a series hybrid system.

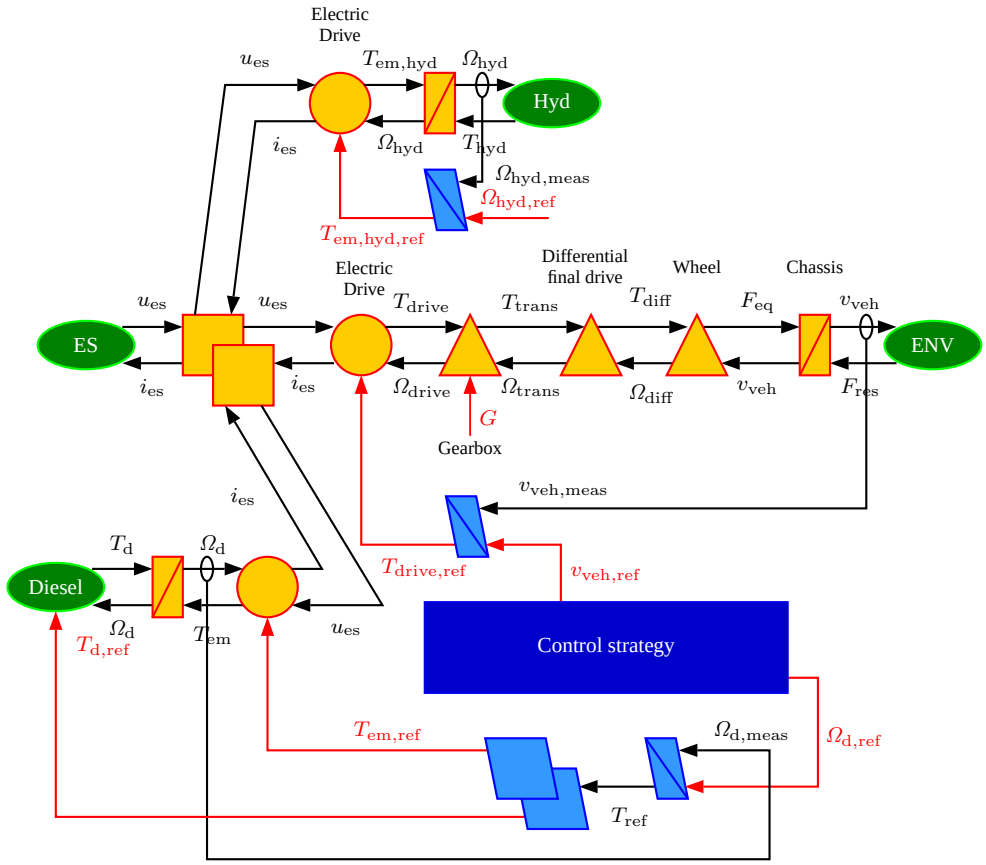

Fig. 3.6: EMR of the series hybrid system.

The power reference for the diesel in the series hybrid system depends on the load power and SoC of the electric energy storage. The power reference is produced by using the load instantaneous power $P_{\text{load}}(t)$ and the load moving average power $P_{\text{load,mave}}(t) = \int_{t-t_p}^{t} \frac{P_{\text{load}}(t)}{t_p} \mathrm{d}t$, where t_p indicates how long a period is used for averaging the power. A long period needs a high energy capacity in the battery. The instantaneous power and moving average power will be weighted by C_1 and C_2

$$P'_{\text{d,ref}}(t) = C_1 P_{\text{load}}(t) + C_2 P_{\text{load,mave}}(t), \tag{3.2}$$

$0 \leq C_1 \leq 1$ and $C_2 = 1 - C_1$.

In addition to the previous power reference, a SoC-dependent power reference P_{SOC} must be added to the genset power reference, and the power reference now calculated will be low-pass-filtered to guarantee a smooth control of the diesel. The diesel speed and generator torque references will be selected according to the power reference calculated to reach the best possible genset efficiency. The optimal torque reference function is produced by the diesel efficiency map, and therefore, the reference speed of the diesel is selected accordingly.

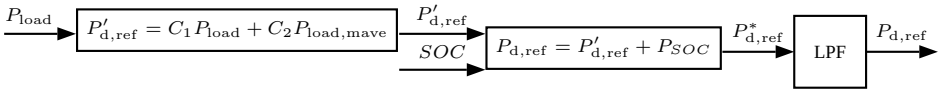

Fig. 3.7: Determining the diesel engine reference power.

The traction motor and the motors driving the working hydraulics are speed controlled. The traction motor torque reference is generated in the speed controller based on the error between the reference speed and the actual speed. The speed controller of the hydraulics motor works similarly. Figure 3.8 presents the main idea of controlling the motors of the series hybrid working machine.

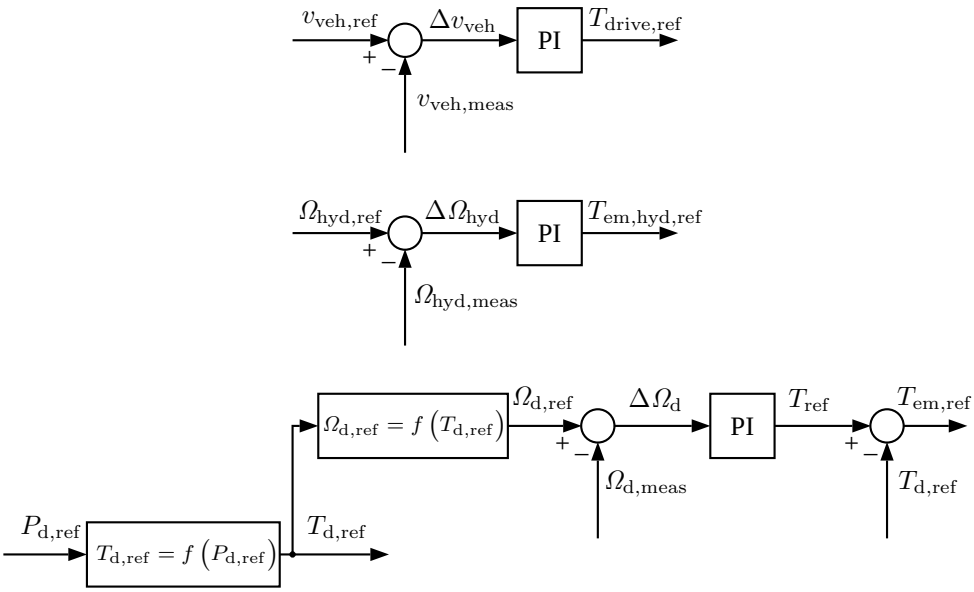

Fig. 3.8: Control principle of the series hybrid system.

Benefits of a series hybrid working machine:

+ working hydraulics can freely be implemented by the pump control guaranteeing the highest possible flexibility and energy efficiency,
+ energy recycling is possible between different functions,
+ no torque converter required; energy recovery from the driving movement is easy,
+ no mechanical connection between the hydraulics and the traction enables free control,
+ diesel operating point can be selected freely and
+ system control is straightforward and easy

and challenges:

- at least three electric machines and their power electronic units are needed,
- direct pump control often needs several units to achieve flexible behaviour and
- large changes are needed in the machine configuration when an existing working machine is converted into a series hybrid one.

Chapter 4

Case study and results

In the case study, a 60 000 kg working machine is studied. Its original diesel engine can yield 300 kW of power. The transmission is implemented by using a non-lock-up torque converter, a four-step gearbox and a final drive. The machine has three servo-valve-controlled hydraulic functions. There are no options for energy recovery neither from the traction nor the hydraulics.

4.1 Hybridization process

Hybridization of a working machine commences by defining the work cycles and corresponding loads for all the main components of the machine. In this work, the basic working operations of the case machine have originally been measured from an actual diesel-operated machine working in its normal working environment. The basic operations have been used to determine the work cycles for the machine by combining different basic operations in series. After defining or measuring an actual work cycle, the cycle has to be analysed. The work cycle should reveal the purpose for which the energy is consumed and whether there are cycles that provide recovery opportunities. At least the following characteristic parameters have to be determined: the maximum power $P_{\mathrm{load,max}}$, average power $P_{\mathrm{load,mean}}$ and maximum energy $E_{\mathrm{load,max}}$ of a single action.

The hybrid system type will be selected based on the working machine work cycle. There are no universal guidelines for the selection. Instead, depending on the work cycle and dimensioning of the machine, any hybridization type can be the best. Obviously, the history of the model series affects the selection of the hybrid system. The manufacturer has to decide how radical changes it is ready to make to the machine. A parallel hybrid system can be built with minimum changes to an existing diesel-operated machine, while the series hybrid system results in a total redesign of the machine.

In a series hybrid system, the traction motor is dimensioned according to the performance requirements of the machine using the speed reference as an input. The driving motor of the hydraulic system instead is dimensioned based on the load caused by the hydraulics. Dimensioning of the electric energy storage of the system, the diesel engine and the genset generator all depend on each other. The most challenging task in a hybridization process is to find the best match for the dimensioning of the electric energy storage, the diesel motor size and the electrical machine performance in a certain mobile working machine to minimize the fuel consumption. After the selection of the hybrid system type and components, the fuel consumption in a typical work cycle is calculated by simulations, and the payback period of the hybridization is determined based on the fuel savings during the cycle. The process is iterative and must be repeated several times to find the optimum or desired payback period.

In a parallel hybrid system, the genset components, that is, the diesel engine and the electrical machine, must produce the maximum power needed from the mechanical power unit. It is possible to divide the maximum power in many ways between the diesel and the electrical machine. The preconditions are that the diesel power must be at least the average power of the system plus losses ($P_{\mathrm{d,max}} \geq P_{\mathrm{load,mean}} + P_{\mathrm{loss}}$) and that the diesel engine and the electrical machine together with the energy storage can produce the maximum power needed ($P_{\mathrm{d,max}} + P_{\mathrm{em,max}} \geq P_{\mathrm{load,max}}$). The power of the electric energy storage must be at least the maximum power of the electrical machine.

In a parallel-series hybrid system, the genset must be capable of yielding the maximum power of the working hydraulics ($P_{\mathrm{d,max}} + P_{\mathrm{em,max}} \geq P_{\mathrm{hyd,max}}$), the energy storage has to be able to produce the traction drive maximum power ($P_{\mathrm{es,max}} \geq P_{\mathrm{drive,max}}$), the diesel engine and the storage must be capable of delivering the maximum load power ($P_{\mathrm{d,max}} + P_{\mathrm{es,max}} \geq P_{\mathrm{load,max}}$) and the diesel engine power must be at least the average power of the load plus the losses ($P_{\mathrm{d,max}} \geq P_{\mathrm{load,mean}} + P_{\mathrm{loss}}$).

In a series hybrid system, the precondition is that the diesel and the energy storage together can supply the maximum power of the system ($P_{\mathrm{d,max}} + P_{\mathrm{es,max}} \geq P_{\mathrm{load,max}}$) and the diesel engine power must be at least the average power of the system plus the losses ($P_{\mathrm{d,max}} \geq P_{\mathrm{load,mean}} + P_{\mathrm{loss}}$).

The difficulty in selecting the main components for a hybrid system is that despite the boundary conditions, there is, in principle, an infinite number of combinations. An extra difficulty is imposed by the control of the system as it is possible to apply several different control methods, resulting again in different energy efficiencies of the system. The mathematical modelling of a hybrid system is so complicated that no simple optimization algorithms can be developed. In this work, a few different hybridization options are analysed in detail to be able to show their effects on the fuel economy. The dimensioning and component selections have partly been made in collaboration with actual machine manufacturers.

Hybridization process:

1. Load cycle definition
2. Selection of the hybridization type
   - Parallel hybrid
   - Parallel-series hybrid
   - Series hybrid
3. Dimensioning
   - Electric energy storage
   - Diesel engine
   - Electrical machine/machines
4. Fuel consumption and payback period

4.2 Work cycle

The work cycle of the original case machine has been defined by measurements in the authentic environment of the machine. The work cycle contains five different work functions. The working machine speed, the load mass and the power consumption of the working hydraulics have been defined in different work functions. Figs. 4.1a–4.1e show the speed, the mass and the working hydraulics power in per unit values during different work functions. Actuator 1 provides the main lifting function of the working machine whereas Actuators 2 and 3 are for secondary functions.

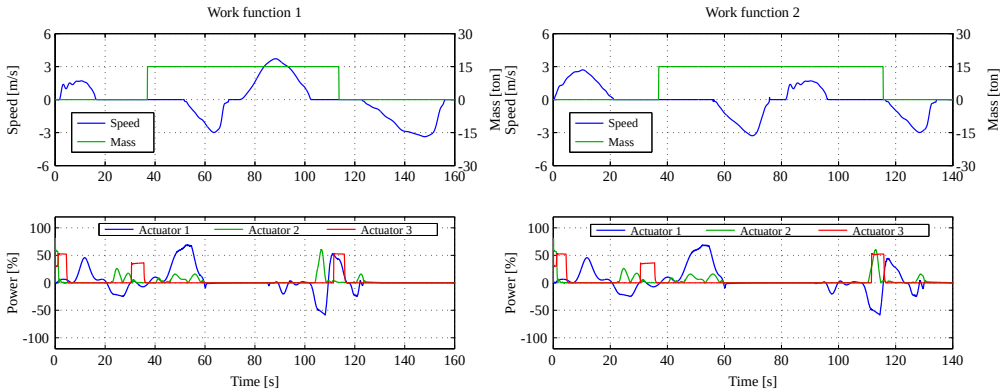

(a) Work function 1.

(b) Work function 2.

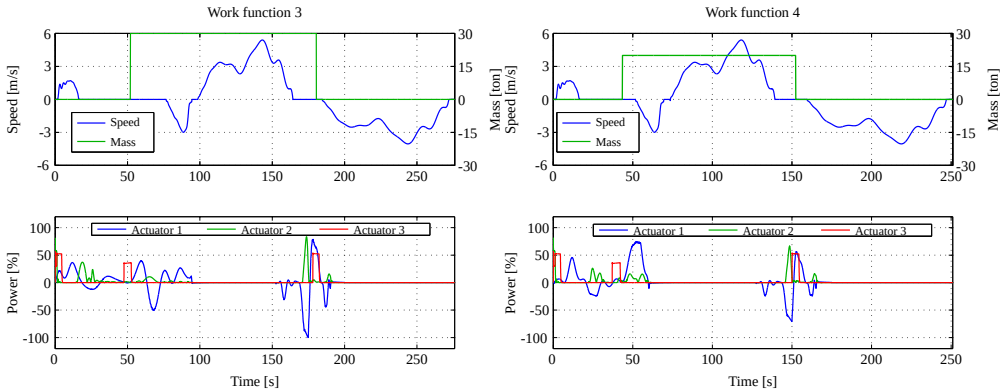

(c) Work function 3.

(d) Work function 4.

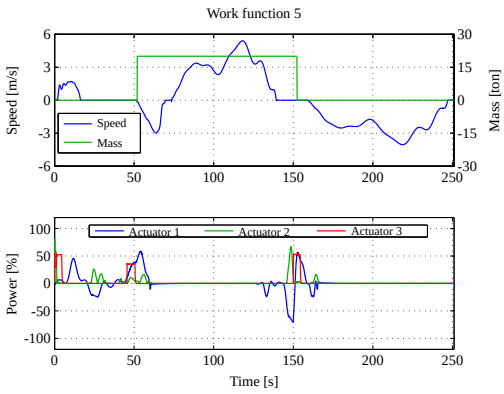

(e) Work function 5.

Fig. 4.1: Working machine speed, load mass and hydraulics per unit power in different work functions.

The complete work cycle has been composed by selecting and repeating the above-mentioned

work functions in a suitable way, see Table 4.1. The duration of the whole cycle is 4 h and 18 min.

Table 4.1: Composition of the work cycle for the case machine.

Work function	Quantity
Work function 1	17
Work function 2	16
Work function 3	20
Work function 4	15
Work function 5	5

Figure 4.2 illustrates the energy consumption of the above-mentioned work cycle with the original machine. The energies are in per unit values. Negative energies represent recovery options.

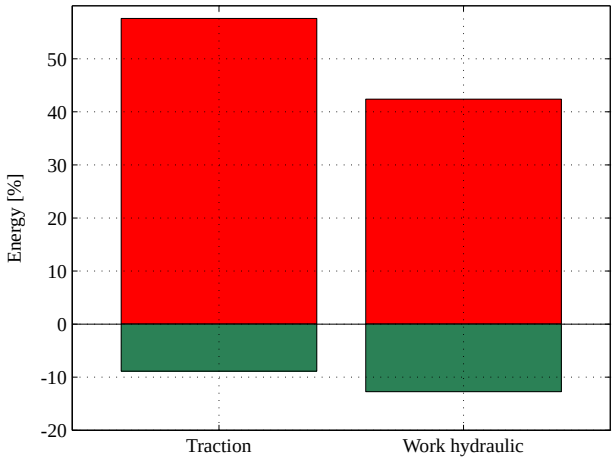

Fig. 4.2: Energy consumed by the traction and the hydraulics during a work cycle and the energy recoverable from the work cycle.

42% of the diesel output energy is used in the working hydraulics and 58% in the traction. 22% of the total energy use is recoverable. Energy can be recovered from the kinetic energy of the working machine and from hydraulic actuator 1. 41% (9% of the total energy) of the recoverable energy comes from the kinetic energy and 59% (13% of the total) from the potential energy of the hydraulic actuators.

Figure 4.3 presents the load cycle energy distribution. Actuator 1 needs 22%, actuator 2 10% and actuator 3 11% of the total energy. In the traction, 23% of the energy is consumed during

acceleration and 35% in friction. Rolling friction is the major friction component. The air drag and the acceleration of the wheel inertias are also taken into account.

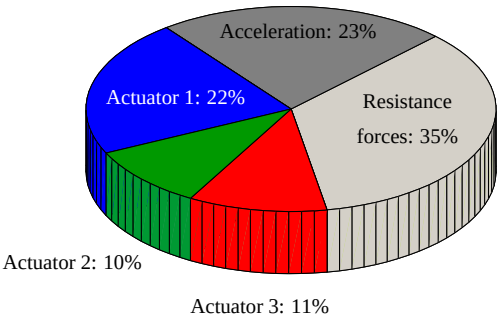

Fig. 4.3: Distribution of energy consumption between hydraulic actuators 1, 2 and 3 and traction (acceleration + friction).

Exact information of the work cycle shows where the energy is consumed and how much recovery potential there is in the work cycle. An analysis of the work cycle also reveals how much certain functions should be adjusted to improve the energy efficiency of the machine. If some actuator consumes a negligible amount of energy, it is probably not advisable to equip it with an energy recovery capability. On the other hand, the actuator that shows the highest potential for recovery should be studied in more detail from the energy efficiency perspective. In this case, actuator 1 provides good recovery potential while actuators 2 and 3 have only very limited potential for recovery.

4.3 Component dimensioning

Component dimensioning is based on the work cycle and performance requirements. This section studies the selection of the main components of the case machine.

4.3.1 Traction motor

In a series hybrid system, the traction motor alone provides the torque needed for the traction wheels. Therefore, the speed-torque curve of the traction motor, the gearbox and the final drive together define the traction drive performance, that is, the maximum acceleration, traction force and speed. When defining the main dimensions of the traction motor, the desired performance and the machine dimensions and mass have to be known in order to calculate the acceleration and friction forces. When these are known, based on the transmission properties, it is possible to define the operating points and time intervals of the traction drive in the speed–torque plane. In the following, the traction motor dimensioning process is described with a case example.

1. Working machine performance
   - Maximum speed
     - 30 $\mathrm{km/h}$
   - Traction force
     - Maximum traction force 250 kN at 2.5 $\mathrm{km/h}$
     - Traction force 70 kN at 8 $\mathrm{km/h}$
   - Acceleration
     - Acceleration between 0–15 $\mathrm{km/h}$, 13 s
     - Acceleration between 0–20 $\mathrm{km/h}$, 18 s
2. The main dimensions and mass of the machine
   - Working machine mass $m_{\mathrm{veh}} = 60\,000$ kg
   - Front surface $A_{\mathrm{f}} = 10\ \mathrm{m}^2$
   - Radius of the wheel $r_{\mathrm{wheel}} = 0.8$ m
3. Definition of the friction forces F_{res}; see Section 2.6
   - Rolling friction F_{roll}
     - Rolling friction coefficient $k = 0.02$
   - Force F_{slope} caused by the surface inclination
     - Surface inclination $\beta = 0$ rad
   - Air drag F_{air}
     - Air drag coefficienct $C_{\mathrm{d}} = 0.79$
4. Definition of the speed reference for the machine $v_{\mathrm{veh,ref}}$ based for instance on measurements
5. Gear ratios and efficiencies
   - Final drive
     - Final drive gear ratio $i_{\mathrm{diff}} = 45$
     - Efficiency $\eta_{\mathrm{diff}} = 0.90$
   - Gearbox
     - Gear ratios $i_{\mathrm{trans}}\,(G) = [-0.63, -2.2, -4.2,\ 4.2,\ 2.2,\ 1.4,\ 0.97,\ 0.63]$
     - Efficiency $\eta_{\mathrm{trans}} = 0.92$
6. Definition of the traction motor working points in the (n, T) plane.
   - $T_{\mathrm{em}} = \frac{m_{\mathrm{veh}} a + F_{\mathrm{res}}}{i_{\mathrm{trans}}(G) i_{\mathrm{diff}} \eta_{\mathrm{trans}} \eta_{\mathrm{diff}}} r_{\mathrm{wheel}}$
   - $n_{\mathrm{em}} = 60 \frac{v_{\mathrm{veh,ref}} i_{\mathrm{trans}}(G) i_{\mathrm{diff}}}{2\pi r_{\mathrm{wheel}}}$

The working points for the traction motor of the series hybrid drive have been calculated based on the above information with the work cycles given in Section 4.2. Figure 4.4 shows the gear shifts. The red arrows indicate the speeds at which the gear is shifted to a higher speed, and the blue arrows show the places where the gear ratio is changed to a lower speed.

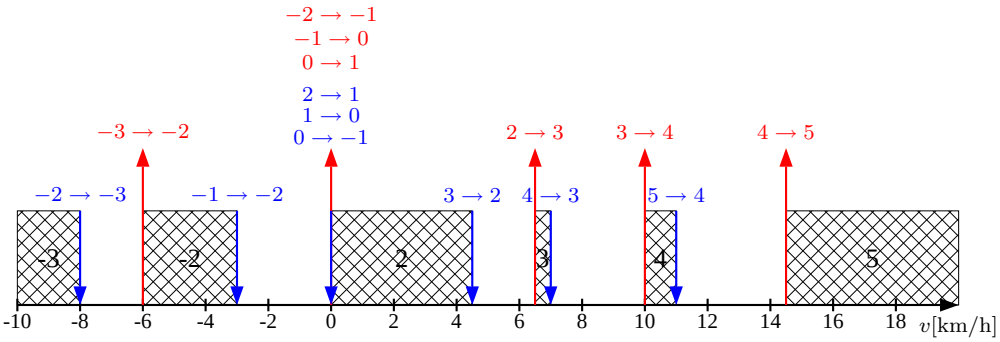

Fig. 4.4: Gear shifts.

The dimensioning of the traction motor of a series hybrid system is based on the operating range of the traction motor. Figs. 4.5a–4.5d show the traction motor speed, torque and power in different work functions.

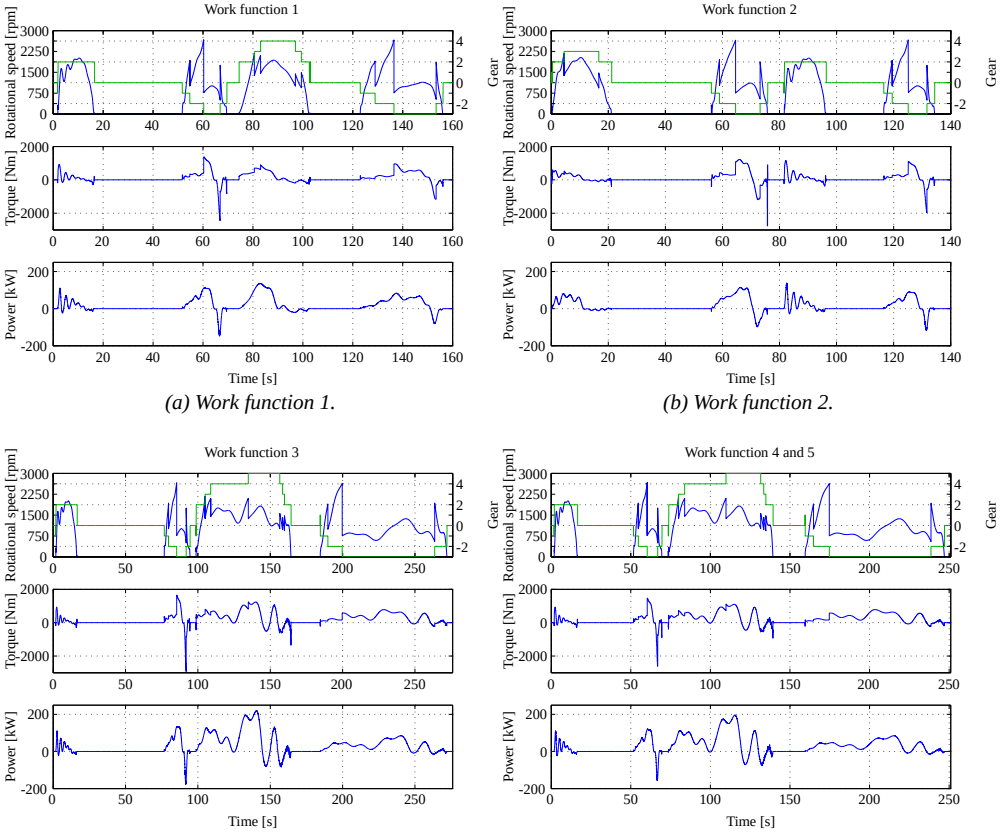

(a) Work function 1. *(b) Work function 2.*

(c) Work function 3. *(d) Work functions 4 and 5.*

Fig. 4.5: Traction motor speed, torque and power. The gear ratio is also indicated.

During different work functions, the maximum torque needed is about 1655 Nm; however, during deceleration the traction motor should be capable of braking at a -3000 Nm torque. It is not necessarily advisable to dimension the traction motor or its converter large enough to be capable of braking with the desired torque. Mechanical brakes can also be used if this can be proven to be the most economical solution. Table 4.2 gives the traction motor RMS powers and torques in different work functions.

Table 4.2: Traction motor RMS powers and torques in different work functions.

Work function	$P_{\mathrm{drive,RMS}}$ [kW]	$T_{\mathrm{drive,RMS}}$ [Nm]
Work function 1	43	351
Work function 2	38	349
Work function 3	60	438
Work function 4 and 5	57	424

Figure 4.6 shows the motor working range in the rotating torque–speed plane with per unit time periods for the work cycle presented above in Table 4.1. The traction motor operation is given with absolute torque values, which means that the presentation contains both positive and negative torques. However, negative torques below -1655 Nm are not included in the presentation. The traction motor is, therefore, not capable of utilizing all the braking energy.

The performance requirements define the working points that the motor has to meet. The maximum speed of the machine is 30 $\mathrm{km/h}$, and it is reached with the fifth gear at the traction motor rotational speed of 2820 rpm. The maximum traction force (250 kN at 2.5 $\mathrm{km/h}$) corresponds to the traction motor operating point with the first gear at 1570 rpm and 1280 Nm. The traction force 70 kN at 8 $\mathrm{km/h}$ is reached at the third gear at 1670 rpm and 1075 Nm or with the fourth gear at 1160 rpm and 1550 Nm. Figure 4.6 also presents these performance requirement points (250 kN at 2.5 $\mathrm{km/h}$ the 1^{st} gear) and (70 kN at 8 $\mathrm{km/h}$ at the 3^{rd} or 4^{th} gear) as motor operating points.

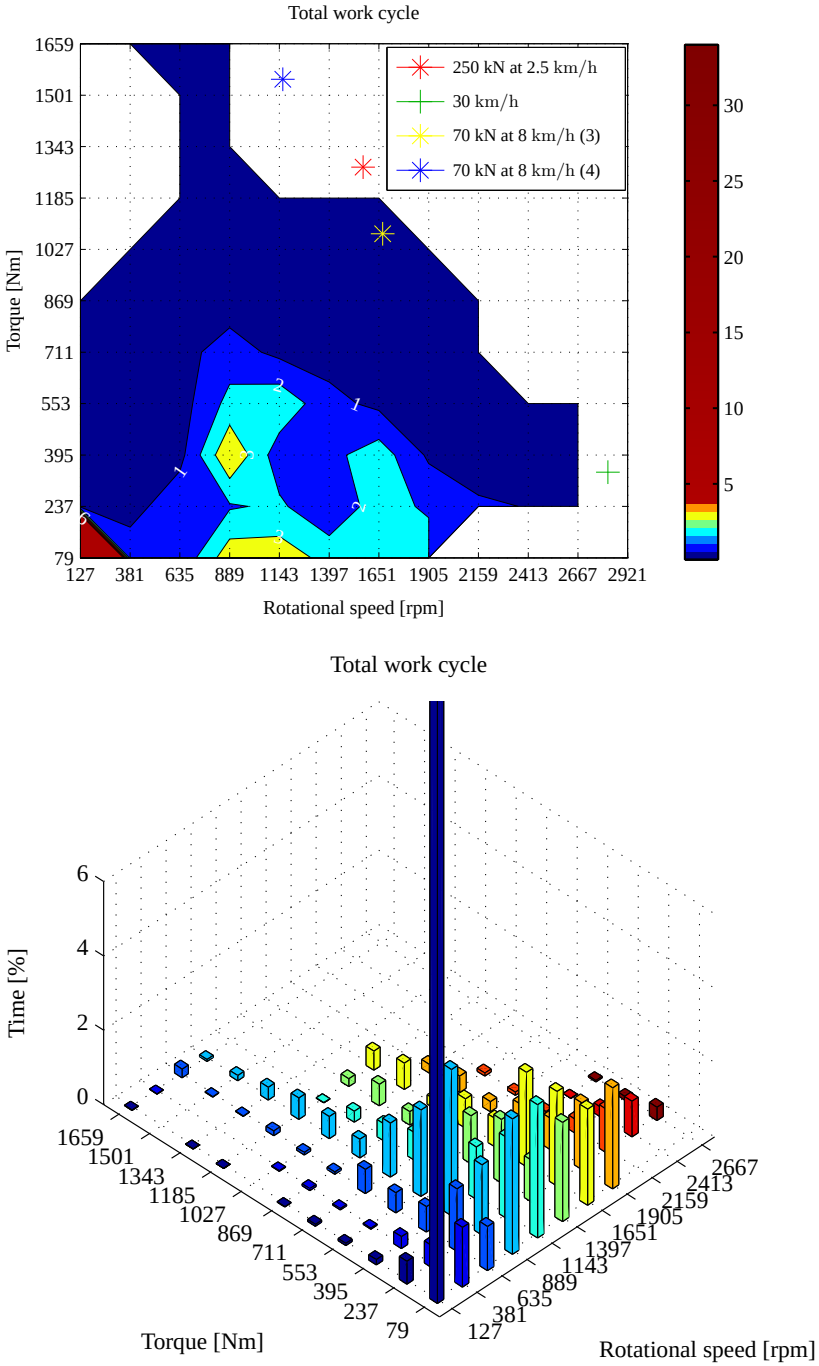

Fig. 4.6: Traction motor operation in the torque–speed plane with per unit time periods during the whole work cycle (17 periods of work function 1, 16 ps. of work function 2, 20 ps. of work function 3, 15 ps. of work function 4 and 5 ps. of work function 5). During the whole cycle, the motor operates at $T < 79$ Nm and $n < 127$ rpm 35% of the time. The RMS value of the load is 54 kW and the RMS torque 407 Nm. The figure also shows the required operating points.

The traction motor of the series hybrid drive could be for instance a water-cooled 90 kW (440 Nm and 1981 rpm) induction machine. The maximum torque of such a motor is 2000 Nm. The parameters of the motor have been given in Table 4.3 and its efficiency map in Fig. 4.7.

Table 4.3: 90 kW traction motor parameters.

Nominal power	P_n	90 kW
Nominal voltage	U_n	690 V
Nominal current	I_n	153 A
Nominal frequency	f_n	100 Hz
Number of pole pairs	p	3
Nominal speed	n_n	1981 rpm
Nominal torque	T_n	440 Nm
Stator resistance	R_s	0.037 Ω
Rotor resistance	R_r	0.046 Ω
Magnetizing inductance	L_m	10 mH
Stator leakage inductance	$L_{\mathrm{s}\sigma}$	0.41 mH
Rotor leakage inductance	$L_{\mathrm{r}\sigma}$	0.42 mH
Outer diameter of the stator	D_se	438 mm
Inner diameter of the stator	D_s	300 mm
Core length	l_c	278 mm
Mass	m	680 kg
Diameter	D	563 mm
Length	l	1034 mm

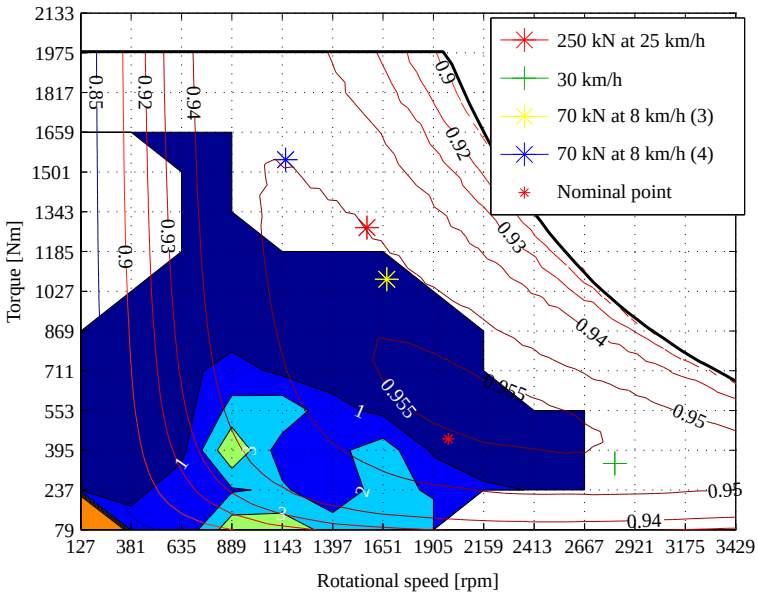

Fig. 4.7: Efficiency map of the traction motor.

The 90 kW induction motor designed for the mobile machine is well capable of meeting the performance requirements of the mobile machine. All the performance points are located in the operating area. The rated power and torque are higher than any RMS power or torque value in the whole work cycle or different work functions.

Figure 4.8 illustrates the accelerations $v_{\mathrm{veh,ref}}$ 0–15 $\mathrm{km/h}$ in 13 seconds and 0–20 $\mathrm{km/h}$ in 18 seconds and the performance with the induction motor designed above. The motor meets the requirements.

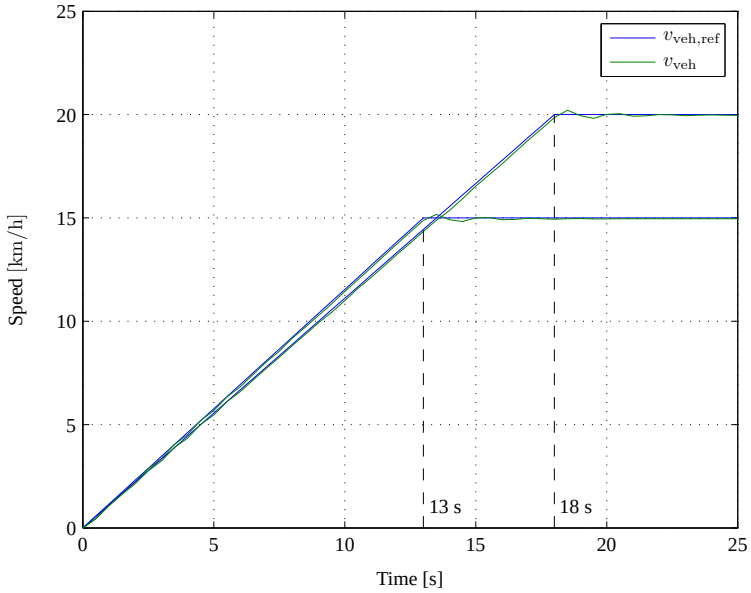

Fig. 4.8: Acceleration of the working machine by using the motor designed above 0–15 $\mathrm{km/h}$ *and 0–20* $\mathrm{km/h}$.

4.3.2 Dimensioning of the energy storage and energy storage lifetime

In the dimensioning of the energy storage, the boundary conditions are set by the mass, volume and price. Naturally, there has to be place for the energy storage in the machine, and therefore, a small storage volume is desired. Moreover, the voltage of the energy storage has to be such that the storage can be directly connected to the DC link of the inverter, unless a DC-DC converter is used. A key criterion in the dimensioning of the energy storage is that the storage can be implemented with components available in the market. Further, the lifetime of the energy storage has to be long enough, and the price of the storage should also be reasonable. Finally, the investment should be economically feasible.

Therefore, the capacity of the energy storage should not necessarily be so high that for instance all the recoverable power could be stored in it. For example, single high braking power peaks do not necessarily contain enough energy so that the power rating of the energy storage should be selected according to such a value.

The theoretical optimal dimensioning of the energy storage in a series hybrid drive can be determined by simulations. However, it may not be possible to implement the energy storage used in the simulations with an actual energy storage cell or module. Figure 4.9 illustrates the work cycle used to determine the energy storage capacity and its influence on the fuel consumption. This cycle consists of the work functions introduced in Section 4.2. Each of the functions is repeated once.

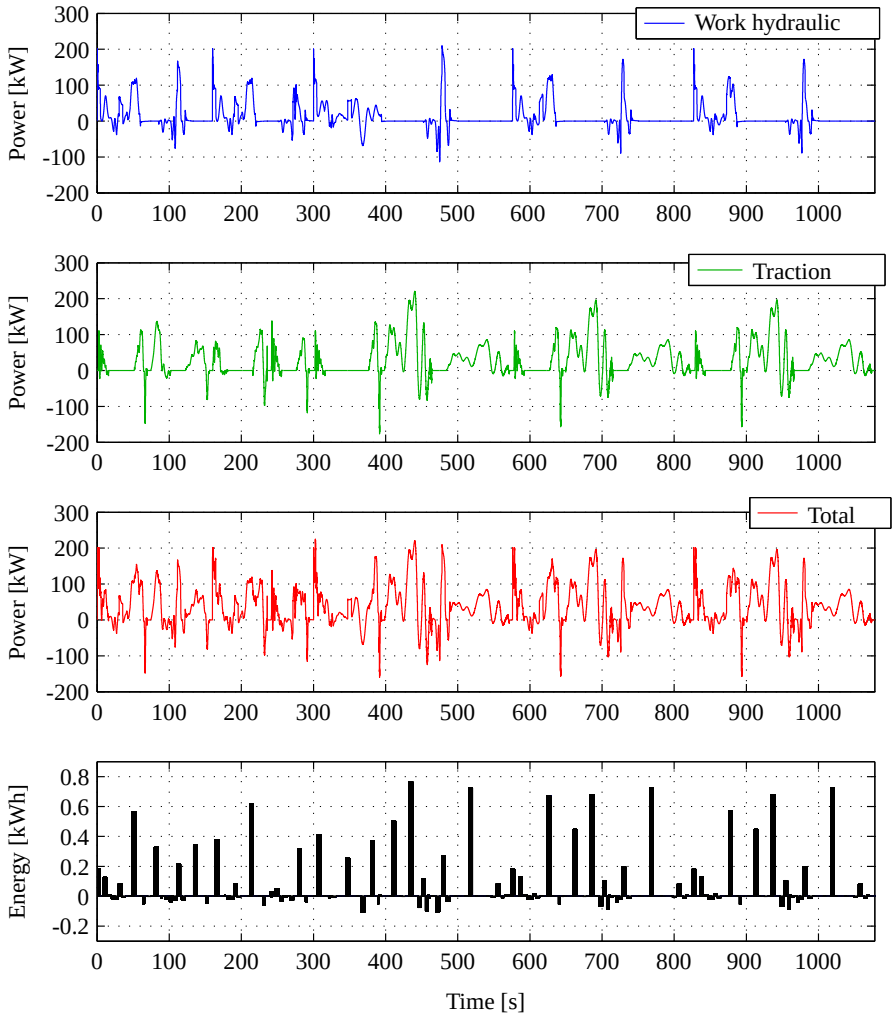

Fig. 4.9: Load cycle used in assessing the influence of the energy storage capacity on the mobile machine fuel consumption. The energies of individual power peaks are indicated in the lower illustration in the center of power peaks.

Figure 4.9 illustrates the power levels of the working hydraulics, the traction and the total power. The figure also shows the energy amounts of single power peaks. The maximum load power is 225 kW, the minimum power is –160 kW and the average power 40 kW. A single power peak contains 0.8 kWh of energy at maximum.

The theoretical optimal dimensioning of the energy storage in a series hybrid system is found by simulations.

- In the simulation, the following items are varied:
  - Energy capacity E_{es},
  - Power capacity P_{es},
  - Maximum power $P_{\mathrm{d,max}}$ of the diesel engine and
  - Control parameters (C_1, C_2, τ_{LPF}) of the diesel engine.

- The boundary conditions used in the simulations are:
  - The total output power of the diesel engine and the energy storage must be at least 225 kW.
  - The following error margins must be met:
    - error in the travelling length (Δs) < 2%, error in the speed (Δv_{veh}) < 2%, error in the working hydraulics energy (ΔE) < 5%.
  - The SoC at the end of the simulation must not have an error higher than $\pm 1\%$.
  - The no-load power of the diesel engine is 10% of the diesel engine maximum power or at least 10 kW.
    - Cutting down the power of the diesel engine does not have an impact on all no-load powers required. Indeed, the frictions of the diesel engine are reduced, yet the powers required by the auxiliary systems, such as lights, blowers, power steering and the like will remain.

Figure 4.10 illustrates the behaviour of the fuel consumption as a function of different power and energy capacities of the energy storage. The energy capacity is varied between 1 kWh and 19 kWh, and the power capacity is varied from 50 kW to 300 kW.

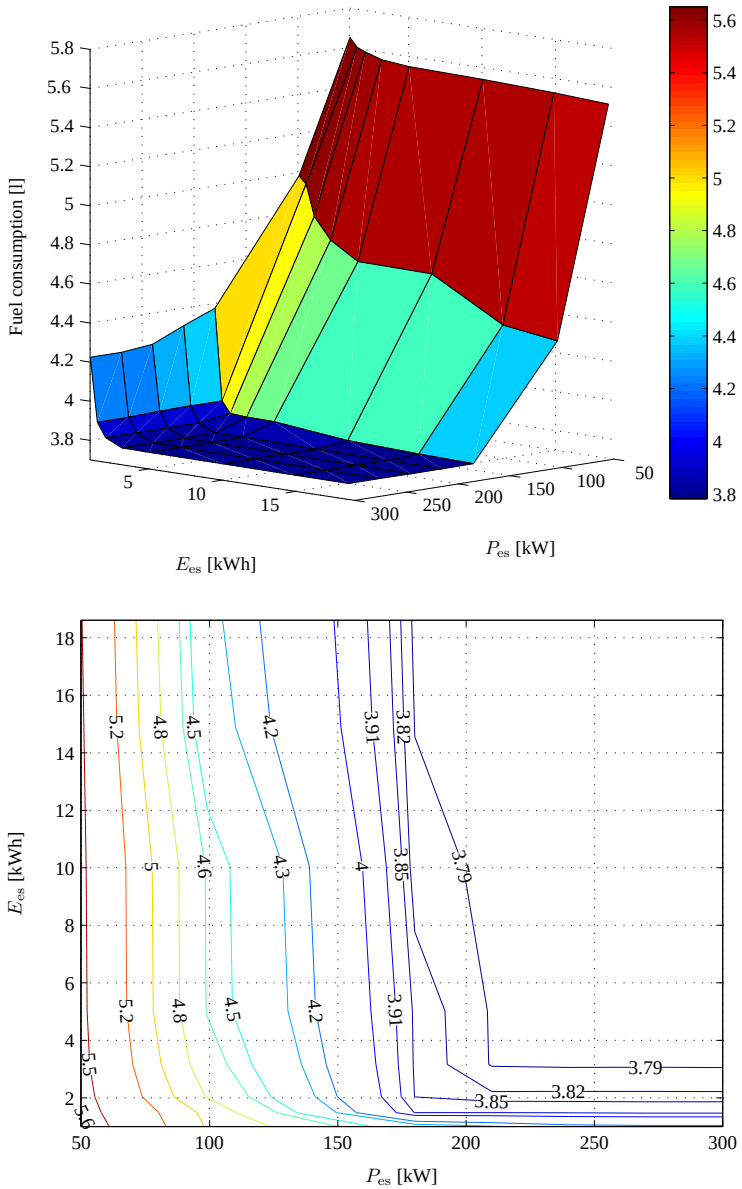

Fig. 4.10: Diesel fuel consumption in the series hybrid system as a function of power and energy capacities of the energy storage. The diesel engine size is selected in each case so that the minimum fuel consumption is reached.

The smaller the energy storage is, the higher is the fuel consumption. With a 50 kW, 1 kWh energy storage, the consumption in the cycle is 5.7 litres. With a 300 kW and 20 kWh energy storage, the consumption is 3.8 litres. The power capacity of the storage is more important than the energy capacity.

However, it is difficult to cover the above areas with practical components as high-power super capacitors have too small an energy capacity. The most viable storage in this case seems to be a large enough LiTi battery that can reach the desired power. In such a case, the energy storage capability is more than enough for the application.

When a low-power capacity storage is used, the diesel engine has to react faster in transients, which again increases the consumption. Using a low-power storage also results in a need for a large diesel engine, which has a higher no-load consumption.

With a high-power capacity energy storage, the diesel engine does not have to react at all to load changes. The task of the diesel engine in such a case is to take care of the SoC of the storage. The diesel power variations can be kept to a minimum, and in theory, a 40 kW diesel could work at a constant power resulting in a consumption of 3.7 l and an efficiency of 0.41. The series hybrid could also be constructed without any energy storage. In such a case, the diesel engine has to react to all power needs.

Figure 4.11 illustrates the minimum and maximum powers of the diesel engine and the energy efficiency of the engine using energy storages of different sizes.

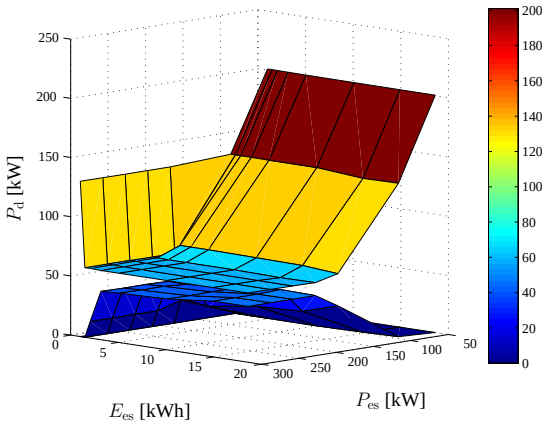

(a) Optimum diesel sizes with energy storages of different power and energy capacities.

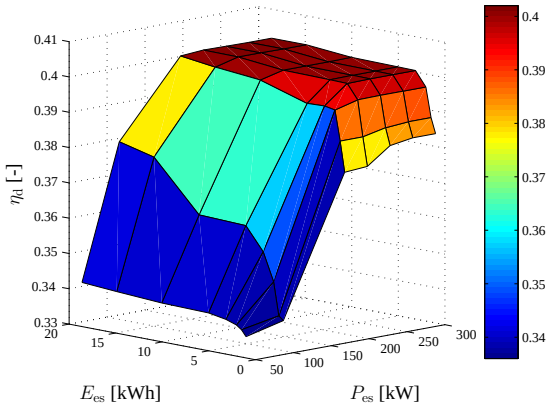

(b) Energy efficiency of the diesel engine in the work cycle.

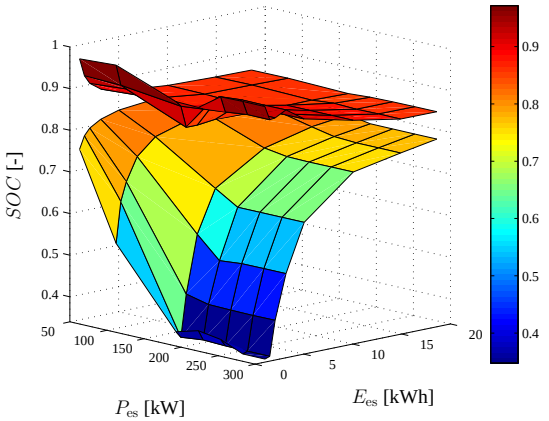

(c) Minimum and maximum SoCs of the energy storage during the work cycle.

Fig. 4.11: Diesel engine efficiency, minimum and maximum powers and SoC of the energy storage during the work cycle.

When an electric energy storage with a 50 kW peak power is used, the rated power of the diesel engine has to be 224 kW. When an electric energy storage with a 100 kW peak power is used, a diesel engine with the rated power of 150 kW is employed. In other cases, the rated power of the diesel engine is selected to be 66 kW. The larger an energy storage (measured by power and energy capacity) is used, the smaller the diesel engine power variation is during the load cycle. Figure 4.11b depicts the diesel engine energy efficiency during the load cycle with different energy storages. The diesel engine efficiency varies, depending on the energy storage capacity, between 0.33 and 0.40. The larger an energy storage is used, the smaller power variations the diesel engine will experience during the load cycle. In such a case, the diesel can be made to operate as close to its best operating point as possible. Further, emissions are reduced when the power variations of the diesel engine are small. With a large energy storage, the system dynamics is improved. A future diesel engine will react more and more slowly to transients, and its dynamics will be considerably smaller than the dynamics of electrical machines.

Figure 4.11c illustrates the maximum and minimum SoCs. In a large-capacity storage, the SoC varies only slightly and the lifetime of the storage is thereby longer. In a small energy storage, the SoC varies a lot; for example with a 1 kWh storage, the SoC varies between 0.35 and 0.97. Such a storage must be a supercapacitor as batteries do not tolerate such a behaviour. In the simulations, the supercapacitor voltage varies between 60 and 100% of the rated value. Such a voltage variation range is possible with a slightly overdimensioned voltage tolerance of the converter without a DC-DC converter, which, owing to its low efficiency, easily degrades the energy efficiency of a hybrid system.

As stated above in Section 2.2, the energy storages suitable for hybrid mobile working machines are the LiTi battery and the supercapacitor. In this study, the consideration of the physical dimensions and prices of energy storages has been limited to storages suitable for working machine applications. The physical dimensions of the energy storage have been calculated by using the values given in Table 4.4 for LiTi batteries and supercapacitors.

Table 4.4: Specific energy, specific power, energy density, power density and price of a LiTi battery and a supercapacitor [110], [111].

	Lithium titanate	Supercapacitor
Specific energy $[\mathrm{Wh/kg}]$	51.9	2.26
Specific power $[\mathrm{W/kg}]$	799	3600
Energy density $[\mathrm{Wh/l}]$	106	2
Power density $[\mathrm{W/l}]$	1673	3124
Price $[€/\mathrm{kWh}]$	1800	40 000

In the applied energy-power range, the energy capacity of a LiTi battery is determined by the power required. Hence, there is no 300 kW LiTi battery available, the energy of which would be only 1 kWh. The power of a supercapacitor, again, is determined based on the

energy capacity. Thus, there is no 1 kWh supercapacitor available, the power of which would be only 50 kW. Figure 4.12 shows the areas in the power–energy plane covered by the LiTi battery and the supercapacitor, when the allowed maximum volume of the energy storage is 3 m^3. The maximum volume 3 m^3 of the LiTi battery does not limit the area covered in the power-energy plane, but the limit is set by the specific energy to specific power ratio of the battery.

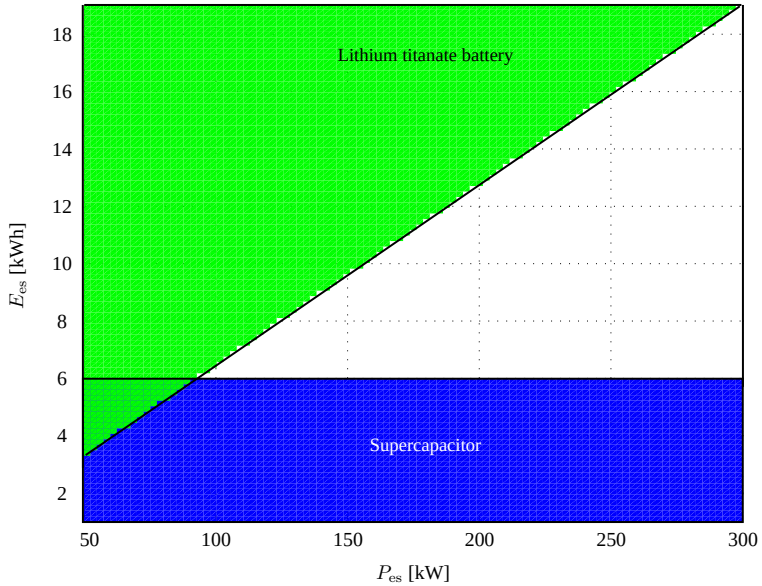

Fig. 4.12: Areas in the power–energy plane covered by the LiTi battery and the supercapacitor, when the maximum allowed volume of the energy storage is 3 m^3. The maximum volume 3 m^3 of the LiTi battery does not limit the area covered in the power-energy plane, but the limit is set by the specific energy to specific power ratio of the battery.

Hence, the power–energy plane applied in the calculations cannot be achieved in full with a LiTi battery or a supercapacitor. Figs. 4.13a and 4.13b depict the physical dimensions of the energy storage in the power–energy plane.

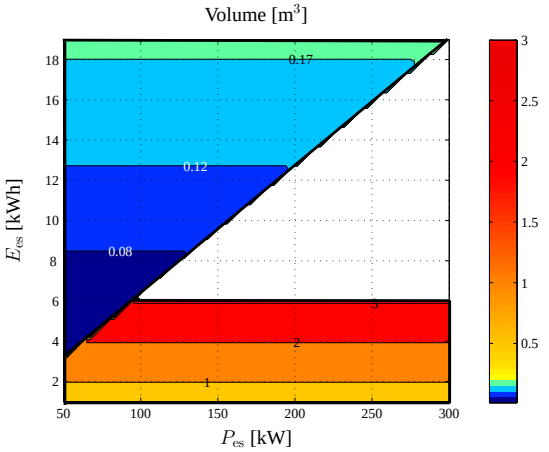

(a) Volume of the energy storage.

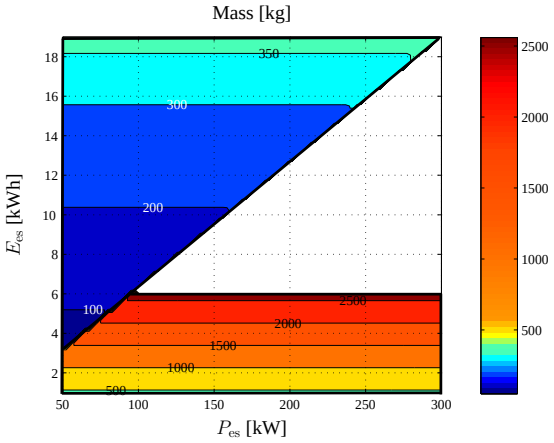

(b) Mass of the energy storage.

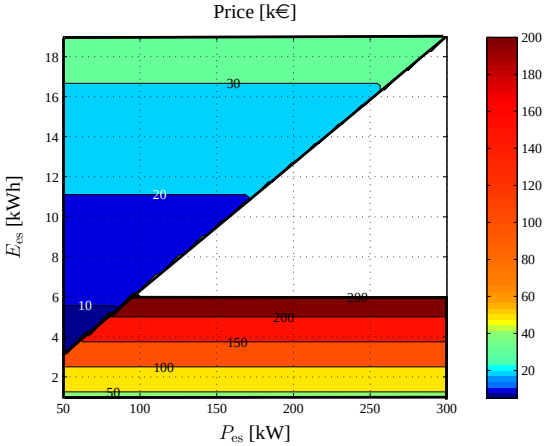

(c) Price of the energy storage.

Fig. 4.13: Volume, massa and price of the energy storage.

It is pointed out that both the volume and mass of the supercapacitor are significantly larger than those of the LiTi battery. Moreover, Fig. 4.13c provides a comparison of the energy storage prices; a LiTi battery seems to be a more viable choice for working machine applications than a supercapacitor, considering both the physical size and the price.

The hybrid systems addressed in this work have all been implemented without a DC-DC converter and using electrical machines of 400 V line-to-line voltage. In that case, the voltage level of the energy storage should be about 600 V to enable the implementation without a DC-DC converter. Hence, the above considerations are theoretical only, as it has not been investigated whether the energy storages can be built of commercially available LiTi or supercapacitor cells or modules so that the above voltage requirement is met.

Next, the study focuses on investigating what kinds of energy storage packages could be compiled from commercially available LiTi or supercapacitor cells or modules so that the above voltage requirement can be met. Table 4.5 presents the commercially available LiTi and supercapacitor modules by which the energy storages of the case hybrid working machine can be constructed.

Table 4.5: Voltage, power, energy, mass and volume of the commercially available LiTi and supercapacitor modules [110], [111].

	Lithium titanate	Supercapacitor
Module	Altairnano 24 V 60 Ah	Maxwell BMOD0063 125 V
Rated voltage $[\mathrm{V}]$	24	125
Power $[\mathrm{kW}]$	21.9	103
Energy $[\mathrm{Wh}]$	1400	136.7
Mass $[\mathrm{kg}]$	27.4	60.5
Volume $[\mathrm{m}^3]$	0.013	0.07

By applying the 24 V 60 Ah modules by Altairnano and connecting 26 modules in series, it is possible to construct an energy storage pack that meets the requirements of the working machine. Similarly, by using seven Maxwell BMOD0063125 V supercapacitors connected in series, an energy storage meeting the requirements is achieved. Table 4.6 gives the voltages, powers, energy capacities, physical dimensions and estimated prices of the energy storage packs constructed of the above modules.

Table 4.6: Energy storages compiled of the lithium titanate battery and supercapacitor modules commercially available.

	Lithium titanate battery pack	Supercapacitor pack
Connection	26 × Altairnano 24 V 60 Ah module in series	7 × Maxwell BMOD0063 125 V module in series
Rated voltage [V]	624	875
Power [kW]	355	721
Energy [kWh]	36.4	0.96
Mass [kg]	712	424
Volume [m^3]	0.34	0.49
Price [€]	60 000	40 000

Based on the theoretical approach of Fig. 4.13, we may conclude that the physical dimensions and price of the LiTi battery are lower than those of the supercapacitor. When taking into account the voltage requirement of the energy storage and constructing an energy storage of the modules commercially available, we obtain a LiTi battery for a working machine application, the energy capacity of which is significantly high, 36.4 kWh. However, also the physical dimensions and price of the battery pack increase. Nevertheless, the increase in the energy capacity has a positive impact on the lifetime of the battery, which is beneficial for the economical feasibility of the solution.

Lifetime calculation

The lifetime of a LiTi battery has been investigated in a solution introduced in Table 4.6 for a working machine application; that is, by connecting 26 Altairnano 24 V 60 Ah modules in series. Figure 4.14 depicts the power and SoC of the energy storage with a 36.4 kWh LiTi battery.

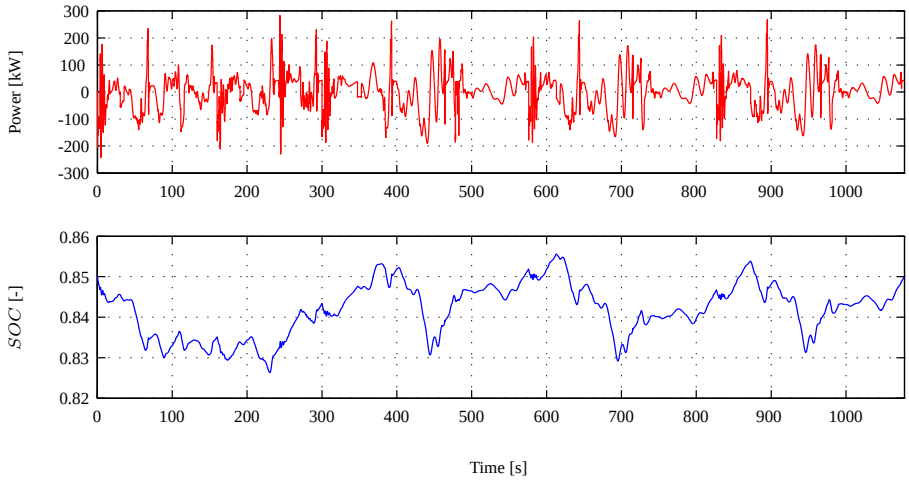

Fig. 4.14: Power and SoC of the energy storage with a 36.4 kWh LiTi battery.

In Section 2.2, the cycle life of a LiTi battery was given for different depths of discharge. In batteries used in hybrid working machines, the change in the depth of discharge DoD consists of a certain number of values occurring during a load cycle. Each of these DoD cycles reduces the lifetime of the battery. Cycles with different DoDs have been determined by a rainflow cycle method. In the rainflow method, the discharge cycles are idealized continuous-amplitude cycles [112].

The lifetime of an energy storage LT can be determined as follows

$$LT = \frac{t_{\text{cycle}}}{\sum_{i=1}^{n} \frac{N_i(DOD)}{CL_i(DOD)}}, \tag{4.1}$$

where t_{cycle} is the duration of the load cycle, N_i is the number of cycles with different DoDs during the loading and CL_i is the cycle life of the energy storage at different DoDs. We can produce an equation fit for the cycle life of the LiTi battery illustrated in Fig. 2.27 as follows

$$CL = 1 \cdot 10^8 DOD^{-2}. \tag{4.2}$$

Figure 4.15 gives the number of cycles with different DoDs.

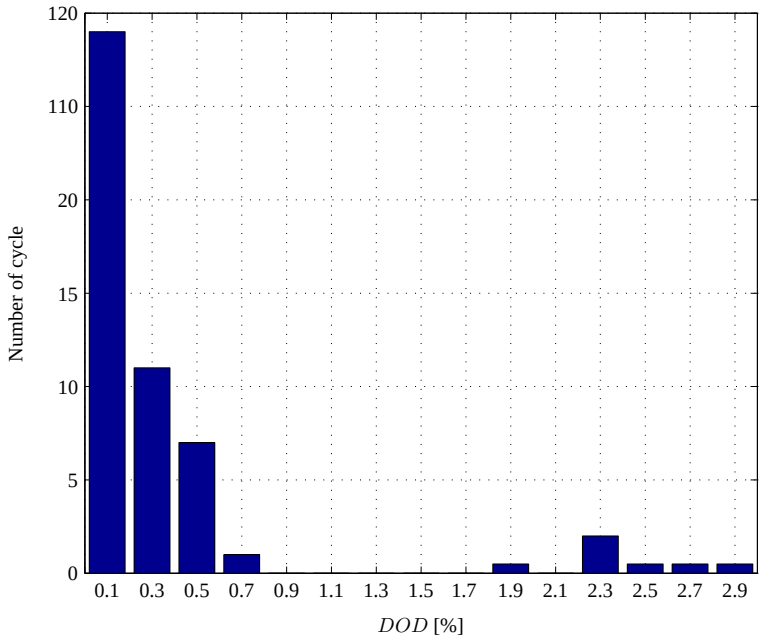

Fig. 4.15: Number of LiTi battery cycles with different DoDs.

Moreover, it has to be kept in mind that the initial state of charge of the battery is 85%. Hence,

the load cycle also includes a 0.5 cycle with a 25% of DoD. Table 4.7 lists the numbers of cycles with different DoDs during loading and the corresponding cycle lifes.

Table 4.7: Numbers of LiTi battery cycles with different DoDs.

DoD [%]	0.1	0.3	0.5	0.7	1.9	2.3	2.5	2.7	2.9	25
N_i	119	11	7	1	0.5	2	0.5	0.5	0.5	0.5
CL_i	10^{10}	$1 \cdot 10^9$	$4 \cdot 10^8$	$2 \cdot 10^8$	$3 \cdot 10^7$	$2 \cdot 10^7$	$2 \cdot 10^7$	$1 \cdot 10^7$	$1 \cdot 10^7$	$2 \cdot 10^5$

The lifetime of the LiTi battery determined by Eq. (4.1) is ten years. In the lifetime calculation, the battery temperature is assumed $35\,^{\circ}\mathrm{C}$. In actual use, the battery temperature varies, which should be taken into account when estimating the battery lifetime more accurately. However, it is crucial to guarantee the low temperature of the battery. $35\,^{\circ}\mathrm{C}$ may be a challenging level for many environments and may require a heat pump to cool the battery in warm ($50\,^{\circ}\mathrm{C}$) environments.

4.3.3 Dimensioning of the diesel genset

Dimensioning of the diesel genset is strongly dependent on the energy storage dimensioning. In a series hybrid system, the genset + energy storage power must equal the maximum power of the load. The genset must naturally be capable of producing at least the average power of the system. Normally, the highest efficiency of a diesel engine is reached at about 50–75% of the engine maximum power and at a considerably low speed. For example in the efficiency map of Fig. 2.32, the maxcimum efficiency of the diesel engine is found at a 75% power and about half of the speed corresponding to the maximum power. The diesel power must therefore be about 130–200% of the average power needed. The generator dimensioning should also be performed so that it should operate close to its maximum efficiency point.

4.4 Simulation results

Different hybridization alternatives have a significant impact on the machine fuel consumption. This section studies the fuel consumption of the case machine with different hybrid systems and their dimensioning. Parallel, parallel-series and series-hybrid systems have been simulated with three different diesel engine and energy storage dimensions. The boundary condition for each of the systems is that the original performance must be maintained.

4.4.1 Energy consumption of different hybrid systems

The energy consumption of different hybrid systems has been determined by simulating the machines by using the example work cycle. Each of the work functions have been simulated

separately and the fuel consumptions have been added up. Three different combinations for diesel engine energy storages have been used. In the parallel hybrid system, the combinations are the following: the energy storage peak powers are 50 kW, 100 kW and 150 kW, and the corresponding powers for the diesel diesel engine are 200 kW, 150 kW and 100 kW. In the parallel-series and series hybrid, the powers for the energy storage are 100 kW, 150 kW and 200 kW and for the diesel engine 150 kW, 100 kW and 66 kW; Table 4.8.

Table 4.8: Sizes of the diesel engine, the electrical machines and the energy storage used in different systems.

	Original	Parallel			Parallel-series			Series		
Diesel engine [kW]	300	200	150	100	150	100	66	150	100	66
Diesel engine idle power [kW]	30	20	15	10	15	10	10	15	10	10
Electrical machine [kW]	-	50	100	150	125	130	155	150	100	66
Drive motor [kW]	-	-	-	-	250	250	250	250	250	250
Working hydraulics electric motor [kW]	-	-	-	-	-	-	-	250	250	250
Energy storage power [kW]	-	50	100	150	100	150	200	100	150	200
Energy storage [kWh]	-	3	3	3	5	5	5	8	8	8

Figure 4.16 illustrates the fuel consumptions of the working machine compared with the consumption of the original working machine with the work cycle according to Table 4.1. The consumption figures given include the diesel transient consumption according to [97].

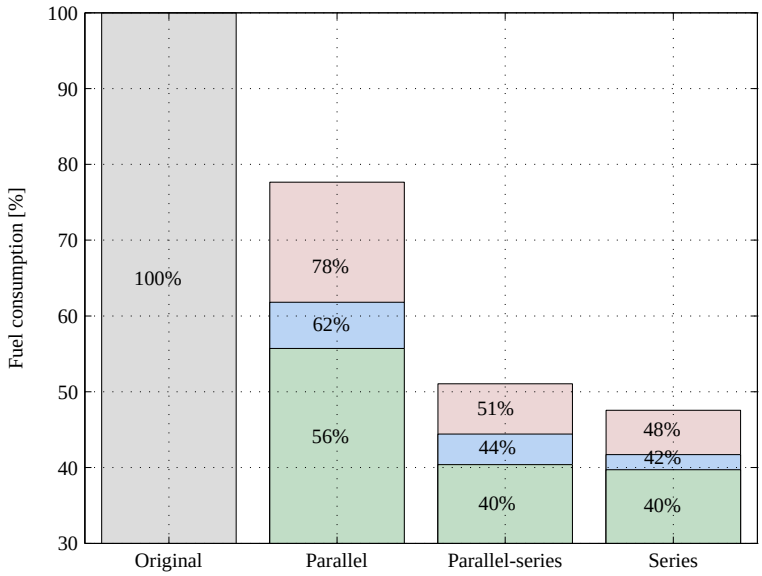

Fig. 4.16: Working machine per unit consumptions with different diesel engine and energy storage combinations, the diesel transient consumption included. The original machine consumption is 100%. Each system is simulated by using three different diesel engine and energy storage power combinations. In the parallel hybrid system P_{es} = 50 kW, P_{d} = 200 kW (red), P_{es} = 100 kW and P_{d} = 150 kW (blue) and P_{es} = 150 kW and P_{d} = 100 kW (green). In parallel-series and pure series hybrids P_{es} = 100 kW, P_{d} = 150 kW (red), P_{es} = 150 kW and P_{d} = 100 kW (blue) and P_{es} = 200 kW and P_{d} = 66 kW (green).

In all hybrid systems simulated, the fuel consumption increases when the rated power of the energy storage decreases and the diesel engine increases. Fuel consumption of the alternative hybrid systems and different maximum powers of the diesel engine and the energy storage are presented in Table 4.9.

Table 4.9: Fuel consumption of the alternative hybrid systems with different maximum powers of the diesel engine and the energy storage.

	Parallel			Parallel-series			Series		
Diesel engine [kW]	200	150	100	150	100	66	150	100	66
Energy storage power [kW]	50	100	150	100	150	200	100	150	200
Fuel consumption [%]	78	62	56	51	44	40	48	42	40

With a high-power energy storage, a small diesel engine can be chosen. Its no-load consumption is low compared with the original. In the simulations, the no-load power is 10% of the

rated power or at least 10 kW. A small diesel engine can be run close to its optimal efficiency point while a large diesel engine almost always has to run in non-optimal areas.

When using a large-power energy storage and a small diesel engine, no transient driving of the diesel engine is needed in practice, but it can very slowly move from one working point to another. The transient extra consumption is thereby avoided, and the suitable diesel engine can run close to its best efficiency point. Figure 4.17 shows the diesel engine energy efficiency when the transient consumption is included.

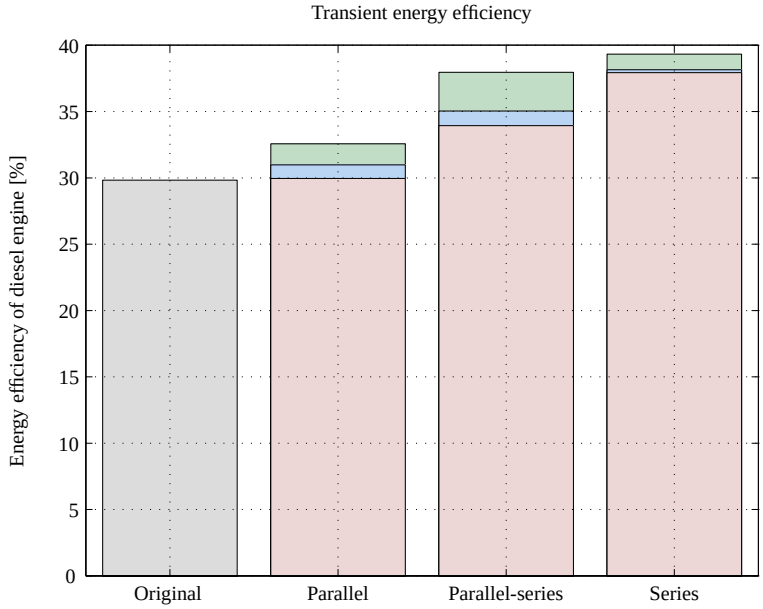

Fig. 4.17: Energy efficiencies of diesel engines in different systems when the extra transient consumption is included. The combinations are the same as above. In the original machine and in the hybrid systems, Tier 4 class engines are used.

Figure 4.17 shows that the higher the diesel engine efficiency is, the smaller is the engine itself and the higher the rated power of the energy storage. In the parallel hybrid system, the energy efficiency of the diesel is 30% in the case of the 200 kW diesel, 31% with the 150 kW diesel and 33% with the 100 kW diesel. In the parallel hybrid system, the diesel efficiency is not significantly dependent upon the energy storage power. This is a result of the fact that the diesel engine is always mechanically connected to the hydraulics and the traction, and therefore, it has to react to their needs. The higher the storage power is, the more slowly the diesel has to react to the load changes and the better will the energy efficiency be.

In the case of the parallel-series hybrid, the diesel engine has to react only to the load changes of the hydraulics. If the energy storage power is small, the difference between the load power and the energy storage power must be taken from the diesel engine, which, therefore, has to run in transient states. The load of the diesel engine also has to react to the SoC of the energy

storage. The extra fuel consumption caused by transients is, however, significantly lower than in the parallel hybrid system.

In the series hybrid machine there is no mechanical connection between the diesel and the mechanical load. Therefore, the diesel engine has to react only by the difference of the load power minus the energy storage power. In addition to this, the diesel engine must keep the SoC of the energy storage suitable. In theory, a series hybrid system can be driven so that the diesel engine is running at a constant power supplying the system with its average power. In practice, however, there is a need to slightly vary the power to keep the SoC within suitable boundaries.

Figure 4.18 shows the energy distributions for the working machine implemented by different hybrid systems. The whole pie represents the energy consumption of the present working machine. In the energy distributions, the energy consumption is divided into amounts of energy consumed in traction, working hydraulics, auxiliary systems and idle running, as well as in traction losses, electric losses and losses in the diesel engine.

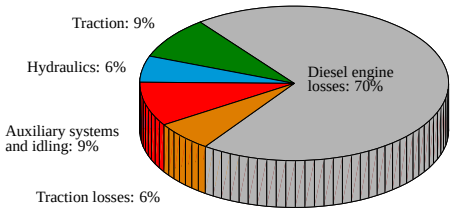

(a) Original system with a 300 kW diesel engine.

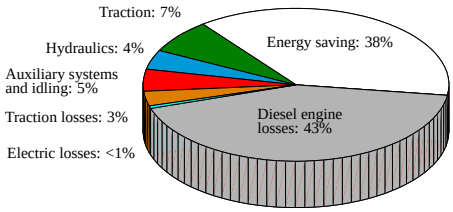

(b) Parallel system with a 150 kW diesel engine.

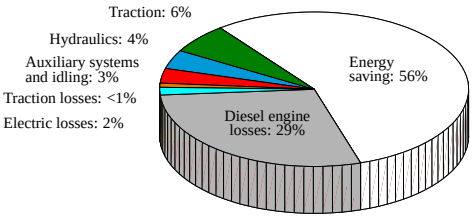

(c) Parallel-series system with a 100 kW diesel engine.

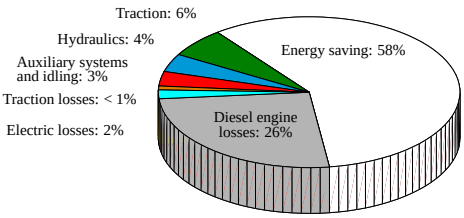

(d) Series system with a 100 kW diesel engine.

Fig. 4.18: Energy distributions for the working machine with different hybrid systems. The whole pie represents the energy consumption of the present machine.

The energy distributions show that in the present working machine, only 15% of the energy taken by the diesel engine is consumed in actual work, while auxiliary systems and idle running use 9% and losses account for 70% of the energy. In the parallel hybrid system, energy savings are brought by the energy recovery and recycling, and less energy intake is

thereby required for the traction and the working hydraulics. The loss energy in the traction is also reduced by the lock-up torque converter used in the system. Further, significant savings in energy are achieved by the smaller diesel engine used in the system, as a result of which less energy is required for auxiliary systems and idle running. In the parallel hybrid system, the actual work accounts for 18% of the energy taken by the diesel engine.

In the parallel-series and series hybrid systems, the energy demand and loss energy in the traction decrease even further as there is no torque converter in the system, and energy can always be recovered in braking. The energy required in auxiliary systems and idle running is reduced into one-third compared with the present system. Moreover, the diesel engine can be made to operate with a far higher efficiency than in the present or parallel hybrid systems. In the parallel-series hybrid system, 23% of the energy taken by the diesel engine is consumed in actual work, while in the series hybrid system, actual work accounts for 24% of the energy consumption. In the series hybrid system, the amount of electric losses is slightly higher than in the parallel-series hybrid system; on the other hand, the diesel engine can be made to operate with a higher efficiency in the series hybrid system, and thus, the system provides the highest energy savings.

Finally, in many cases, the diesel engine of a working machine may run significant periods at no load. Figure 4.19 shows the per unit fuel consumption of parallel, parallel-series and series hybrid machines compared with the consumption of the original machine as a function of no-load time. In all other cases than the series hybrid system, the diesel engine runs at no load. The series hybrid is the more energy efficient, the more there is no-load running in the working machine work cycle. In addition, the more there is no-load operation, the smaller the diesel engine must be if it is not stopped when the working machine runs at no load.

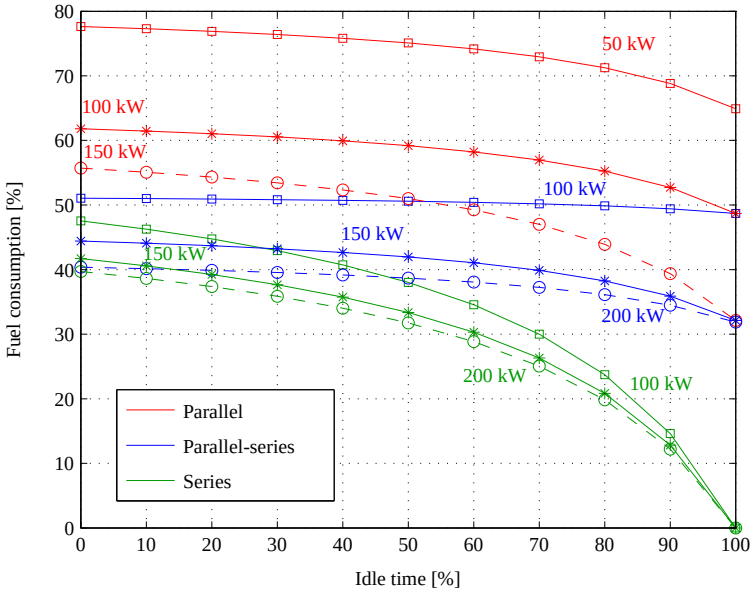

Fig. 4.19: Fuel consumption of the working machine as a function of no-load time varying from 0% to 100%. The consumption of the original machine is 100% in each point. Each system is simulated by using three different diesel engine and energy storage power combinations. The combinations are the same as above. In the figure, the power given next to the curve is the power of the energy storage.

4.4.2 Payback time

A hybrid working machine is more expensive than its traditional diesel-driven counterparts. By simple investment calculations, it is possible to study the economic feasibility of the hybridization process. The economic feasibility can be assessed for instance by the payback time and net present value methods, which are applied to this case also. In the payback time method, the time needed to amortize the hybridization investment is calculated. The payback time in years with a certain interest rate is obtained by [113]

$$PB = \frac{\ln\left(\frac{SA}{SA-Hk}\right)}{\ln\left(1+k\right)} \tag{4.3}$$

where SA represents annual savings, H is the difference between prices and k is the rate of interest. The most favourable investment is the one with the shortest payback time. In the net present value method, the income is discounted to the investment date. The investment is profitable if the net income is higher than the investment.

The net present value (NPV) can be determined by [114]

$$NPV = \sum_{i=1}^{N} \frac{SA}{(1+k)^i}, \tag{4.4}$$

where N is the investment lifetime.

The payback time of a hybrid working machine can be calculated when the annual fuel price savings and the extra costs of different systems compared with the traditional solution are known. The extra costs of a hybrid mobile machine are caused by the new components. The following costs are used in the calculation; Table 4.10.

Table 4.10: Additional cost of components needed for a hybrid working machine.

	Additional cost
Electrical machine [€/kg]	12
Inverter [€/kW]	40

The payback times are determined for parallel, parallel-series and series hybrid systems. The systems apply commercially available energy storages listed in Table 4.6. Table 4.11 gives the sizes of the diesel engine, the electrical machine or machines and the electric energy storage. In the parallel hybrid and parallel-series hybrid system, the energy storage is a commercial 0.96 kWh supercapacitor, and in the series hybrid, a 36.4 kWh LiTi battery. The table also lists the fuel savings in litres and euros when the machine annual operating time is 4000 hours with 40% no-load operation. At no load, the series hybrid genset is stopped if the battery is full. The present working machine consumes 90000 l/a. The extra costs caused by the hybridization have been defined according to the following information: the payback period is based on the component prices, and the diesel fuel price is 1 €/l. The rate of interest is 5%. The NPV of the investment is also calculated when the investment lifetime is 10 years.

Table 4.11: Extra investment cost, fuel consumption, annual savings and NPV for different hybrid systems.

	Parallel	Parallel-series	Series
Diesel engine [kW]	100	100	66
Electric machine [kW]	150	130	66
Energy storage [kWh]	0.96	0.96	36.4
Electric machine additional cost [k€]	6	14	21
Inverter additional cost [k€]	6	15	23
Energy storage additional cost [k€]	40	40	60
Additional cost [k€]	52	69	104
Fuel consumption compared to present machine consumption [%]	56	49	39
Fuel saving $\left[\frac{1000\,\mathrm{l}}{\mathrm{a}}\right]$	39	46	55
Fuel saving [k€]	39	46	55
Payback time [a]	1.4	1.6	2
NPV [k€]	301	355	424

Based on the results obtained by the net present value method, the investment in a hybrid working machine is economically profitable, as the present value of net profits is essentially higher than the extra investment in a hybrid working machine [115]. Furthermore, the payback time is short.

Chapter 5

Conclusion

This doctoral thesis has introduced the subcomponent models required for the modelling of a mobile hybrid working machine, and demonstrated the combination of these components into a complete system model. In the work, efficiencies have been determined for the electrical machines and inverters included in the model by applying an analytical algorithm in the torque–rotational speed plane of the whole electrical machine. Further, by applying the models, the study has focused on the hybridization of a mobile working machine and the effects of the selection and dimensioning of the hybrid system on the fuel consumption of the working machine.

5.1 Hybridization of a mobile working machine

The hybridization of a mobile working machine starts with the determination of the load cycle of the working machine. In many cases, the load cycle of a working machine has to be determined during machine operation in the normal operating environment of the machine. Alternatively, the load cycle can be simulated if there is a virtual simulation model available of the working machine. When the load cycle has been determined, the cycle is analysed and the amounts of energy consumed in different work functions and motions are determined. Finally, the options for energy recovery in different functions are investigated.

When the work cycle has been analysed, the hybrid system is chosen and dimensioned, the fuel consumption of the working machine is determined by simulations, and the payback time is calculated. The process is iterative, and therefore, it may be necessary to repeat the selection and dimensioning process in order to reach the desired results with respect to the payback time and changes required in the system.

5.2 Determining the fuel consumption by simulations

The fuel consumption of a working machine has been simulated by three alternative hybrid solutions and with three different combinations of diesel engine power and electric energy storage power. Based on the simulations, it can be observed that in addition to the hybrid system choice, the component dimensioning and the electric energy storage maximum power in particular affect the fuel consumption. By using a high-power electric energy storage with a sufficient energy capacity, a significantly smaller diesel engine can be selected. Such a diesel engine can then operate in a good efficiency area, and its no-load power is small. A large energy storage also enables slow power transitions for the diesel engine thereby improving its energy efficiency further. The transient fuel consumption of the diesel engine is considerably higher than in the steady state.

The influence of the power and capacity of the energy storage has been studied with a special reference to series hybrids. The energy capacity of the storage seems to be less important than the power capacity. However, the energy capacity of supercapacitors seems not large enough in this case.

Because of the large transient consumption of the diesel engine, the series hybrid system with a sufficient energy storage provides significant fuel consumption savings. The diesel engine not only operates in a high efficiency range but may also operate at a fairly constant power.

It is challenging to determine accurately enough all the parameters of the hybrid system components, that is, the efficiency maps of different machines. One of the reasons for this is that the commercial component manufacturers do not usually provide a designer with the required parameters. In a hybrid working machine, for instance the electrical machines almost never operate in a steady state, but the operating range is considerably larger than in industrial applications. This means that the electrical machine efficiency must be known in all possible operating points, and knowing the efficiency in a few points only is far from enough.

Similarly, the diesel engine efficiency maps have to be known both in the steady-state operation and during transients. Neither the static nor dynamic efficiency maps are easily available from manufacturers, and therefore, these maps should often be measured and generated by the machine builder. The transient fuel consumption is especially important, because ignoring this results in far too positive results, especially in parallel hybrid system simulations.

Regrettably, this study lacks extensive verification results. Verification results have not been provided, because it was by no means possible to build suitable 60-ton machine prototypes for measurements at the university. However, the electrical machine models used in the study were verified by laboratory measurements, and the calculated efficiency map correlated well with the measurement results. The methods used in the modelling, such as in the modelling of the diesel transient consumption, are based on measurements reported for example in [97], and therefore, the results should be considered at least indicative. The fuel consumptions of different systems can also well be compared with each other, even though the absolute levels are not fully correct.

5.3 Suggestions for future work

The accuracy of the modelling can always be improved. For example, the permanent magnet traction motors should be modelled taking cross-saturation into account as these motors are often used at high overloads. The results should be verified by using a prototype machine. The series hybrid traction motor control should minimize the motor current, and it would be advisable to evaluate how well commercial converters are capable of optimal control of motors.

Embedding the simulation models of hybrid working machines in a real-time simulator provides fascinating research opportunities. The real-time combined model could enable virtual testing of the performance of a hybrid working machine for instance in the case of underdimensioned components. In this doctoral thesis, the dimensioning has been carried out so that the system can always react as efficiently as the traditional machine. A real-time simulator should show whether the impact of underdimensioned components is significant or not.

The upper-level control of a hybrid system has a significant impact on the fuel economy. Optimizing the upper-level control is a challenging task and worth further research. Moreover, the diesel engine modelling accuracy should be improved to allow the estimation of the emissions.

References

[1] DieselNet, *Nonroad Diesel Engines Emission Standards*. Accessed 21 May 2012, Online: http://www.dieselnet.com/.

[2] S. Niemi, K. Lundin, J. Perus, M. Laurén, J. Hoikkala, K. Ekman, P. Nousiainen, K. Arve, K. Eränen, and D. Y. Murzin, "HC-SCR catalyst for NOx reduction in an off-road diesel engine," in *Proc. Finnish-Swedish Flame Days*, Naantali, Finland, Jan. 2009.

[3] L. Guzzella and A. Amstutz, "Control of diesel engines," *Control Systems Magazine, IEEE*, vol. 18, no. 5, pp. 53 –71, Oct. 1998.

[4] G. Xinqun, D. Dou, and R. Winsor, "Non-road diesel engine emissions and technology options for meeting them," in *Proc. Agricultural Equipment Technology Conference*, Jan. 2010, Orlando, Florida, USA.

[5] J. Rodríguez-Fernández, A. Tsolakis, R. Cracknell, and R. Clark, "Combining GTL fuel, reformed EGR and HC-SCR aftertreatment system to reduce diesel NOx emissions. A statistical approach," *International Journal of Hydrogen Energy*, vol. 34, no. 6, pp. 2789–2799, Mar. 2009.

[6] D. Hountalas, G. Mavropoulos, and K. Binder, "Effect of exhaust gas recirculation (EGR) temperature for various EGR rates on heavy duty DI diesel engine performance and emissions," *Energy*, vol. 33, no. 2, pp. 272–283, Feb. 2008.

[7] M. Zheng, G. T. Reader, and J. G. Hawley, "Diesel engine exhaust gas recirculation-a review on advanced and novel concepts," *Energy Conversion and Management*, vol. 45, no. 6, pp. 883–900, Apr. 2004.

[8] M. Koebel, M. Elsener, O. Kröcher, C. Schär, R. Röthlisberger, F. Jaussi, and M. Mangold, "NOx reduction in the exhaust of mobile heavy-duty diesel engines by urea-SCR," *Topics in Catalysis*, vol. 30–31, no. 1, pp. 43–48, Jul. 2004.

[9] M. Naseri, S. Chatterjee, M. Castagnola, H. Chen, J. Fedeyko, H. Hess, and J. Li, "Development of SCR on Diesel Particulate Filter System for Heavy Duty Applications," *SAE Int. J. Engines*, vol. 4, no. 1, pp. 1798–1809, Apr. 2011.

[10] M. Okubo, T. Miyashita, T. Kuroki, S. Miwa, and T. Yamamoto, "Regeneration of diesel particulate filter using nonthermal plasma without catalyst," *IEEE Transactions on Industry Applications*, vol. 40, no. 6, pp. 1451–1458, Nov.–Dec. 2004.

[11] M. Bennett, J. Volckens, R. Stanglmaier, A. P. McNichol, W. D. Ellenson, and C. W. Lewis, "Biodiesel effects on particulate radiocarbon (14C) emissions from a diesel engine," *Journal of Aerosol Science*, vol. 39, no. 8, pp. 667–678, Aug. 2008.

[12] M. Glensvig, M. Stolz, B. Willneff, and S. Daum, "Lowering transient emissions and improving transient performance of diesel engines using the venturi booster technology," Aug.–Sep. 2011, Milano, Italy.

[13] J. Eihola, "Kaivoslastaajan hyötysuhteen tarkastelu ja tuottosäätöisen pumppuohjauksen testaus [Analysis of mine loader efficiency and testing of flow rate-adjusted pump control]," Master of Science Thesis, Tampere University of Tehnology, Tampere, Finland, Nov. 2011 (In Finnish), Online: http://dspace.cc.tut.fi/dpub/bitstream/handle/123456789/20735/eihola.pdf?sequence=3.

[14] T. Shang, *Improving Performance of an Energy Efficient Hydraulic Circuit*. Master's Thesis, University of Saskatchewan, Saskatoon, Saskatchewan, 2009.

[15] M. Vael, P. Achten, and P. Jeroen, "Cylinder control with the floating cup hydraulic transformer," in *Proc. The Eighth Scandinacian International Conference on Fluid Power (SICFP)*, May 2003, Tampere, Finland.

[16] K. Heybroek, *Saving Energy in Construction Machinery using Displacement Control Hydraulics: Concept Realization and Validation*. Licentiate thesis, Linköpings universitet, Linköping, Sweden, 2008.

[17] K. Heybroek and J.-O. Palmberg, "Evaluating a pump controlled open circuit solution," in *Proc. The International Exposition for Power Transmission (IFPE)*, Mar. 2008, Nevada, USA.

[18] K. Rydberg, "Hydrostatic drives in heavy mobile machinery-new concepts and development trends," *SAE Technical Paper 981989*, 1998.

[19] T. Kohmäscher, H. Jähne, and H. Deiters, "Moderne voll- und teilhydrostatische. fahrantriebe – untersuchung und weiterentwicklung von antriebsstrangkonzepten mobiler arbeitsmaschinen," *Ölhydraulik und Pneumatik*, no. 5, May 2006.

[20] R. Finzel, H. Jähne, and S. Helduser, "Energieeffiziente antriebssysteme mobiler arbeitsmaschinen," in *Proc. 4th Fachtagung Baumaschinentechnik*, May 2009, Dresden, Germany.

[21] Y. Ancai and J. Jihai, "Research on the regenerative braking control strategy for secondary regulation hydrostatic transmission excavators," in *Proc. International Conference on Mechatronics and Automation (ICMA)*, Aug. 2009,Changchun, China.

[22] P. A. Achten, "A serial hydraulic hybrid drive train for off-road vehicles," in *Proc. The International Exposition for Power Transmission (IFPE)*, Mar. 2008, Nevada, USA.

[23] T. Kautzmann, P. Thiebes, and M. Geimer, "Serieller hydrostatischer hybrid – teil 2: Regelung und potentialabschätzung," *Mobile Maschinen*, vol. 2, no. 4, pp. 38–40, Apr. 2009.

[24] K. Huhtala, P. Nikkilä, P. Vahlsten, and M. Vilenius, "The effect of control to the efficiency of the hydrostatic transmission," in *Proc. 6th Scandinacian International Conference on Fluid Power*, May 1999, Tampere, Finland.

[25] T. Lin, Q. Wang, B. Hu, and W. Gong, "Research on the energy regeneration systems for hybrid hydraulic excavators," *Automation in Construction*, vol. 19, no. 8, pp. 1016–1026, Dec. 2010.

[26] M. Ochiai and S. Ryu, "Hybrid in construction machinery," *Proc. 7th JFPS International Symposium on Fluid Power*, Sep. 2008, Toyama, Japan.

[27] X. Zhang, S. Liu, Z. Huang, and L. Chen, "Research on the system of boom potential recovery in hydraulic excavator," in *Proc. International Conference on Digital Manufacturing and Automation (ICDMA)*, Dec. 2010, ChangSha, China.

[28] T.-S. Kwon, S.-W. Lee, S.-K. Sul, C.-G. Park, N.-I. Kim, B.-I. Kang, and M.-S. Hong, "Power control algorithm for hybrid excavator with supercapacitor," *IEEE Transactions on Industry Applications*, vol. 46, no. 4, pp. 1447–1455, Jul. Aug. 2010.

[29] J. I. Yoon, A. K. Kwan, and D. Q. Truong, "A study on an energy saving electro-hydraulic excavator," in *ICCAS-SICE*, Aug. 2009, Fukuoka, Japan.

[30] M. Ehsani, Y. Gao, S. E. Gay, and A. Emadi, *Modern Electric, Hybrid Electric, and Fuel Cell Vehicles: Fundamentals, Theory, and Design*. CRC Press, 2005.

[31] G. Maggetto and J. Van Mierlo, "Electric and electric hybrid vehicle technology: a survey," in *Proc. IEE Seminar Electric, Hybrid and Fuel Cell Vehicles*, Apr. 2000, Durham, UK.

[32] R. Weinstock, P. Krein, and R. White, "Optimal sizing and selection of hybrid electric vehicle components," in *Proc. Power Electronics Specialists Conference (PESC)*, Jun. 1993, Seattle, WA, USA.

[33] S.-M. Kim and S.-K. Sul, "Control of rubber tyred gantry crane with energy storage based on supercapacitor bank," *IEEE Transactions on Power Electronics*, vol. 21, no. 5, pp. 1420–1427, Sep. 2006.

[34] S. Mulder, *Energy Management Strategy for a Hybrid Container Crane*. Master of Science Thesis, Delft University of Technology, Delft, Netherlands, 2009.

[35] Q. Xiao, Q. Wang, and Y. Zhang, "Control strategies of power system in hybrid hydraulic excevator," *Automation in Construction*, vol. 17, no. 4, pp. 361–367, May. 2008.

[36] X. Lin, S.-X. Pan, and D.-Y. Wang, "Dynamic simulation and optimal control strategy for a parallel hybrid hydraulic excavator," *Journal of Zhejiang University SCIENCE A*, vol. 9, no. 5, pp. 624–632, May 2008.

[37] C.-C. Lin, H. Peng, J. Grizzle, and J.-M. Kang, "Power management strategy for a parallel hybrid electric truck," *IEEE Transactions on Control Systems Technology*, vol. 11, no. 6, pp. 839–849, Nov. 2003.

[38] J. Kessels, F. Willems, W. Schoot, and P. van den Bosch, "Integrated energy & emission management for hybrid electric truck with SCR aftertreatment," in *Proc. IEEE Vehicle Power and Propulsion Conference (VPPC)*, Sep. 2010, Lille, France.

[39] S.-J. Hou, Y. Zou, and R. Chen, "Feed-forward model development of a hybrid electric truck for power management studies," in *Proc. 2nd International Conference on Intelligent Control and Information Processing (ICICIP)*, Jul. 2011, Harbin, China.

[40] J. Tervola, "Hybridiharvesteri lähes puolittaa polttoainekulut," *Tekniikka ja Talous*, Sep. 27/2003.

[41] Elforest, "Elforest web site," Online: www.el-forest.se/sv/fordon, Accessed 21 Dec. 2012.

[42] Komatsu, "Komatsu web site," Online: www.komatsu.eu/displayBrochure.ashx?id=82172, Accessed 21 Dec. 2012.

[43] Cargotec, "Cargotec web site," Online: www.cargotec.com/en-global/PS/Straddle-Carriers/Hybrid-SC/Pages/default.aspx, Accessed 21 Dec. 2012.

[44] M. Beck, C. Ehret, M. Kliffken, and D. van Bracht, "Das hydrostatisch regenerative bremssystem von rexroth: Anwendungen und potentiale für fahrzeuge mit hydrostatischem fahrantrieb," in *Proc. 4th Fachtagung Baumaschinentechnik*, May 2009, Dresden, Germany.

[45] D.-Y. Jo and S. Kwak, "Development of fuel-efficient construction equipment," in *Proc. IEEE 8th International Conference on Power Electronics and ECCE Asia (ICPE ECCE)*, May–Jun. 2011, Jeju, Korea.

[46] A. Froberg, J. Aslund, and L. Nielsen, "Optimal transient control of power generation in hybrid construction equipment," in *Proc. IEEE Vehicle Power and Propulsion Conference (VPPC)*, Sep. 2011, Chicago, IL, USA.

[47] T. Lin, Q. Wang, B. Hu, and W. Gong, "Development of hybrid powered hydraulic construction machinery," *Automation in Construction*, vol. 19, no. 1, pp. 11–19, Jan. 2010.

[48] A. Bouscayrol, R. Schoenfeld, G. Dauphin-Tanguy, G.-H. Geitner, X. Guillaud, A. Pennamen, and J. Hautier, "Different energetic descriptions for electromechanical systems," in *Proc. of the European Conference on Power Electronics and Applications (EPE)*, Sep. 2005, Dresden, Germany.

[49] K. Chen, A. Bouscayrol, and W. Lhomme, "Energetic macroscopic representation and inversion-based control: Application to an electric vehicle with an electrical differential," *Journal of Asian Electric Vehicles*, vol. 6, no. 1, pp. 1097–1102, Jun. 2008.

[50] A. Bouscayrol, X. Guillaud, P. Delarue, and B. Lemaire-Semail, "Energetic macroscopic representation and inversion-based control illustrated on a wind-energy-conversion system using hardware-in-the-loop simulation," *IEEE Transactions on Industrial Electronics*, vol. 56, no. 12, pp. 4826–4835, Dec. 2009.

[51] T. Letrouvé, A. Bouscayrol, W. Lhomme, N. Dollinger, and F. Calvairac, "Different models of a traction drive for an electric vehicle simulation," in *Proc. IEEE Vehicle Power and Propulsion Conference (VPPC)*, Sep. 2010, Lille, France.

[52] F. Millo, L. Rolando, and M. Andreata, "Numerical simulation for vehicle powertrain development, numerical analysis - theory and application," Prof. Jan Awrejcewicz (Ed.), InTech, Sep. 2011, Online: http://www.intechopen.com/books/numerical-analysis-theory-and-application/numerical-simulation-for-vehicle-powertrain-development.

[53] K. Stockman, S. Dereyne, D. Vanhooydonck, W. Symens, J. Lemmens, and W. Deprez, "Iso efficiency contour measurement results for variable speed drives," in *Proc. 19 th International Conference on Electrical Machines (ICEM)*, Sep. 2010, Rome, Italy.

[54] W. Deprez, J. Lemmens, D. Vanhooydonck, W. Symens, K. Stockman, S. Dereyne, and J. Driesen, "Iso efficiency contours as a concept to characterize variable speed drive efficiency," in *Proc. 19 th International Conference on Electrical Machines (ICEM)*, Sep. 2010, Rome, Italy.

[55] V. Ruuskanen, "Design aspects of megawatt-range direct driven permanent magnet wind generators," Doctoral dissertation, Lappeenranta University of Tehnology, Lappeenranta, Finland, Dec. 2011, Online: http://urn.fi/URN:ISBN:978-952-265-184-6.

[56] A. Proca and A. Keyhani, "Identification of variable frequency induction motor models from operating data," *Energy Conversion, IEEE Transactions on*, vol. 17, no. 1, pp. 24–31, Mar. 2002.

[57] S. Zoroofi, "Modeling and simulation of vehicular power systems," Master's, Chalmers University of Tehnology, Göteborg, Sweden, Mar. 2008.

[58] N. Urasaki, T. Senjyu, and K. Uezato, "Relationship of parallel model and series model for permanent magnet synchronous motors taking iron loss into account," *IEEE Transactions on Energy Conversion*, vol. 19, no. 2, pp. 265–270, Jun. 2004.

[59] V. Ruuskanen, P. Immonen, J. Nerg, and J. Pyrhönen, "Determining electrical efficiency of permanent magnet synchronous machines with different control methods," *Electrical Engineering (Archiv fur Elektrotechnik)*, vol. 94, no. 2, pp. 97–106, Jun. 2012.

[60] G. Bertotti, "General properties of power losses in soft ferromagnetic materials," *IEEE Transactions on Magnetics*, vol. 24, no. 1, pp. 621–630, Jan. 1988.

[61] M. Bašić, D. Vukadinović, and D. Lukač, "Novel dynamic model of self-excited induction generator with iron losses," *International Journal of Mathematical Models and Methods in Applied Sciences*, vol. 5, no. 2, pp. 221–229, Sep. 2011.

[62] E. Levi, M. Sokola, A. Boglietti, and M. Pastorelli, "Iron loss in rotor-flux-oriented induction machines: identification, assessment of detuning, and compensation," *IEEE Transactions on Power Electronics*, vol. 11, no. 5, pp. 698–709, Sep. 1996.

[63] A. Dey, A. Tripathi, B. Singh, B. Dwivedi, and D. Chandra, "An improved model of a three phase induction motor incorporating the parameter variations," *Electical Power Quality and Utilisation, Journal*, vol. 14, no. 1, pp. 73–78, Sep. 2008.

[64] S.-D. Wee, M.-H. Shin, and D.-S. Hyun, "Stator-flux-oriented control of induction motor considering iron loss," *IEEE Transactions on Industrial Electronics*, vol. 48, no. 3, pp. 602–608, Jun. 2001.

[65] E. Levi and M. Wang, "Impact of iron loss on speed estimation in sensorless vector controlled induction machines," in *Proc. 23rd International Conference on Industrial Electronics, Control and Instrumentation, IECON 97*, Nov. 1997, New Orleans, Louisiana.

[66] P. Vas, *Vector Control of AC Machine*. New York: Oxford University Press, 1990.

[67] A. Stankovic, E. Benedict, V. John, and T. Lipo, "A novel method for measuring induction machine magnetizing inductance," *IEEE Transactions on Industry Applications*, vol. 39, no. 5, pp. 1257–1263, Sep.–Oct. 2003.

[68] R. Seebacher, G. Dannerer, K. Krischan, and R. Ingruber, "Modeling the induction machine's main inductance as a function of the supply frequency and the magnetizing and the torque building component of the stator current," in *Proc. 13th European Conference on of the Power Electronics and Applications (EPE)*, Sep. 2009, Barcelona, Spain.

[69] J. Nerg, J. Pyrhönen, J. Partanen, and E. Ritchie, "Induction motor magnetizing inductance modelling as a function of torque," in *Proc. of the 16 th International Conference on Electrical Machines (ICEM)*, Sep. 2004, Cracow, Poland.

[70] D. Chatterjee, "A simple leakage inductance identification technique for three phase induction machines under variable flux condition," *IEEE Transactions on Industrial Electronics*, to be published, 2011.

[71] L. Aarniovuori, "Induction motor drive energy efficiency-simulation and analysis," Doctoral dissertation, Lappeenranta University of Tehnology, Lappeenranta, Finland, Aug. 2010, Online: http://urn.fi/URN:ISBN:978-952-214-963-3.

[72] D. Seyoum, C. Grantham, and M. Rahman, "The dynamic characteristics of an isolated self-excited induction generator driven by a wind turbine," *IEEE Transactions on Industry Applications*, vol. 39, no. 4, pp. 936–944, Jul–Aug. 2003.

[73] L. Kalamen, P. Rafajdus, P. Sekerak, and V. Hrabovcova, "A novel method of magnetizing inductance investigation of self-excited induction generators," *IEEE Transactions on Magnetics*, vol. 48, no. 4, pp. 1657–1660, Apr. 2012.

[74] J. Pyrhönen, T. Jokinen, and V. Hrabovcová, *Design of Rotational Electrical Machines*. Chichester, England: John Wiley & Sons, Ltd., 2008.

[75] J. Kolar, H. Ertl, and F. C. Zach, "Influence of the modulation method on the conduction and switching losses of a pwm converter system," *IEEE Transactions on Industry Applications*, vol. 27, no. 6, pp. 1063–1075, 1991.

[76] A. Wintrich, U. Nicolai, W. Tursky, and T. Reimann, *Application Manual Power Semiconductors*. Semikron, Online: http://www.semikron.com/skcompub/en/Application_Manual_en_2011.pdf, Accessed 21 Apr. 2013.

[77] Semikron, "Semikron SKM600GA12E4 datasheet," Online: http://pdf1.alldatasheet.com/datasheet-pdf/view/323813/SEMIKRON/SKM600GA12E4.html, Accessed 21 Apr. 2013.

[78] M. Stoller, "Graphene based ultracapacitors for electrical energy storage," Doctoral dissertation, The University of Texas at Austin, Texas, USA, Dec. 2011, Online: http://hdl.handle.net/2152/ETD-UT-2011-12-4516.

[79] A. Burke, "Batteries and ultracapacitors for electric, hybrid, and fuel cell vehicles," *Proc. IEEE*, vol. 95, no. 4, pp. 806–820, Apr. 2007.

[80] A. Burke and M. Miller, "The power capability of ultracapacitors and lithium batteries for electric and hybrid vehicle applications," *Journal of Power Sources*, vol. 196, no. 1, pp. 514–522, Jan. 2011.

[81] A. Burke, "Performance, charging, and second-use considerations for lithium batteries for plug-in electric vehicles," *Institute of Transportation Studies, University of California, Davis, Research Report*, 2009.

[82] G. Nielson and A. Emadi, "Hybrid energy storage systems for high-performance hybrid electric vehicles," in *Proc. IEEE Vehicle Power and Propulsion Conference (VPPC)*, Sep. 2011, Chicago, Il. USA, pp. 1–6.

[83] A. Väyrynen and J. Salminen, "Lithium ion battery production," *The Journal of Chemical Thermodynamics*, vol. 46, pp. 80–85, Sep. 2012.

[84] P. Denholm, A. Dillon, E. Drury, G. Glatzmaier, J. Logan, M. Melaina, J. Neubauer, D. Reindl, S. Santhanagopalan, K. Smith, D. Steward, and S. Succar, "Energy storage for power grids and electric transportation: A technology assessmen," *Research Report*, 2012, Online: http://www.fas.org/sgp/crs/misc/R42455.pdf.

[85] W.-C. Lih, J.-H. Yen, F.-H. Shieh, and Y.-M. Liao, "Second use of retired lithium-ion battery packs from electric vehicles: Technological challenges, cost analysis and optimal business model," in *Proc. International Symposium on Computer, Consumer and Control (IS3C)*, Jun. 2012, pp. 381–384.

[86] P. Nelson and K. Amine, "Advanced lithium-ion batteries for plug-in hybrid-electric vehicles," in *Proc. 23th World Battery, Hybrid and Fuel Cell Electric Vehicle Symposium*, Dec. 2007, Anaheim, CA, USA.

[87] N. Omar, M. Daowd, P. Bossche, O. Hegazy, J. Smekens, T. Coosemans, and J. Mierlo, "Rechargeable energy storage systems for plug-in hybrid electric vehicles-assessment of electrical characteristics," *Energies*, vol. 5, no. 8, pp. 2952–2988, Aug. 2012.

[88] R. Misback, "Applications for advanced energy storage- new technology," in *Proc. Advanced Energy 2010*, Nov. 2010,New York, USA.

[89] P. Bauer, N. Stembridge, J. Doppler, and P. Kumar, "Battery modeling and fast charging of ev," in *Proc. 14th International Power Electronics and Motion Control Conference (EPE/PEMC)*, Sep. 2010, Metropol Lake Resort Ohrid, Macedonia.

[90] L. Gao, S. Liu, and R. Dougal, "Dynamic lithium-ion battery model for system simulation," *IEEE Transactions on Components and Packaging Technologies*, vol. 25, no. 3, pp. 495–505, Sep. 2002.

[91] Youngho, "Ultracapacitor technology powers electronic circuits," in *Power Electronic Technology*, Oct. 2003.

[92] L. Zubieta and R. Bonert, "Characterization of double-layer capacitors (dlcs) for power electronics applications," in *Proc. IEEE Industry Applications Conference*, Oct. 1998.

[93] F. Rafik, H. Gualous, R. Gallay, A. Crausaz, and A. Berthon, "Frequency, thermal and voltage supercapacitor characterization and modeling," *Journal of Power Sources*, vol. 165, no. 2, pp. 928–934, Mar. 2007.

[94] H. Douglas and P. Pillay, "Sizing ultracapacitors for hybrid electric vehicles," in *Proc. IEEE Industrial Electronics Society (IECON)*, Nov. 2005.

[95] P. A. Hansson, M. Lindgren, M. Nordin, and O. Pettersson, "A methodology for measuring the effects of transient loads on the fuel efficiency of agricultural tractors," *Applied Engineering in Agriculture*, vol. 19, no. 3, pp. 251–257, May 2003.

[96] M. Lindgren, "Engine exhaust gas emissions from non-road mobile machinery," Doctoral dissertation, Swedish University of Agricultural Sciences, Uppsala, Sweden, Sep. 2004, Online: http://pub.epsilon.slu.se/644/.

[97] M. Lindgren and P.-A. Hansson, "Effects of transient conditions on exhaust emission from two non-road diesel engines," *Biosystems Engineering*, vol. 87, no. 1, pp. 57–66, Jan. 2004.

[98] M. Tinker, "Wheel loader powertrain modeling for real-time vehicle dynamic simulation," Master of Science Thesis, University of Iowa, Iowa City, Iowa Jul. 2006, Online: http://ir.uiowa.edu/etd/75/.

[99] J. Shue, "Hydrokinetic torque converter stator blade construction," Patent US 7 083 381, August 1, 2006.

[100] H. Murrenhoff, "Trends and some recent developments in mobile hydraulics," in *Proc. 12th International conference and exhibition on pneumatics and hydraulics*, Sep. 2007, Miskolc/Eger, Hungary.

[101] H. Beck, "Emissionsreduzierung durch antriebsstrangoptimierung," in *Proc. 4th Fachtagung Baumaschinentechnik*, May 2009, Dresden, Germany.

[102] R. Rajamani, "Longitudinal vehicle dynamics," in *Vehicle Dynamics and Control*, ser. Mechanical Engineering Series, F. F. Ling, Ed. Springer US, 2006, pp. 95–122, 10.1007/0-387-28823-64. [Online]. Available: http://dx.doi.org/10.1007/0-387-28823-64

[103] L. Guzzella and A. Sciarretta, *Vehicle Propulsion Systems: Introduction to Modeling and Optimization*. Berlin Heidelberg, New York: Springer, 2005.

[104] S. Hausberger, M. Rexeos, M. Zallinger, and R. Luz, "Emission factors from the model phem for the hbefa version 3," 2009, Report, Graz University of Technology, Graz, Austria.

[105] H. A. Rakha, K. Ahn, K. Moran, B. Saerens, and E. Van den Bulck, "Virginia tech comprehensive power-based fuel consumption model: Model development and testing," *Transportation Research Part D: Transport and Environment*, vol. 16, no. 7, pp. 492–503, Oct. 2011.

[106] S. Martini and S. Campo, "A control strategy for ACC in heavy truck application," in *Proc. 7th word congress on intelligent system*, Nov. 2000, Turin, Italy.

[107] A. G. Simpson, "Full-cycle assessment of alternative fuels for light-duty road vehicles in australia," in *Proc. 7th Annual Environmental Research Conference*, Dec. 2003, Marysville, Australia.

[108] C. Chan, "The state of the art of electric, hybrid, and fuel cell vehicles," *Proc. IEEE*, vol. 95, no. 4, pp. 704–718, Apr. 2007.

[109] J. Ottosson, "Energy management and control of electrical drives in hybrid electrical vehicles," Licentiate Thesis, Lund University, Lund, Sweden, Jun. 2007.

[110] Altairnano, "Altairnano 24 V 60 Ah Battery Module datasheet," Online: www.altairnano.com/wp-content/uploads/2011/10/60Ah-DataSheet.pdf, Accessed 1 Dec. 2012.

[111] Maxwell, "Maxwell BMOD0063 125 V Heavy Transportation Module datasheet," Online: www.maxwell.com/products/ultracapacitors/docs/datasheet_bmod0063_1014696.pdf, Accessed 1 Dec. 2012.

[112] S. You and C. N. Rasmussen, "Generic modelling framework for economic analysis of battery systems," in *Prof. IET Renewable Power Generation Conference*, Sep. 2011, Edinburgh, United Kingdom, pp. 1–6.

[113] P. Barnwal and G. Tiwari, "Life cycle cost analysis of a hybrid photovoltaic/thermal greenhouse dryer," *The Open Environmental Journal*, vol. 2, no. 1, pp. 39–46, 2008.

[114] M. Illés, "Transforming the net present value for a comparable one," *Theory, Methodology, Practice*, vol. 8, no. 1, pp. 24–27, 2012.

[115] A. Avadikyan and P. Llerena, "A real options reasoning approach to hybrid vehicle investments," *Technological Forecasting and Social Change*, vol. 77, no. 4, pp. 649–661, May 2010.

ACTA UNIVERSITATIS LAPPEENRANTAENSIS

476. LAAKSONEN, JONNA. Tactile-proprioceptive robotic grasping. 2012. Diss.

477. KALLIO, ANNE. Enhancing absorptive capacity in a non-research and development context An action research approach to converting individual observations into organizational awareness. 2012. Diss.

478. LÄTTILÄ, LAURI. Improving transportation and warehousing efficiency with simulation based decision support systems. 2012. Diss.

479. OYOMNO, WERE. Usable privacy preservation in mobile electronic personality. 2012. Diss.

480. LINNALA, MIKKO. Simulation and optimization tools in paper machine concept design. 2012. Diss.

481. KORPIJÄRVI, JUHA. Aging based maintenance and reinvestment scheduling of electric distribution network. 2012. Diss.

482. KORHONEN, JUHAMATTI. Active inverter output filtering methods. 2012. Diss.

483. KLODOWSKI, ADAM. Flexible multibody approach in bone strain estimation during physical activity: quantifying osteogenic potential. 2012. Diss.

484. VUORENMAA, MARKKU. Osaamisen johtaminen pk-yrityksen kansainvälisen kasvun elinkaarella. 2012. Diss.

485. RAUTIAINEN, MARITA. Dynamic ownership in family business systems – a portfolio business approach. 2012. Diss.

486. LILIUS, REIJO. THE FINNISH IT INDUSTRIES IN TRANSITION Defining and measuring the Finnish software product and IT services industries by applying theoretical frameworks . 2012. Diss.

487. TUOMINEN, PASI. The purpose of consumer co-operation: implications for the management and governance of co-operatives. 2012. Diss.

488. SAARI, ESA. Suurnopeus-turbokoneroottoreiden termodynaaminen ja mekaaninen mallinnus sekä rakenneanalyysi. 2012. Diss.

489. PAANANEN, MIKKO. On innovative search: the use of internal and external sources of innovation among Finnish innovators. 2012. Diss.

490. BELOVA, POLINA. Quasiclassical approach to the vortex state in iron-based superconductors. 2012. Diss.

491. HIETANEN, IIRO. Design and characterization of large area position sensitive radiation detectors. 2012. Diss.

492. PÄSSILÄ, ANNE. A reflexive model of research-based theatre Processing innovation of the cross-road of theatre, reflection and practice-based innovation activities. 2012. Diss.

493. RIIPINEN, TOMI. Modeling and control of the power conversion unit in a solid oxide fuel cell environment. 2012. Diss.

494. RANTALAINEN, TUOMAS. Simulation of structural stress history based on dynamic analysis. 2012. Diss.

495. SALMIMIES, RIINA. Acidic dissolution of iron oxides and regeneration of a ceramic filter medium. 2012. Diss.

496. VAUTERIN, JOHANNA JULIA. The demand for global student talent: Capitalizing on the value of university-industry collaboration. 2012. Diss.

497. RILLA, MARKO. Design of salient pole PM synchronous machines for a vehicle traction application. 2012. Diss.

498. FEDOROVA, ELENA. Interdependence of emerging Eastern European stock markets. 2012. Diss.

499. SHAH, SRUJAL. Analysis and validation of space averaged drag model for numerical simulations of gas-solid flows in fluidized beds. 2012. Diss.

500. WANG, YONGBO. Novel methods for error modeling and parameter identification of redundant hybrid serial-parallel robot. 2012. Diss.

501. MAXIMOV, ALEXANDER. Theoretical analysis and numerical simulation of spectral radiative properties of combustion gases in oxy/air-fired combustion systems. 2012. Diss.

502. KUTVONEN, ANTERO. Strategic external deployment of intellectual assets. 2012. Diss.

503. VÄISÄNEN, VESA. Performance and scalability of isolated DC-DC converter topologies in low voltage, high current applications. 2012. Diss.

504. IKONEN, MIKA. Power cycling lifetime estimation of IGBT power modules based on chip temperature modeling. 2012. Diss.

505. LEIVO, TIMO. Pricing anomalies in the Finnish stock market. 2012. Diss.

506. NISKANEN, ANTTI. Landfill gas management as engineered landfills – Estimation and mitigation of environmental aspects. 2012. Diss.

507. QIU, FENG. Surface transformation hardening of carbon steel with high power fiber laser. 2012. Diss.

508. SMIRNOV, ALEXANDER. AMB system for high-speed motors using automatic commissioning. 2012. Diss.

509. ESKELINEN, HARRI, ed. Advanced approaches to analytical and systematic DFMA analysis. 2013.

510. RYYNÄNEN, HARRI. From network pictures to network insight in solution business – the role of internal communication. 2013. Diss.

511. JÄRVI, KATI. Ecosystem architecture design: endogenous and exogenous structural properties. 2013. Diss.

512. PIILI, HEIDI. Characterisation of laser beam and paper material interaction. 2013. Diss.

513. MONTO, SARI. Towards inter-organizational working capital management. 2013. Diss.

514. PIRINEN, MARKKU. The effects of welding heat input usability of high strength steels in welded structures. 2013. Diss.

515. SARKKINEN, MINNA. Strategic innovation management based on three dimensions diagnosing innovation development needs in a peripheral region. 2013. Diss.

516. MAGLYAS, ANDREY. Overcoming the complexity of software product management. 2013. Diss.

517. MOISIO, SAMI. A soft contact collision method for real-time simulation of triangularized geometries in multibody dynamics. 2013. Diss.